A Cluster Multi-Spacecraft Study of Earth's Bow Shock

by

Thamer Yousef Saeed Alrefay

Previous Degrees (Master of Science, Florida Institute of Technology , 2003)
Bachelor of Science,King Abdulaziz University, 1996

A DISSERTATION SUBMITTED IN PARTIAL FULFILLMENT OF THE REQUIREMENTS FOR THE DEGREE OF

Doctor of Philosophy

In the Graduate Academic Unit of Physics

Supervisor(s):	Abdelhaq M. Hamza, PhD, Physics
	Karim Meziane, PhD, Physics
Examining Board:	P. T. Jayachandran, PhD, Physics, Chair
	William Ward, PhD, Physics
	Karl Butler, PhD, Earth Sciences
External Examiner:	Christian. Mazelle, PhD, Physics, CESR

This dissertation is accepted by the

Dean of Graduate Studies

THE UNIVERSITY OF NEW BRUNSWICK

July, 2014

©Thamer Yousef Saeed Alrefay, 2014

Abstract

The location, shape and motion of Earth's bow shock are investigated using observations based on measurements made by the Cluster spacecraft quartet. Several bow shock crossings have been identified and carefully characterized according to relevant plasma parameters; a collection of 133 shocks has been selected and analysed using a timing method. The shock crossings cover orbits in which the spacecraft separation is of the order of $\sim$ 600 km or less. When present, the magnetic field fluctuations are suppressed using the conventional low-pass filtering technique prior to implementing timing method. The results of this investigation are compared with both Gas Dynamics and Magnetohydrodynamics (MHD) bow shock models.We have found, on a statistical basis, that the shock standoff position derived from the timing method agrees well with the Gas Dynamics predictions for high Mach-number cases only. We have also found that for half the crossings, the timing and the conic-based shock normals agree within an 11 degree-angle. Our results strongly indicate that the motion of the shock is predominantly along the Sun-Earth direction; a departure from this direction is not related to the

shock-crossing location. Shock velocities below ~ 80 km/s satisfactorily follow a nearly Gaussian distribution with zero mean and a standard deviation of ~ 42 km/s. We show that high speed motions are correlated with sharp increases in the solar wind upstream ram pressure, and are consistent with gas dynamics model predictions.

Dedication

To my Family.

They sacrificed much and often to allow me to complete this work.

Acknowledgements

I Should First Thank Dr. Karim Meziane , for his guidance and support over the past five years, without which I wouldn't have got very far at all. I would like to express my sincere gratitude to my supervisor Prof . Abdelhaq Hamza, for his help and support. I would like to thank my family for encouraging me down to pursue the PhD. I would like to acknowledge the King Abdulaziz City for Science and Technology (KACST) for financial support over the course of my PhD studies. Finally I would like to thank the The Cluster Active Archive (CAA) for providing the data.

Table of Contents

Abstract **ii**

Dedication **iv**

Acknowledgments **v**

Table of Contents **ix**

List of Tables **x**

List of Figures **xvi**

Abbreviations **xvii**

1 Introduction **1**

1.1 Shocks in Space 1

1.2 The Earth's Bow Shock 3

1.3 Physics of the Earth's Bow Shock 4

1.4 Statistical Models 11

1.5 Earth's Bow Shock Dynamics 21

1.6 Shock Nonstationarity 25

2 Data Selection and analysis **27**

2.1 Cluster Multi-Spacecraft Measurements 27

2.1.1 Cluster Orbit and Separation Strategy 27

2.1.2 Timing Analysis Method for Multi-Spacecraft Data . . 30

2.2 Plasma and Interplanetary Magnetic Field Measurements . . 32

2.2.1 FGM (Fluxgate Magnetometer) 33

2.2.2 CIS (Cluster Ion Spectroscopy) 34

2.2.3 ACE/SWEPAM 36

2.2.4 ACE/MAG 37

2.3 ACE - Cluster Time Delay 38

2.4 Events Selection 43

2.4.1 Selected Events 44

2.4.2 Event Selection Criteria 54

2.4.3 Observation Positions and Database 55

3 Standoff Distance and Shape of the Earth's Bow Shock **61**

3.1 Standoff Position 61

3.2 Shape 69

3.2.1 Comparison of Coplanarity and Timing Based Normal 70

3.2.2 Comparison of Conics Models and Timing Normals . . 75

4 Earth's Bow Shock Dynamics **80**

4.1 Statistical Results 81
4.2 A Simple Model for the Shock Velocity Distribution Function 85
4.2.1 The Probability Distribution Function of $P_z(z)$, $z = xy$ 85
4.2.2 Probability Density for the Velocity of the Bow Shock Near the Nose Region 89
4.3 The Case of High Speed Shocks 98

5 Conclusion and Discussion **104**

Bibliography **109**

A General Solution to the Rankine-Hugoniot Conservation Equations **123**
A.0.1 The $\vec{E} \times \vec{B}$ drift velocity 124
A.0.2 The Hoffman-Teller Velocity 125
A.1 The shock Frame 126
A.1.1 Case $V_s = 0$, $\eta = 0$ and $\alpha = 1$ 137
A.1.2 Solving for the downstream plasma variables 140
A.1.3 The Normal Component of the Electric Field $\vec{E}$ and the Pressure Term 143

B The Earth's Magnetopause Size **145**

C Error Analysis **148**
C.1 Shock Speed 148

C.2 Shock Normal 151
C.3 Standoff Distance 151

D Forcing the Conics Models **153**

D.1 Forcing Ellipsoid Model 154
D.2 Forcing the Hyperboloid Model 154
D.3 Forcing Merka's Model 155

Vita

List of Tables

2.1 FGM Operating Ranges (numbered 2 to 5 were used) [12]. . . 34
2.2 CIS Instrument Status [13]. 35
2.3 Shock parameters 46
2.4 Shock parameters 49
2.5 Shock parameters 49

List of Figures

1.1 Model of bow wave determined for various Mach Numbers in the case of a steady aligned flow (from [24]). 9
1.2 The left panel shows nearly 2500 crossing events undertaken by by HEOS-1, HEOS-2 & five IMP spacecrafts [37]. The right panel illustrates the GSE coordinate system. 14

2.1 Cluster orbits during polar cusp crossings [6]. 28

2.2 The Cluster inter-spacecraft separation strategy allows the plasma structure in the magnetosphere to be investigated on different spatial scales during the mission [6]. 29

2.3 An example showing the time delay difference between ACE and Cluster SC. Panel *a* shows the magnetic field data time series from Cluster-3. Panel *b* shows the magnetic field data time series from ACE. Panel *c* the data is shifted by 0.587 hours obtained from flat estimation. Panel *d* same as panel *c* but the data is now shifted by 0.620 hours obtained after visual inspection of the magnetic field structures. 39

2.4 An example showing how the time delay between ACE and Cluster is obtained. The top two panels show the magnetic field magnitude data time series from ACE and Cluster-3, respectively. The third panel shows both profiles with the Cluster-C3 data shifted by 0.850 hours from its original base, while the bottom panel is the same as the panel above with magnetosheath data removed. 41

2.5 Second example showing how the time delay between ACE and Cluster is obtained. Same as Figure 2.4 with the Cluster-C3 data shifted by 0.631 hours from its original base. 42

2.6 An Example of a clean bow shock crossing; the time series correspond to the magnetic field from Cluster/IMF. On March 31, 2001 at 1714:39 UT.Successive crossings along the spacecraft trajectories are indicated in color on the top panel. The middle panel shows the same profile shifted in time according to lags Δt obtained from cross-correlation analysis. The bottom panel provides those cross correlation values as function of lag. 46

2.7 A Second Example of a clean bow shock crossing same as Figure 2.6. Event of March 28, 2001 at 1312:22 UT. 47

2.8 Third Example of a clean bow shock crossing on March 19, 2001 at 1948:30 UT. 48

2.9 An Example of a bow shock crossing where low band-pass filtering is applied on the time series of IMF measurements. Panel (a) shows the IMF measurements while panel (b) shows the same time series where the high frequency fluctuations are suppressed. Panel (c) shows the same time series as in panel (b) but shifted in time according to lags Δt, obtained from cross correlation between each spacecraft time series and that of the reference spacecraft S/C3. The bottom panel provides those cross correlation values as function of lag. 50

2.10 A Second example of using low band-pass filtering on April 20, 2002. 52

2.11 An Example of bow shock crossing in which the moving average technique is applied on the time series of IMF measurements. Panel (a) shows the IMF measurements and panel (b) shows the same time series where the hight frequency fluctuations are suppressed. Panel (c) shows the same time series of IMF as in panel (b) but shifted in time according to lags Δt resulting from cross correlations between each spacecraft time series and that of S/C3. The bottom panel provides those cross correlation values as function of lag. 53
2.12 A second example of using moving averages on April 20, 2002. 54
2.13 An Example of a non selected event on January 21 2002. In panel (a), the IMF shows fluctuations in the shock structure. In panel (b), the IMF fluctuations have been suppressed using moving averages. Panel (c) shows the same time series of IMF as in panel (b) shifted in time according to lags Δt obtained from the cross correlation analysis between each spacecraft time series using S/C3 as a reference. 56
2.14 Second example of eliminated event on May 16, 2001. Bow shock crossing at 18:02:35 UT. 57
2.15 Satellite Crossing Positions in The GSE frame of reference. The red curve represents a nominal bow shock 58
2.16 Histogram for θ_{Bn}. 59
2.17 Histogram for Mach number. 59

2.18 Histogram for Ram pressure. 60

3.1 Timing standoff distance a_{st} versus standoff distance a_s obtained from a gas dynamics model (top panel) and a MHD model (bottom panel); errors are added to the plots. Each point corresponds to a bow shock crossing, and the slope of the dashed line is one. 67

3.2 $\Delta = a_{st} - a_s$ histogram 68

3.3 Absolute value of $\Delta = a_{st} - a_s$ versus M_A 69

3.4 Histogram of angles between shock normal estimated by timing method and those calculated by coplanarity. 71

3.5 Comparison of θ_{Bn} obtained from coplanarity and those obtained from timing analysis. 72

3.6 Angle θ_{ct} between the coplanarity and timing normals as a function of timing θ_{Bn}. 73

3.7 Deviation of coplanarity normal from timing normal as a function of the angle between the upstream and downstream magnetic fields directions. 74

3.8 Histogram of the angle between the timing normal $\hat{\mathbf{n}}_\mathbf{t}$ and the paraboloid shock normal $\hat{\mathbf{n}}_\mathbf{m}$. 77

3.9 Histogram of the angle between the timing normal $\hat{\mathbf{n}}_\mathbf{t}$ and the ellipsoid shock normal $\hat{\mathbf{n}}_\mathbf{m}$. 78

3.10 Histogram of the angle between the timing normal $\hat{\mathbf{n}}_\mathbf{t}$ and the hyperboloid shock normal $\hat{\mathbf{n}}_\mathbf{m}$. 78
3.11 Histogram of the angle between the timing normal $\hat{\mathbf{n}}_\mathbf{t}$ and Merka's shock normal $\hat{\mathbf{n}}_\mathbf{m}$. 79

4.1 Successive shock crossings. 81
4.2 Histogram for the direction of shock motion along the 3 cartesian coordinates. 82
4.3 Shock velocity distribution. 83
4.4 Solar plasma data time series measured by WIND-3DP experiment on 1996, January 01-02. The two top panels show the ion density and flow velocity, respectively. The third panel shows the solar wind ram pressure in nPa unit, while the bottom panel displays the time variation of the ram pressure (in nPa/s) at WIND location. The time resolution for the measurements is 12 sec. 93
4.5 Solar wind ram pressure distribution. 94
4.6 Solar wind dp/dt distribution. 95
4.7 Results of the numerical integration of expression (4.19) for two values of p_0. 96
4.8 Velocity PDF calculated from expression (4.19); the free parameters are obtained from the average of the plasma data measurements by WIND on 1996 January 01-02. 97

4.9 Bottom panel shows magnetic field magnitude from Cluster-3 and ACE spacecraft on April 20, 2002. Data from ACE are shifted by 42.4 minutes. The middle and top panels show measurements from ACE of ram pressure ρ and Alfvèn and Mach number M_A as derived from the solar wind and magnetic field data, respectively. The two dashed vertical lines in both panels indicate a 12 minute window centred on the shock crossing we have analyzed. 98

4.10 Observed shock velocity versus the variation of the ram pressure at ACE location. The convective time delay between ACE and Cluster is taken into account. 102

4.11 Observed shock velocity versus the model shock velocity predicted with Equation 4.27. The dashed line represents the best linear fit. 103

List of Symbols and Abbreviation

MHD	Magnetohydrodynamics.
RH	Rankine - Hugoniot Relation/ Condtion.
IMP & IMP-8	Interplanetary Monitoring Platform (Spacecraft).
HEOS-1 & HEOS-2	Highly Eccentric Orbit Satellite.
WIND	Mission for long term Solar wind measurements (Spacecraft).
GEOTAIL	Mission for observing the Earth's magnetosphere (Spacecraft).
ACE	Advanced Composition Explorer (Spacecraft).
IMF	Interplanetary Magnetic Field.
ISEE 1 & 2	International Sun-Earth Explorer (Spacecraft).
AMPTE/IRM	Active Magnetospheric Particle Tracer Explorers.
GSE	Geocentric Ecliptic coordinate system.
TD	Tangential Discontinuities.
Ogo-5	Orbiting Geophysics observatories (Spacecraft).
MAGTO-4/INTERBALL	Satellite - subsatellite (Spacecraft).
Cluster/FGM	Cluster Fluxgate- Magnetometer.
Cluster/CIS	Cluster Ion Spectrometer.
ACE/MAG	ACE - Magnetometer instrument.
ACE/SWEPAM	ACE - Solar Wind Electron, Proton and alpha Monitor.

Cluster/CIS-HIA	High Ion Analyzer.
CODIF	Composition and Distribution Function (Data).
MCP	Microchannel plate.
FFT	Fast Furrier Transform.
GPE	Geocentric Plasma Ecliptic system.
PDFs	Probability distribution Functions.
PIC	Particle-in-cell.
ρ	Density.
$\vec{U}$	Bulk Velocity.
$\vec{J}$	Current Density.
$\vec{B}$	Magnetic Field.
$\vec{B}_u$	Magnetic Field (Upstream).
$\vec{B}_d$	Magnetic Field (Downstream).
$\vec{E}$	Electric Field.
μ_0	Permeability of free space.
P	Pressure.
γ	ratio of heat capacities.
V_A	Alfven speed.
M	Mach number.
M_A	Alfven Mach number.
M_S	Acoustic Mach number.
M_{MS}	Magnetosonic Mach number.
R_E	Earth's Radius.
$\vec{S}$	Poynting vector.
D_0	Obstacle position.
Δ	Distance between obstacle and shock.
V_{SW}	Solar Wind velocity.
p	Solar wind ram pressure.
R_{BS}	The bow shock standoff distance.
V_S	Shock speed.
θ_{Bn}	Angle between the shock normal and the magnetic field.
θct	The angle between shock normal (by timing) and normal (by Coplanarity).

a_s	The Shock nose distance.
a_{st}	The Shock nose distance (By timing analysis).
$a_s(GD)$	The Shock nose distance (By Gasdynamics model).
$a_s(MHD)$	The Shock nose distance (By MHD model).
b_s	Distance to the flaring.
(n_x, n_y, n_z)	The Shock normal components.
$\hat{\mathbf{n}}_t$	The Shock normal (By timing analysis).
$\hat{\mathbf{n}}_m$	The Shock normal (By Conics model).
N_{SW}	Solar wind density.
V_{SW}	Solar wind velocity.
T_{SW}	Solar wind temperature.

Chapter 1

Introduction

1.1 Shocks in Space

The solar wind plasma emanating from the lower region of the solar corona constantly propagates at supersonic and superalfvenic speed through the interplanetary medium. When this flow encounters an obstacle that opposes its propagation, a shock wave forms upstream (of the obstacle). While crossing the surface of the shock wave, of limited spatial-thickness, the solar wind is slowed down and becomes subsonic. Since the mean free path of a solar wind particle is very large compared to the shock thickness, the shock is qualified as collisionless. The processes involved in shocks are very complex in nature. Their main role is to convert the excess in kinetic energy of the incident flux to thermal and magnetic energy, which in turn are redistributed and transmitted to the downstream plasma. The mechanisms of energy dissipa-

tion determine the character of the shock, and depend on several parameters such as the Mach number of the solar wind, the ratio of the thermal to the magnetic pressure and the inclination of the interplanetary magnetic field relative to the shock surface. Part of the energy is dissipated through physical processes that lead to particle acceleration. Therefore, shocks constitute a very important source of energetic particles in interplanetary space, and understanding the production mechanisms of the latter is essential given their implications in cosmic electrodynamics. Collisionless acceleration of particles up to several hundred keV is often invoked as a potential explanation for phenomena such as radio bursts of type II or type III in the solar system or cosmic radiation.

The Earth's bow shock is the closest shock accessible to scientists through various satellite missions. These missions have in turn made it possible to investigate different physical phenomena pertinent to the solar-terrestrial interaction. Access to the interplanetary medium through satellites has enabled the harvest of valuable spatial and temporal data on the Earth bow shock, and has allowed us to understand some aspects of shock physics that were inaccessible to us until now.

Fast-mode shocks such as the Earth's bow shock and interplanetary traveling shocks, because they have been observed frequently, have been studied extensively. Slow shocks occurring in the magnetosphere have also been studied but not to the same extent. The availability of large observational databases has stimulated a tremendous theoretical effort, including an increasing num-

ber of sophisticated numerical experiments, in an attempt to understand their relevance.

The main objective of the thesis is to characterize the shape and quantify the dynamics of Earth's bow shock. This objective is consistent with various Earth bow shock investigations, and a systematic study using data from the European Cluster mission is conducted to achieve the goal set. The interpretation of the observations is examined in the light of various conventional theories. In the first chapter, we summarize the characteristics of the terrestrial bow shock and describe briefly the traditional theoretical shock models used to explain and interpret the satellite observations. In the second chapter, we describe the data selected and the analysis techniques adopted. The results of our investigation are presented in chapters three and four, and we finally conclude with chapter five.

1.2 The Earth's Bow Shock

The Earth's bow shock continues to attract intense and extensive theoretical and experimental investigations. It is believed that the study of the shape as well as the dynamics of the Earth's bow shock will lead to a better understanding of collisionless shocks in both laboratory and space plasmas. Moreover, the Earth's bow shock constitutes a rare natural archetype of an irreversible transition boundary between plasmas, which in turn suggests and

justifies the relevance of bow shock studies. With an ever increasing data collection rate by space-borne missions, numerous studies have been carried out; this has led to the availability of quality data with higher time resolution, including magnetic field, plasma and spacecraft potential measurements, making it possible to perform and conduct extensive and sophisticated analyses on the shape and position of the bow shock. Bow shock studies have led to a better understanding of the solar wind-magnetosphere interaction; they have unveiled some of the physical mechanisms taking place in the foreshock, and have allowed for a better description of the thermodynamic state of the plasma through the determination of the specific heat ratio γ [58]. It has been established that the bow shock shape and position are determined by the size and location of the magnetopause as well as the interplanetary conditions characterized by ram pressure, Mach number and Interplanetary Magnetic Field (IMF) orientation [83]. This last aspect is directly related to our present work and will be examined thoroughly in the remainder of this thesis.

1.3 Physics of the Earth's Bow Shock

The theoretical investigations of planetary bow shocks provide predictions for the bow wave location as well as the properties of the downstream plasma as functions of the interplanetary conditions. The most simple model is based on the Magnetohydrodynamics (MHD) approximation, which treats

the multi-species plasma as a single compressible, perfectly conducting fluid described by ideal fluid dynamics equations coupled with Maxwell's equations for the electromagnetic fields. The MHD approximation is usually adopted in its ideal form, which neglects the plasma resistive effects. When viscosity along with the thermal and electrical conductivities are included, the non-ideal MHD approximation has to be used, and the resulting model equations are sophisticated enough not to allow for any analytical solution when dealing with three-dimensional boundary problems such as the bow shock. It is equally difficult to construct numerical solutions, because of the multi-scale nature of the bow shock; one has to be able to resolve kinetic scales that are completely averaged out in the MHD approximation, in order to take into account physical phenomena occurring within the thickness of the shock boundary. Over the past two decades, we have witnessed a burst of numerical activity that attempts to address some of the bow shock observations, but these remain attempts at best. There is a need to overcome the numerical constraints and some of the analytical ones to a certain extent because most of the theoretical models available to us in the literature are ideal MHD models that have become obsolete given the precision of the state-of-art observational diagnostics available to us through various satellite missions which have flown, are flying or to be flown. Current observations have revealed that the dissipative effects within the shock boundary and in the adjacent regions can no longer be ignored, which in turn requires models that transcend the limitations of the ideal MHD approximation.

The ideal MHD equations are given by:

Continuity equation,

$$\frac{\partial \rho}{\partial t} + \nabla \cdot \left(\rho \vec{U} \right) = 0$$

Momentum equation

$$\rho \frac{\partial \vec{U}}{\partial t} + \rho \vec{U} \cdot \nabla \vec{U} = -\nabla P + \vec{J} \times \vec{B}$$

Energy conservation equation

$$\frac{\partial}{\partial t} \left(\frac{\rho U^2}{2} + \frac{P}{\gamma - 1} + \frac{B^2}{2\mu_0} \right) + \nabla \cdot \left(\frac{\rho U^2}{2} \vec{U} + \frac{\gamma}{\gamma - 1} P \vec{U} + \frac{\vec{E} \times \vec{B}}{\mu_0} \right) = 0$$

with the ideal Ohms's law,

$$\vec{E} + \vec{U} \times \vec{B} = 0$$

Faraday's law for a perfectly conducting fluid,

$$\frac{\partial \vec{B}}{\partial t} = \nabla \times \left(\vec{U} \times \vec{B} \right)$$

Ampere's law in which the displacement current is omitted:

$$\mu_0 \vec{J} = \nabla \times \vec{B}$$

and finally, the divergence free magnetic field condition,

$$\nabla \cdot \vec{B} = 0$$

Notice that Faraday's law ensures that $\nabla \cdot \vec{B}$ will be zero for all time.
In the ideal MHD equations above, $\vec{B}$ is the magnetic field, $\vec{E}$ is the electric field, $\vec{U}$ is the plasma bulk flow, $\vec{J}$ the current density, ρ is the mass density and P the plasma pressure. The $\vec{J} \times \vec{B}$ force can be expressed in the following form:

$$\vec{J} \times \vec{B} = \frac{1}{\mu_0} \left(\vec{B} \cdot \nabla \right) \vec{B} - \nabla \left(\frac{B^2}{2\mu_0} \right)$$

Note that the gradient of $\vec{B}$ along the field line is just the curvature $\vec{\kappa}$ of the field line:

$$\vec{\kappa} \equiv \hat{\mathbf{b}} \cdot \nabla \hat{\mathbf{b}}$$

whose magnitude is equal to the reciprocal of the radius of curvature, and where $\hat{\mathbf{b}} = \vec{B}/|\vec{B}|$.
If one introduces the perpendicular gradient:

$$\nabla_\perp \equiv \nabla - \hat{\mathbf{b}}\hat{\mathbf{b}} \cdot \nabla$$

one can then express the $\vec{J} \times \vec{B}$ force in the following form:

$$\vec{J} \times \vec{B} = \frac{B^2}{\mu_0} \vec{\kappa} - \nabla_\perp \left(\frac{B^2}{2\mu_0} \right)$$

which suggest a "tension" of magnetic field lines producing a force $\frac{B^2}{\mu_0}\vec{\kappa}$ directed toward the center of curvature - in much the same way as tension acts on a string. Then the "pressure" of the magnetic field produces a force $\nabla_\perp \left(\frac{B^2}{2\mu_0}\right)$ directed away from the region of high field strength. Bending the field produces tension and compressing it produces a restoring pressure.

Although simplified, the ideal MHD equations are none the less difficult to solve in the case of an arbitrary three-dimensional boundary subject to initial conditions. However, for simple boundaries, exact solutions exist particularly in the case of steady flows. A satisfactory model based on the ideal MHD approximation that accounts for the global bow wave morphology was reported by Spreiter and Rizzi [24] for the special case of an axisymmetric obstacle in a flow aligned with the interplanetary magnetic field; the ideal MHD equations, through a change of variables, can be reduced to those of neutral fluid dynamics (gas dynamics) without a state equation. The resulting 'pseudo-gasdynamics' equations are then solved and the solutions are shown on Figure 1.1 for various numerical values of the Alfven Mach number $M_A = U/V_A$, where $V_A = B/\sqrt{4\pi\rho}$. An important result of the model is that the bow waves tend toward an asymptotic spatial boundary for $M_A \geq 10$, i.e the shock boundary location becomes independent of M_A when the Alfven Mach number is larger than $\sim$ 10. In addition, a counter intuitive result suggests that the shock boundary tends to approach the obstacle near the nose when the Mach number M_A decreases. The ad-hoc replacement of M_A

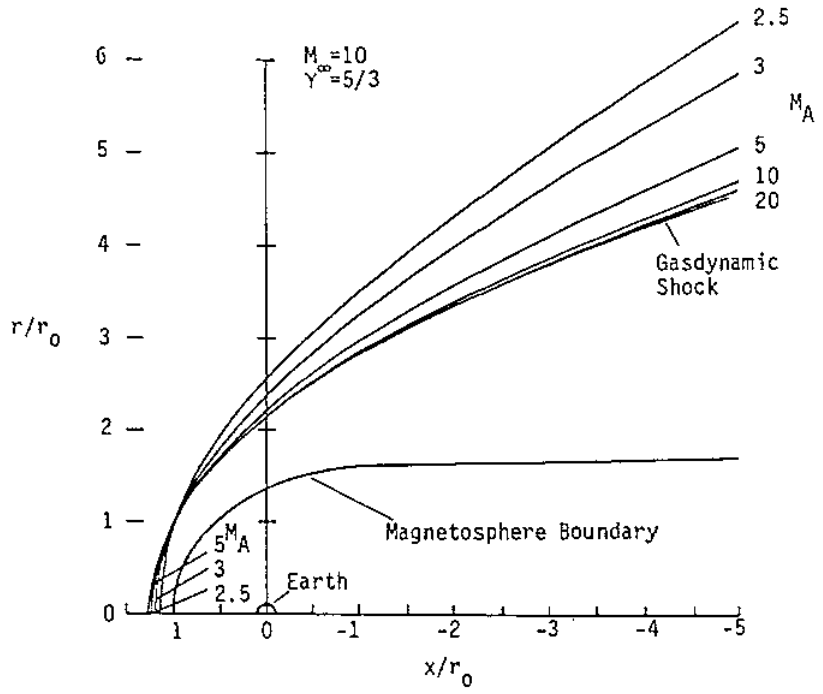

Figure 1.1: Model of bow wave determined for various Mach Numbers in the case of a steady aligned flow (from [24]).

by the acoustic Mach number M_S or the magnetosonic Mach number M_{MS} or a combination of both does not resolve the problem. An acceptable model would predict an outward motion of the shock flanks and simultaneous receding of the nose away from the obstacle.

Solutions for non aligned fields ($\vec{U}$,$\vec{B}$) exist in some special cases. It is worth citing the results published by Wu et al. [79] and Zhuang and Russell [78]. In the work reported by Wu et al. [79], the Interplanetary Magnetic Field (IMF) is omitted, and the model put forth simulates the flow passing a dipolar mag-

netic field; a bow wave develops through which the Rankine-Hugoniot jump conditions are approximatively satisfied. However, the simulations by Wu et al. [79] give rise to a shock boundary with a thickness of ($\sim 5\ R_E$ where R_E is the Earth radius) suggesting serious limitations in the simulation model or undetected numerical instabilities. In the study reported by Zhuang and Russell [78], an examination of the jump conditions at the shock boundary is explored in order to obtain a semi-analytic representation of the plasma and magnetic field patterns behind the shock. Mapping the contours of constant density (isopycnal) and pressure (isobar) behind the shock, the authors were able to estimate the distance of the shock boundary to the obstacle for various solar wind and magnetic field conditions.

At this point, we should emphasize the fact that the excitation of MHD wave modes from infinitesimal disturbances is a necessary but not sufficient step to account for the development of a highly nonlinear shock solution. A nonlinear buildup mechanism has to take place in order for these MHD fluctuations to evolve into a shock front upstream of the obstacle. Conservation laws dictate the plasma and magnetic field conditions upstream and downstream of the shock boundary. The continuity conditions across the boundary are usually written in a coordinate system defined by ($\hat{\mathbf{n}}$,$\hat{\mathbf{t}}$), where $\hat{\mathbf{n}}$ and $\hat{\mathbf{t}}$ are unit vectors normal and tangential to the shock surface, respectively. If we denote by $[Q]$ the difference between the upstream and downstream values of a quantity Q, the jump conditions (also known as the Rankine-Hugoniot

(RH) Relations/Conditions) are given by the following relations:

$$[B_n] = 0 \quad (1.1)$$

$$[E_t] = 0 \quad (1.2)$$

$$[\rho(U_n - V_s)] = 0 \quad (1.3)$$

$$\left[\rho(U_n - V_s)(\vec{U} - \vec{V}_s) + P\hat{n} - \frac{B_n}{\mu_0}\vec{B} + \frac{B^2}{2\mu_0}\hat{n}\right] = 0 \quad (1.4)$$

$$\left[\frac{1}{2}\rho(U_n - V_s)(\vec{U} - \vec{V}_s)^2 + \frac{\gamma}{\gamma - 1}P(U_n - V_s) + S_n\right] = 0 \quad (1.5)$$

where, $\vec{S}$ is the Poynting vector

$$\vec{S} = \frac{1}{\mu_0}\vec{E} \times \vec{B} = \frac{1}{\mu_0}\left[B^2(\vec{U} - \vec{V}_s) - (\vec{U} - \vec{V}_s) \cdot \vec{B}\vec{B}\right] \quad (1.6)$$

The RH relations are written in an inertial frame, which explains the inclusion of the shock speed V_s. The general three-dimensional solutions, for initial upstream conditions, are provided in detail in Appendix A.

1.4 Statistical Models

The Earth's magnetosphere is an obstacle to the superalfvenic and supersonic solar wind emanating from the solar corona. The fast magnetosonic waves, generated in the solar wind, pile up in front the magnetosphere and travel back upstream creating a bow shock wave with a shape and location that

have been the subject of extensive scientific investigations for more than four decades. Diagnostics onboard of various spacecrafts have allowed for studies to be conducted and for results on bow shock physics to be communicated on a continuous basis. Modelling the Earth's bow shock, including size, location and dynamics has been a daunting challenge to the space physics community for more than half a century. All bow shock models, which we briefly review in this section, are geometrical and statistical in nature. More precisely, these models use a 2D-surface described by equation (1.7) with ten coefficients a_i $(i = 1, ...10)$ determined by an optimization procedure which subjects the equation to the empirical observational data. The conventional approach uses either the gas dynamics approximation [50, 47, 68] or the MHD approximation[30, 41, 31].

Usually, these parameters are strongly dependent upon the solar wind plasma and magnetic field conditions. Therefore, the average shape of the bow shock is given by the following general form of a 2D-surface:

$$a_1x^2+a_2y^2+a_2z^2+2a_4xy+2a_5xz+2a_6yz+2a_7x+2a_8y+2a_9z+a_{10}=0 \quad (1.7)$$

The first model was derived from Interplanetary Monitoring Platform (IMP) spacecraft observations, and is therefore restricted to topologies near the Ecliptic plane [36]. In this two-dimensional model, although a correction to aberration due to Earth's orbital motion was taken into account, the effect

of the the solar wind ram pressure variations was ignored. The first three-dimensional bow shock model was reported by Formisano [37] in a study based on nearly 2500 crossing events undertaken by by HEOS-1, HEOS-2 & five IMP spacecrafts, which revealed that the solar wind ram pressure is a controlling parameter as far as bow shock location is concerned. However, the resulting model was bias towards out of Ecliptic plane geometries because of numerous high-latitude crossings by HEOS-2 (Figure 1.2). Using a much larger database, Slavin and Holzer [50] and Slavin et al. [49] explored for the first time the effects of Mach number on the shock topology and compared their results with a Geodynamics theoretical model predictions. They were able to quantify the impact of the Mach number on the shock boundary.
Another three-dimensional model, less cited in the literature, was reported by Verigin et al. [66] in which a study based on 450 distinct WIND bow shock crossings is described. With a semi-empirical planetary bow shock reported in an earlier work [67], the authors introduced a novel element in the normalization of the shock curvature. In particular, the asymmetry of the terrestrial bow shock in the Ecliptic plane is studied as a function of Friedrichs diagram anisotropy. It is worth mentioning that the model's predictions of the shock stand-off distances dependence on Mach number is not quantitatively intuitive.

The first exhaustive three-dimensional study that accounts for the impacts of ram pressure variations, sonic (M_S), magnetosonic (M_{MS}) and Alfenvic

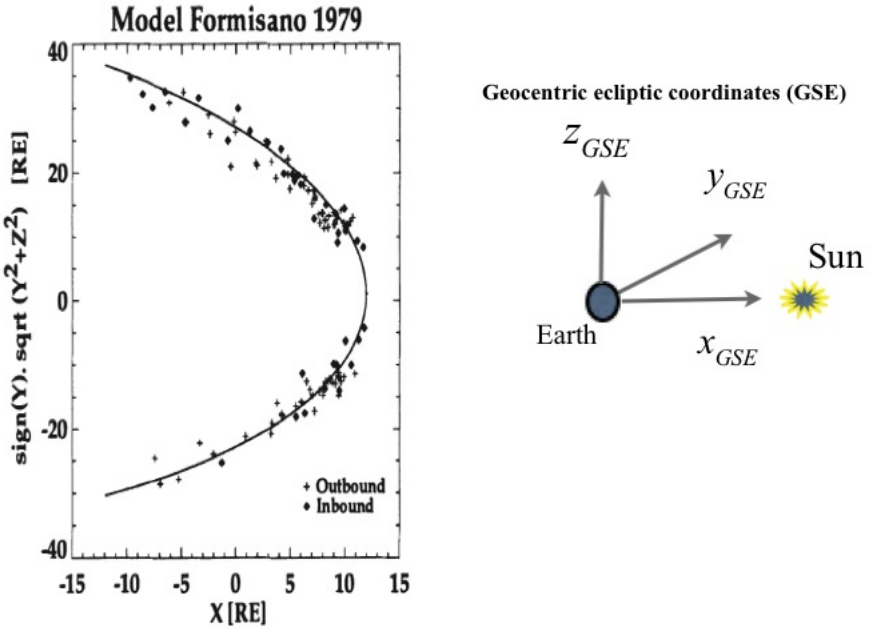

Figure 1.2: The left panel shows nearly 2500 crossing events undertaken by by HEOS-1, HEOS-2 & five IMP spacecrafts [37]. The right panel illustrates the GSE coordinate system.

(M_A) Mach numbers as well as the direction of the interplanetary magnetic field on shock topology was reported by Peredo et al. [41]. The study is based on a collection of 1392 crossing events from 17 satellites. Although widely used, Safránková et al. [57] and Merka et al [31] have shown that Perodo et al. [41] model overestimates the bow shock standoff distance by at least 20%. It turns out that Peredo et al. [41] used a significant number of incorrect satellite positions at the bow shock crossings. Merka et al. [33] used the same, but corrected, data set and an approach similar to that of Peredo et

al. [41] to derive a new bow shock model. In the latter, the coefficients of the second-order ideal bow shock surface are M_A dependent. Finally, similar bow shock models, not described in this thesis, and apparently less cited in the literature, have been developed, and we only mention those reported by Russell and Petrinec [44], Verigin et al. [66] and Chao et al. [69].

With a multitude of bow shock models available in the literature, a systemic comparison was attempted by some authors. Any comparative study should not only include the various models available, but should also compare their predictions to satellite observations. In one such study, Dmitriev et al. [70] analyzed a collection of 755 events from the WIND and GEOTAIL spacecrafts while relying on the ACE satellite to monitor the upstream conditions. Only four models were considered in the Dmitriev et al. [70] comparative study, and those include the Peredo et al. [41], Petrinec and Russel [44] and Verigin et al. [66] gas dynamics models, and the Chao et al. [69] model. The authors found that the latter model provides the best capability to predict bow shock crossing. In addition, the ram pressure and the magnetosonic Mach number are reported to be the most important parameters controlling the bow shock size and shape.

A more exhaustive comparative study was reported by Merka et al. [31], which included the majority of models available in the literature. The study used 2293 bow shock crossings by IMP 8 satellites (collected over 12 years) to scrutinize, under various interplanetary conditions, the deficiencies of each

of the shock models. The statistical study lead Merka et al. [31] to conclude that the model most coherent with the observations was the one reported by Formisano [37]. It was also found that for large IMF magnitudes, all the models studied, with the exception of the model reported by Němeček and Šafránková [61], underestimate the bow shock standing off distance. Furthermore, the same underestimation of the bow distance was found when the upstream Mach numbers were $M \leq 5$, which in turn confirms the shortcomings of the shock models for low Mach numbers. The models also do not properly reflect changes in the relative orientation of the IMF and solar wind velocity. Moreover, by taking the upstream parameters from a distant solar wind monitor (the WIND spacecraft in this case), the models were found to predict greater stand off distances from Earth: a result very likely due to the spacecraft's separation perpendicular to the solar wind flow or to calibration-differences of the plasma density measurements by the spacecraft. Merka's [31] comparative study clearly illustrates the ongoing challenges to understanding the bow shock dynamics.

As an extension to various studies, the shock nose region continues to be an intensive subject to study because it is the location where the Mach number is maximum and where the shock expansion is at its minimum. This in turn has triggered the investigation of the shock standoff distance (or subsolar point position) by various scientists whose common goal has been to test various shock models including the MHD and Gas Dynamics models.

However, the observations can only provide, in most cases, a lower limit for the standoff distance. On the other hand, all the models used are either based on Gas Dynamics or on a phenomenological extension. Němeček and Šafránková [61], in one of their early studies of the shock standoff distance, analyzed several sets of bow shock crossings, and reported that for large magnitudes of the interplanetary magnetic field the bow shock nose was found to be standing off at a distance greater than that predicted by Formisano [37]. The first empirical formula that allows the calculation of the standoff distance Δ between the obstacle and the shock was first reported by Seiff [22] and later by Spreiter et al. [23], and is primarily based on the Gas Dynamics approximation. This empirical formula is given by:

$$\Delta = 1.1 D_0 \rho \tag{1.8}$$

where D_0 is the distance from Earth to the Magnetopause (obstacle), and ρ the upstream to downstream particle density ratio (notice that for convenience and coherence with the notation used in the literature, ρ no longer represents the mass density but instead it represents the ratio of particle densities). This formula constitutes the fundamental basis of all studies of the shock standoff distance, and ought to be scrutinized for as far as its limitations and validity are concerned when dealing magnetized plasmas in particular; its use in the context of solar wind-magnetosphere interaction is not understood. Moreover, the upstream to downstream plasma density ratio is

given in terms of the acoustic M_S Mach number [62], and it appears that the shock can form at a finite distance for $M_S = 1$. One ought to seek a physical explanation for this empirical description of the standoff distance; indeed, it provides a good approximation for Δ for large Mach numbers $M_S \geq 5$. In the case of shocks which form and evolve in plasmas, Spreiter et al. [23] suggested interchanging M_S by M_A for aligned flows (IMF parallel to V_{SW}) while Russell [45] opted for M_{MS}, the magnetosonic Mach number, arguing that the shocks are magnetosonic in nature. It turned out that replacing M_S by M_A or M_{MS} underestimates the observed standoff distance for M_A and $M_{MS} \sim 1 - 3$ [46, 30]. In an attempt to resolve these issues, Farris and Russell [48] explored the plasma and the magnetic field conditions in order to determine the most controlling parameters of the standoff distance. As a result, the authors modified the Spreiter et al. [23] formula in an attempt to try and resolve the Mach number =1 anomaly while at the same time drafting a solution for low Mach number shocks in which the Gas Dynamics approximation ceases to be valid. Farris and Russell's new formula is widely used and is given by:

$$\Delta = 1.1 D_0 \frac{(\gamma - 1)M_A^2 + 2}{(\gamma + 1)(M_A^2 - 1)} \tag{1.9}$$

Using numerical simulations, Cairns and Grabble [64] extended Spreiter et al. [23] empirical formula (1.8) to explore the MHD effects. More precisely, the authors replaced the coefficient 1.1 by a factor k which is determined

by the results of numerical simulations while the shock compression ratio ρ is obtained from the solution of Rankine-Hugoniot at the nose. As a consequence, the authors found that the Mach number M_{MS} is irrelevant and that larger numerical values for the standoff distance were found for low Mach number values M_A. Cairns and Grabbe's [64] work predicts that a change of IMF direction causes a factor 4-change in the shock size; a problematic result indeed. Finally, this last model introduces a singularity (non physical solution) when the plasma flow is parallel to the IMF direction. It turned out the solution provided by Cairns and Grabbe [64] for the aligned flow case was incomplete, and that for low Mach numbers the resolution of the Rankine-Hugoniot conditions provides three shock solutions ($\rho < 1$). In another study based on simultaneous measurements from Prognoz 10 and IMP 8, Němeček and Šafránková [61] provided a new determination of the factor k when using a tilted magnetic field dipole. Němeček and Šafránková [61] found that k is linearly dependent upon the magnitude of the IMF.

As mentioned above, the results of the model proposed by Verigin et al. [66] on the standoff distance contrast with the results reported by Cairns and Grabbe [64]. In the former model, in the case of aligned flows (IMF parallel to V_{SW}), the shock nose region recedes towards Earth with decreasing Alfven Mach number M_A, while for non field-aligned flow, the bow shock expands. Finally in a recent study using a simple but novel approach, Jelinek et al. [71] developed simple models for the magnetopause and the bow shock boundaries. The models use continuous measurements of the magnetic field

and plasma density by sounding spacecrafts to determine the most probable locations of the shock boundary. In practice both ACE and THEMIS observations were used. The models developed are in good agreement with the results obtained from crossing identifications. At the nose region, the shock model predicts that the bow shock standoff distance $R_{BS} = 15.02p^{-\frac{1}{6.35}}$, where p is the solar wind ram pressure.

In addition, and as seen above, the shock standoff distance is linearly related to the size of the magnetopause. At the sub-solar point, this latter is directly obtained from the solar wind and the magnetosphere pressure balance (see Appendix B). In the widely used standard formulation, $D_0 = \eta p^{-1/6}$, where p is the solar wind ram pressure and η a constant that reflects the effective downstream pressure, which is very sensitive to the electric currents flowing along the magnetopause. Several studies followed, which made significant corrections to the standard formulation. As an example, we cite the work of Shue et al. [28] based on a large number of ISEE 1 & 2, AMPTE/IRM and IMP 8 satellites magnetopause crossings. Using a fitting procedure with a modified conic section, the authors provided a new expression for η that is linearly dependent upon the IMF-B_Z. Another study from Jelinek et al. [71] found that D_0 is exclusively dependent upon the ram pressure p with an exponent of $-\frac{1}{5.26}$.

1.5 Earth's Bow Shock Dynamics

The motion of the Earth's bow shock has received less attention, and this is certainly due to the lack and availability of suitable measurements. Any unambiguous study of shock dynamics requires specific multi-point observations, without which any determination of the shock velocity is entailed with significant errors. The first investigations of the shock motion date back to the 1960's [74, 72]. Single satellite observations, including Explorer 33 & 35, Ogo-5 and Heos-1, have estimated shock speeds of $\sim$ 10 km/s on the average. Other studies from Greesntadt [73] reported the observation of a laminar shock exhibiting speeds of the order of $\sim$ 100 km/s. Formisano and Mastrantonio [40] reported, with measurements from the same previous satellites, some observational evidence that solar wind tangential discontinuities (TD) provoke relatively high speed shock motion, usually greater than 50 km/s. The first dual shock observation reports appeared after the launch of ISEE 1 & 2 satellites. The short separation distance between the two satellites (less than 200-300 km) provided an opportunity to increase the precision of the shock dynamics measurements although only one component of the velocity is available. Using magnetic field data, Russell et al. [43] determined the speed of 13 laminar quasi-perpendicular shocks, and found a speed range lying between few km/s to over 100 km/s for the events studied. With similar data, Newbury et al. [55] determined the shock speed of twenty quasi-perpendicular supercritical shocks. The velocities were calculated by

determining the time separation between shock crossings at ISEE1 and ISEE2 and the spatial separation of the spacecraft in the direction along the shock normal. The latter vector was obtained from the magnetic coplanarity assumption. The results provided small to moderate shock speed magnitudes in agreement with previous determinations. Another two-point study of the bow shock motion was later reported by Zastenker et al. [59] using Prognoz 10 and IMP 8 plasma measurements. These authors suggested that, at a given location, the shock triggers a surface wave propagating along the shock front. In this case, however, the separation between the two spacecraft was quiet large ($\sim$ 20 R_E). Šafránková et al. [56] analyzed 130 bow shock crossings by the closely separated spacecraft MAGIO-4/INTERBALL-1 and suggested that 80% of the estimated velocities are consistent with a radial expansion/-compression of the shock surface. Interestingly, this last study indicated that slow shock speeds ($\leq$ 5 km/s) are observed during quiet upstream conditions while the probability of observing high speed shocks increases with disturbed IMF conditions suggesting that the Mach number is a dominant factor in the shock dynamics rather than the variations in ram pressure. Moreover, the investigation of the shock deep-tail flank, although seldom, can provide new elements in understanding shock dynamics. Analyzing 68 far shock flank events ($\sim$ $60R_E$ behind Earth) observed by the Geotail spacecraft, Tsubouchi et al. [75] reported that the bow shock is always in a state dominated by high fluctuations. The authors show that the motion of the shock is directly associated with its shape modification from its nominal form. Faster

bow shock motion (up to $\sim$ 300 km/s) corresponds to significant deviations from the average shape. They suggest that the Alfvenic fluctuations in the solar wind are responsible for such motions.

Paradoxically, theoretical investigations of the Earth's bow shock motion are noticeably few. An initial model was proposed by Smit [76] in which the magnetosphere behaves as a resonant oscillator. To date, and according to our knowledge, Völk and Auer's [58] work forms the sole exhaustive study, although restricted to the nose region, of the impact of the solar wind variations on the shock motion. Based on an empirical Gas Dynamics model, Völk and Auer [58] investigated the dynamics of the shock under various interplanetary conditions including Alfven waves and tangential discontinuities. The theoretical investigation predicts some important results, which potentially could be contrasted with the observations. Thus, under Alfven wave turbulence, the shock would move fast for low Mach number and ram pressure; when these parameters are low, the shock expands beyond its nominal size therefore becoming more sensitive to any perturbation. For typical Mach numbers and solar wind ram pressure, Alfven wave perturbation causes oscillatory shock motion with a speed in the order of $\sim$ 10 km/s, consistent with satellite observations. Another important result is related to the effect of propagating tangential discontinuities. These discontinuities are accompanied by changes in the plasma density in the order of 50% or plasma speed in the order of 10%. The interaction between such impulsive events would

induce shock speeds greater than $\sim$ 85 km/s. We believe that Völk and Auer's [58] seminal work needs to be compared with the increasingly accurate 'recent' measurements such as those performed by the Cluster spacecraft. A comparison of the model with the observations is now plausible given the availability of multi-point measurements.

Prior to the Cluster mission, all shock motion measurements were performed using data collected by single or dual spacecrafts some taking into account the Rankine-Hugoniot constraints and some not taking the RH into consideration. Single spacecraft based determinations used the conservation Rankine-Hugoniot relations [77] throughout the shock boundary. The method consists of an optimization technique, and requires a judicious choice of the upstream and downstream equilibrium plasma states. This technique is subject to significant errors. Dual measurements often require the shock normal to be known precisely since the shock boundary is supposed to move along the normal direction, and the observations provide the velocity along the separation vector between the two satellites. It is now established that coplanarity is a poor estimator of the shock normal. With the launch of the Cluster quartet, full three-dimensional shock velocities as well as shock normal could be determined for the first time. This has become possible because of the tetrahedron configuration of the quartet. Horbury et al. [7] were the first ones to use high time resolution magnetic field measurements by Cluster to study the shape and motion of the shock. From a selected sample of 48

quasi-perpendicular bow shock crossings, Horbury et al. [7] determined the shock normal using a timing method [19]. The method allows for a satisfactory determination of the local shock normal when the spacecraft separation is less than the shock curvature and when the shock acceleration is negligible. With the timing technique, a reliable determination of the local shock normal requires the distance between the quartet elements to be relatively small, given that ripples and surface waves may cause significant deformation. Other studies based on Cluster data using the timing techniques were reported in the literature [34, 54].

1.6 Shock Nonstationarity

With the significant progress in computing hardware and software, numerical simulations of collisionless shocks have replaced in some particular cases laboratory experiments and provided insight, which has led to significant progress in understanding the shock transition layer. Particle-in-cell (PIC) and/or hybrid simulations of two- and three-dimensional shocks have been performed by several authors [81, 80, 82]. The results of these numerical experiments all indicate that low-β supercritical high Mach number shocks are constantly, if subjected to similar conditions, self-reforming. The shock non-stationarity results from various plasma instabilities due to changes in particle distributions occurring at the shock front. Although striking observational evidence of shock self reformation is still lacking, some reports

strongly support their occurrence [34] when plasma and magnetic field conditions are satisfied.

If the shock nonstationarity has little impact on the reliability of the bow shock models described above, it nonetheless renders the experimental determination as well of the theoretical predictions of the shock motion difficult. The shock reformation processes induce motions with various magnitude that could be in the order of the bulk motion of the shock. This is an acute problem particularly for low shock speeds, which are typical. Discriminating the small scale shock motion from the bulk is a real challenge from all points of views, and up to date there has been no report on the subject. Moreover, as explained above an unambiguous determination of the shock speed requires multi-point measurements with some implicit assumptions. Because the technique of measurement consists in the determination of time delays, as explained in the next Chapter, a fundamental assumption stipulates that the shock front is quasi-stable during the successive measurements. Depending upon the time scales involved, the validity of this assumption may be violated given the shock reformation process. Quasi-perpendicular supercritical shocks appear usually as a sharp transition. However, high-precision time magnetic field measurements indicate that the shock transition layer presents short time variations of the different structures making up the shock. This raises serious difficulties in the analysis of the shock motion as derived from successive shock crossings.

Chapter 2

Data Selection and analysis

2.1 Cluster Multi-Spacecraft Measurements

2.1.1 Cluster Orbit and Separation Strategy

The Cluster Spacecraft consists of four identical satellites. Each satellite payload carries the same set of eleven instruments. The Cluster mission is designed to investigate the solar wind-magnetosphere interaction in general, and the development of plasma structures of various scales as well as their spacial and temporal evolution in key regions of the Earth's magnetic environment in particular. These key regions of the near–Earth environment are: the solar wind ,the bow shock, the magnetopause, the polar cusp and the magnetotail as illustrated in Figure 2.1.

In order to achieve the scientific objectives of the mission, a polar orbit was adapted such that the perigee is at $4R_E$ while the apogee is at $19.6R_E$, with

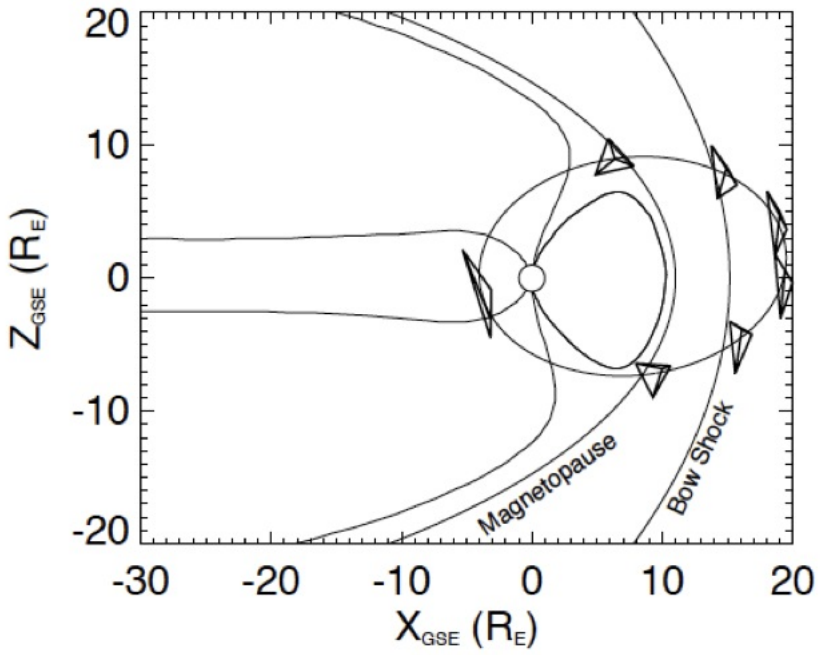

Figure 2.1: Cluster orbits during polar cusp crossings [6].

an orbital period is about 57 hours [5]. The plane of the polar orbit drifts with respect to an inertial frame such that the Spacecraft (SC) can complete a 360° scan of the magnetosphere in one year [2]. The Cluster Spacecraft orbit the Earth in a tetrahedron constellation in which the relative spatial separation between the satellites is variable. This spacecraft configuration allows, for the first time, multi-point observations in three dimensions of plasma structure. The size of the tetrahedron Cluster constellation gradually increases allowing for multi-scale measurements in key regions of the magnetosphere (Figure 2.2). This thesis focuses on the time periods when

the apogee was in the solar wind around the local noon; This covers cusp orbits in years 2001 and 2002 as shown in the Figure 2.2. The separation size of the Cluster quartet has been fixed at around 600 km for the cusp crossing during the first year [5]. The so-called "cusp orbits," which are of the most importance to this thesis, occurs between mid-January and mid-April. The next section describes in more detail the timing analysis technique used to build the data set for this thesis.

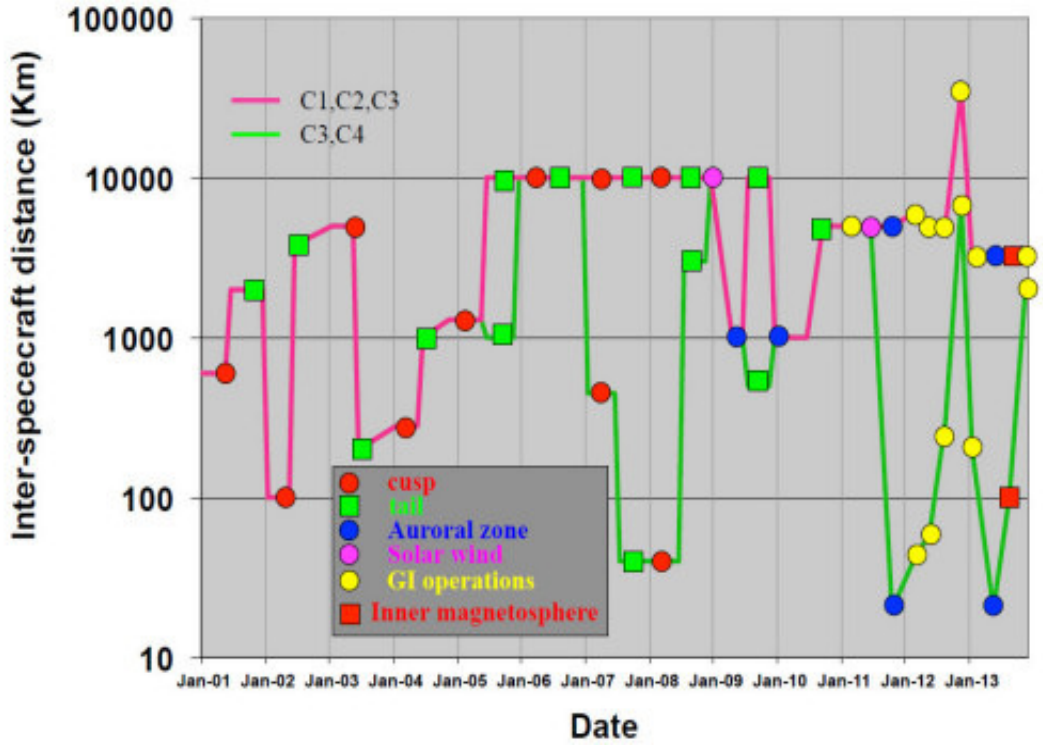

Figure 2.2: The Cluster inter-spacecraft separation strategy allows the plasma structure in the magnetosphere to be investigated on different spatial scales during the mission [6].

2.1.2 Timing Analysis Method for Multi-Spacecraft Data

With the Cluster quartet, full three-dimension shock velocities as well as shock normals were determined for the first time [19].The time delay between successive shock crossings is determined by using the timing analysis, if the bow shock is assumed to be planar and moving with constant velocity at the scale of the Cluster quartet during the time of interest [7]. If the same bow shock passes the cluster quartet, the relative position and the successive time delay can be used to construct the bow shock normal $\hat{\mathbf{n}}$ and velocity $\vec{\mathbf{V}}$ from the solution of the following system [19]:

$$(\vec{\mathbf{V}} t_{\alpha\beta}) \cdot \hat{\mathbf{n}} = (\vec{\mathbf{r}}_{\alpha\beta} \cdot \hat{\mathbf{n}}) \tag{2.1}$$

where $\vec{\mathbf{r}}_{\alpha\beta}$ is the inter-spacecraft separation vector between any two spacecrafts, and $t_{\alpha\beta}$ the time delay between these two spacecrafts for the same bow shock. It is then straightforward to find, the normal vector and propagation velocity along the normal to the shock plane. The spacecraft 3 is usually chosen as a reference satellite, therefore the system of equations 2.1 will be written as follows:

$$\begin{pmatrix} \vec{r}_{13} \\ \vec{r}_{23} \\ \vec{r}_{43} \end{pmatrix} \cdot \frac{1}{V} \begin{pmatrix} n_x \\ n_y \\ n_z \end{pmatrix} = \begin{pmatrix} t_{13} \\ t_{23} \\ t_{43} \end{pmatrix} \tag{2.2}$$

where (n_x, n_y, n_z) are the components of the normal vector $\hat{\mathbf{n}}$, and V is the shock speed. During the time delay t_{13}, the bow shock plane moves along the normal a distance $V(t_1 - t_3)$ between SC3 and SC1, which is equal to the projection of the inter-spacecraft separation $\vec{r}_1 - \vec{r}_3$ onto the normal [4]. This method is used in this thesis for determining the normal and velocity along the normal of the Earth's bow shock. The Timing method assumes that the bow shock structure is planer over the Cluster configuration scale [7]. In order to satisfy this assumption, the cusp orbits in years 2001 and 2002 were chosen such that the spacecraft separation is within a few hundreds of km as shown in the Figure 2.2. The following assumptions are required:

1. The tetrahedron size of the Cluster quartet during configuration during cusp orbits in years 2001 and 2002 is much less than the Earth's bow shock curvature.

2. The shock velocity should remain constant while crossing the Cluster formation.

3. The shock structure is similar for all spacecraft over the interval of crossing.

However, in many cases, shock structures may appear more developed while passing one spacecraft than while passing the others, during the same crossing sequence. During a similar supercritical shock self-reformation cycle, the foot and the overshoot as well the ramp suffer a significant change in terms of

size. For the present work, our emphasis is on the determination of the global motion of the shock front, while the shock kinetic scales are not addressed. The data selection based upon the timing method assumptions is presented in Section 2.4. The next section briefly describes the main instruments that produced the data which were used in the preparation of this thesis.

2.2 Plasma and Interplanetary Magnetic Field Measurements

Data from two different spacecrafts are used in the preparation of this thesis, namely the Cluster and ACE spacecrafts. We are primarily interested in the plasma and the magnetic field measurements. Each Cluster satellite payload supports the same set of eleven instruments, which collect data that can be used to investigate the Earth plasma environment and the solar wind. The ACE spacecraft payload is exclusively devoted to investigate solar wind conditions. In this thesis, data from Cluster/FGM, Cluster/CIS , ACE/MAG and ACE/SWEPAM are used. The plasma data in the solar wind (upstream) are taken from the Cluster/CIS-HIA experiment when it operates in the solar wind mode. In the magnetospheric mode, ACE/SWEPAM data were used. Plasma data from ACE/SWEPAM have been used after introducing the necessary delay to the ACE/MAG time series of the IMF using a visual inspection to compare them with those observed by the Cluster/FGM located upstream of the bow shock. In Section 2.3 more details with examples in the

delay technique are given . The plasma and magnetic data are then used to compute various parameters such as the Mach number in the solar wind, ram pressure and plasma data. In what follows, a short description of each of the instruments is provided.

2.2.1 FGM (Fluxgate Magnetometer)

The four Cluster satellites have identical FGM instruments (Fluxgate Magnetometer) to measure the magnetic field vector at the location of each Cluster spacecraft [1]. The FGM instrument on each spacecraft consists of two triaxial fluxgate magnetometers on one of the two radial booms of the spacecraft and a data processing unit on the main equipment platform [1]. In order to minimize the magnetic background of the spacecraft, one of the FGM sensors is located at the end of one of the two 5.2 m radial booms of the spacecraft and is designated as the primary source of the data, and the other sensor is located at 1.5 m from the end of the boom [12]. The magnetometers measure the three components of the field in seven operating ranges and resolutions designed for different magnetic strengths in different key regions as shown in Table 2.1. Only four (numbered 2 to 5) of these ranges were used on Cluster in flight; the range 7 was used for ground testing [12]. The FGM sensors are capable of sampling the magnetic field vector at the rate of 201.793 vectors/s [1]. This high sampling rate reduced to lower rate for the different telemetry mode constraints to give the highest frequency response for the shortest period. There are two telemetry modes in common use, normal

mode and burst mode. In normal mode operations, FGM transmit 22.416 vectors/second to the ground station, and in the case of burst mode operations about 67.249 vectors/seconds is transmitted [11]. This thesis is based

Range Number	**Range**	**Resolution**
2	-64 nT to + 63.79 nT	7.8×10^{-3} nT
3	-256 nT to + 255.87 nT	3.1×10^{-3} nT
4	-1,024 nT to + 1.023.5 nT	0.125 nT
5	-4,096 nT to + 4,094 nT	0.5 nT
6	-16,385 to + 16,376 nT	2 nT
7	-65,536 to + 65,536 nT	8 nT

Table 2.1: FGM Operating Ranges (numbered 2 to 5 were used) [12].

on magnetic field measurements from the Cluster FGM experiment when the Cluster spacecrafts were crossing Earth's bow shock. The high time resolution data was downloaded from the Cluster Active Archives on the ESA website. In all bow shock crossings, a time resolution of 5 vectors/second (5 Hz) was used. The use of 5 Hz data will be discussed in more details in Section 2.4.

2.2.2 CIS (Cluster Ion Spectroscopy)

The Cluster Ion Spectrometer (CIS) experiment [8] consists of two different ion instruments both capable of measuring cold and hot ions of Maxwellian and non Maxwellian populations from the solar wind, the magnetosheath, and the magnetosphere with a time resolution of one spacecraft spin (4 sec) [8]. The two sensors are a Hot Ion Analyzer (HIA) sensor and a time-

of-flight ion Composition and Distribution Function(CODIF) sensor. Each Cluster spacecraft carries a CIS experiment. The CIS experiment on SC2 is not operational. The CODIF instrument onboard Cluster SC1 has been switched off since October 25, 2004, due Microchannel Plate (MCP) high voltage anomaly [13]. The CIS experiment has been operating nominally on SC3 until it was switched off on November 11, 2009, and the HIA instrument has been switched off on Cluster SC4, but the (CODIF) on spacecraft SC4 is in normal operations [13]. On Table 2.2 the status of each of the CIS instruments in each spacecraft is described. The Cluster/CIS hot ion ana-

Instrument	**SC1**	**SC2**	**SC3**	**SC4**
CODIF	Operations until Oct.2004	Not Operational	Operations until Nov.2009	Normal Operations
HIA	Normal Operations	Not Operational	Operations until Nov.2009	Not Operational

Table 2.2: CIS Instrument Status [13].

lyzer (HIA) is a top-hat electrostatic analyzer which measures particles in the energy range 0.005 - 32 KeV, and the Cluster/CIS Composition and Distribution Function(CODIF) combines a top-hat electrostatic analyzer with a time-of-flight section to measure the major species H^+,He^+,He^{++} and O^+ over the range 0.02-38 KeV/q. Both instruments have $2 \times 180°$ field of view (FOV) section parallel to the spin axis, with two different sensitivities with an approximate ratio of 25, with the high-Geometry or high sensitivity (HS) and low-geometry or low sensitivity (LS) sides looking in opposite directions.

The low-g side allows for detection of the solar wind beam and magnetosheath fluxes without saturation, and is divided such that it has 8 central anodes around the spin plane, 5.625° each, the remaining 8 sectors with a resolution of 11.25°, that allows for high resolution measurements of solar wind ion distributions. There are two sections with 22.5° resolution have been left blank to avoid interference between the high sensitivity and the low sensitivity of the Cluster/CIS instruments. The high-Geometry side or the high sensitivity (HS) side is divided into 16 anodes, 11.25° each; the high-Geometry is well suited for measuring the orders of magnitude lower fluxes of upstream ions [8]. The Cluster/CIS instruments have a large amount of flexibility in the selection of the operational mode and the reduction of the data necessary to fit the normal or burst telemetry. Only measurements from the low–geometry or low sensitivity (LS) factor analyzer (HIA instruments), when available, are considered in this thesis . When in the solar wind mode of operations, the Cluster/CIS-HIA analyzer captures the velocity space center of the solar wind beam. The plasma data in the solar wind (upstream) are taken from the Cluster/CIS-HIA experiment when it operates in the solar wind mode. In the magnetosheath mode case, The ACE-SWEPAM have been used instead of Cluster/CIS-HIA.

2.2.3 ACE/SWEPAM

When the Cluster/CIS-HIA operates in magnetospheric mode, the plasma data are taken from the solar wind electron alpha monitor ACE/SWEPAM.

The ACE/SWEPAM provides solar wind observations for the ACE spacecraft. These observations provide solar wind composition measurements and allow the direct examination of numerous solar wind phenomena such as coronal mass ejections, interplanetary shocks and solar wind structure. These observations were made from the Sun-Earth L-1 orbit. The ACE/SWEPAM consists of two separate instruments; each instrument has an electrostatic analyzer (ESA), one for electron measurements and one for ion measurements. The solar wind data with 64 s time resolution were downloaded from the Coordinated Data Analysis Web (CDAWeb) [14]. Plasma and magnetic field data are then used to compute various parameters such as Mach number in the solar wind, ram pressure and plasma beta.

2.2.4 ACE/MAG

The ACE magnetic field experiment (MAG) measures the interplanetary magnetic field (IMF) and establishes the large scale structure near the Sun-Earth L-1 orbit. The basic instrument is a twin triaxial fluxgate magnetometer system. Each of two identical sensors is set on booms that extend past the end of diametrically opposite solar panels [15]. The interplanetary magnetic field (IMF) data of 1 s time resolution and level 2 was downloaded from the Coordinated Data Analysis Web (CDAWeb). The IMF time series observed by ACE/MAG were delayed by using a visual inspection to compare them with those observed by Cluster located upstream of the bow shock; more details about this technique with examples will be discussed in

the next section.

2.3 ACE - Cluster Time Delay

The investigation of Earth's bow shock requires a careful determination of the solar wind plasma conditions during a cluster bow shock crossing. The ram pressure ρ as well as the Alfvèn Mach number M_A are particularly needed in order to investigate the Earth's bow shock shape and dynamics. When Cluster-CIS was not operating in solar wind mode during periods of interest for this thesis, the ACE-SWEPAM data was used instead, after determining delays required for the solar wind to propagate to the bow shock. The delays were obtained by visual comparison of the magnetic field magnitude time series from ACE-H0-MFI and Cluster-FGM, and by estimating the time delay between ACE & Cluster given that both the solar wind speed, and the distance between the ACE and Cluster-3 spacecrafts were known. In this case, the determination is precise only when the solar wind perturbations propagate radially. In the present study and for each event, the time delay is determined by using visual inspection and by evaluating it from the spacecraft relative locations, respectively. In most cases, the differences are within few minutes indicating that in general, the solar disturbances propagate radially. An example is illustrated on Figure 2.3. The panel *c* shows the magnetic field time series data from ACE and Cluster-3 shifted by approximatively 0.587 hours obtained by estimating the flat delay between ACE

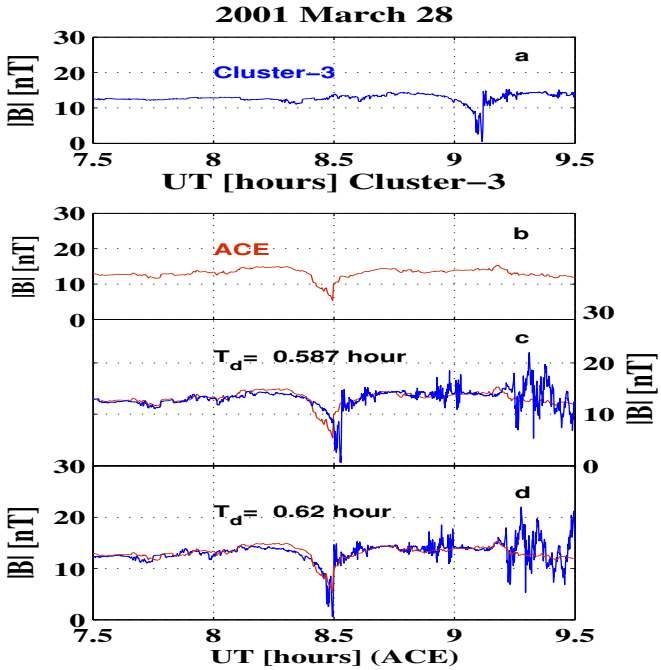

Figure 2.3: An example showing the time delay difference between ACE and Cluster SC. Panel *a* shows the magnetic field data time series from Cluster-3. Panel *b* shows the magnetic field data time series from ACE. Panel *c* the data is shifted by 0.587 hours obtained from flat estimation. Panel *d* same as panel *c* but the data is now shifted by 0.620 hours obtained after visual inspection of the magnetic field structures.

& Cluster-3, which assumes that the plasma element and the frozen magnetic field are propagating at constant speed along the Sun-Earh line; the estimated flat delay is given by

$$t_{flat} = \frac{\Delta_{ACE-SC3}}{V_x}$$

where $\Delta_{ACE-SC3}$ is the distance of separation between the spacecraft along the x-axis, and V_x is the solar wind speed along the X_{GSE} direction [16]. For the illustrated event of March 28, 2001, the solar wind speed was 598 km/s and the distance between ACE and Cluster-3 was about 1.2634×10^6 km. The top two panels in the Figure 2.3 represent the magnitude of the magnetic field measurement from ACE and Cluster-3, respectively. Panel c displays both measurements with time-shifted Cluster data equals to $t_{flat} \sim$ 0.587 hours. A visual adjustment of the time series in order to obtain the best possible overlap of the magnetic field structure is satisfactory. The result is shown on the panel d. The difference between the observed and the estimated (t_{flat}) time delays is $\sim$ 2 minutes. However, we should mention that once the time delay for the best overlap is obtained, significant departures from the two time-series overlap are not noticeable for times within an interval smaller than $\pm$6 minutes. Another example illustrating how the time delay between ACE and Cluster 3 is obtained is shown on Figure 2.4. The top two panels display the ACE and Cluster-3 magnetic field magnitude data recorded on March 19, 2001 between 1800 UT and 2400 UT. As shown, successive bow shock crossings were registered by the Cluster spacecrafts. The third panel shows both time series with Cluster data shifted by approximatively 0.850 hours. Assuming that the IMF variations propagate radially between ACE and Cluster, the prediction of the flat time delay is $\sim$ 0.845 hours, which is consistent with the visual inspection. Clearly, when Cluster-3 is in the solar wind, the overlap of the two time series is quite satisfactory as shown

by the bottom panel where the magnetosheath data were removed. The

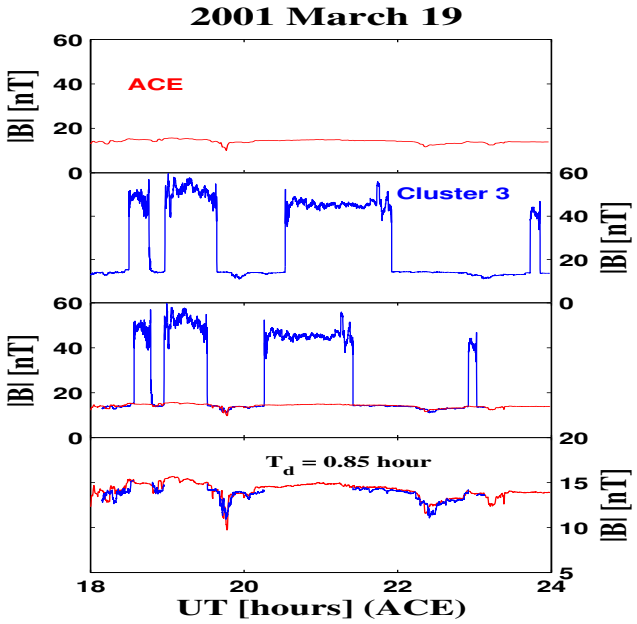

Figure 2.4: An example showing how the time delay between ACE and Cluster is obtained. The top two panels show the magnetic field magnitude data time series from ACE and Cluster-3, respectively. The third panel shows both profiles with the Cluster-C3 data shifted by 0.850 hours from its original base, while the bottom panel is the same as the panel above with magnetosheath data removed.

third example is illustrated on Figure 2.5. Similar to previous examples, the top two panels show the ACE and Cluster-3 magnetic field data recorded on April 05, 2001, between 1400 UT and 2200 UT. The third panels shows two time series with Cluster-3 data shifted by 0.6313 hours, which is consistent with the flat delay prediction that gave ~ 0.6292 hours.

For each event in the data set, a similar time delay analysis between ACE and Cluster was conducted. Only 74 shock events have been found (among

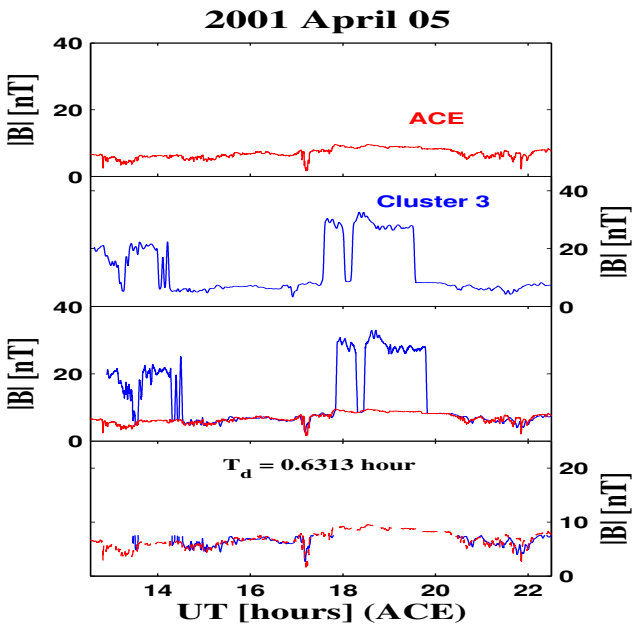

Figure 2.5: Second example showing how the time delay between ACE and Cluster is obtained. Same as Figure 2.4 with the Cluster-C3 data shifted by 0.631 hours from its original base.

133) where ACE data were available. Once the time delay is determined, the solar wind plasma data are obtained from ACE-SWEPAM. The ram pressure ρ and Mach number M_A are then derived. For the latter estimation, a helium density of 5% of the proton density was considered for all events [18]. Studies have established that there is a dependence of the helium to hydrogen abundance ratio (He/H) upon the solar cycle and the solar wind speed. Our choice of helium density is consistent with the analysis of data from WIND Solar Wind Experiment, which reported that, for a typical solar wind speed, the He/H ratio varies, in a statistical sense, from 2% at solar

minimum to about 5% at solar maximum [17] in early 2000, which coincides with the time period chosen to analyze the Cluster data used in this thesis.

2.4 Events Selection

The timing method analysis is applied to the interplanetary magnetic field data measurements from the Cluster FGM instrument [1]. For all crossings, a time resolution of 5 vectors/s of the interplanetary magnetic field data was downloaded from the Cluster Active Archives on the ESA website. The ramp profile observed features, including the small scale fluctuations, depend upon the time resolution of the measurements. The use of 5 Hz data is quite satisfactory when the spatial ramp thickness is not too small. However, some recent studies have shown that the thickness of the shock ramp could be very small and highly dynamic [34, 21] and this could be problematic for our event data selection. However, we should emphasize that the present study focuses on the global motion of the shock front while ignoring the physics at the kinetic scales. The time delay between successive crossings is determined by using the conventional technique of timing difference [19], whose domain of validity and restrictions were discussed above. This method assumes that the bow shock structure is planar on average, similar for all spacecrafts, and that the shock velocity is constant while crossing the cluster formation. However, in many cases, shock structures may appear more complex at one spacecraft and not so complex at the others, during the same crossing sequence. For

instance, during a same supercritical shock self-reformation cycle, the foot and the overshoot as well the ramp suffer a significant change in terms of size. When the shock ramp slopes and thicknesses are different, we use the superimposition of the middle of the ramp as a criterion to determine the successive time delays. Moreover and as mentioned in Section 2.1.1, in order to avoid shock shape distortions, only orbits with small spatial separations between satellites were considered. This covers cusp orbits in years 2001 and 2002 as shown in Figure 2.2. For each crossing, an automatic procedure computing the cross-correlation of the interplanetary magnetic field IMF time series is applied to find the accurate time delay between the various spacecraft signals. Cluster-3 is taken as the reference spacecraft. In the case when the cross-correlation analysis provides an ambiguous and not so clear peak in the correlation function between the successive crossing of Cluster Spacecraft signals, the event is eliminated from our data selection. Sources of errors in the shock normal determination originate from uncertainties in the times when the correlation function between the spacecraft data peaks during the crossing window. These uncertainties have been estimated and presented in Appendix C. Sample shock crossings events are presented in the next section; this includes the selected and rejected events.

2.4.1 Selected Events

More than 400 shock crossings, which occurred between 2001 and 2002 were analyzed, and only 133 shock crossings have been chosen based upon the

timing analysis results. To improve the determination of the time delay between two successive shock crossings, high frequency-IMF fluctuation, when present, are removed or suppressed using appropriate techniques such a low band-pass filtering or moving averages. The most important criterion for choosing or eliminating events is set by the result of the cross-correlation analysis. The data set used in this thesis has 51 "clean" crossings in which no subsequent data analysis has been carried out. For the remaining events (82), significant IMF fluctuations are present and were smoothed out using either the Fast Fourier Transform or a running average.

Figure 2.6 illustrates an example of magnetic field profile measured during a clear Cluster bow shock crossing on March 31, 2001 at 17:14:39 UT; the spacecraft interspace separation was of the order of 600 km. First, the shock is observed by Cluster-3 (C3), followed by C1, C2 and C4, respectively. There is no evidence for the presence of significant differences in the shock structure for this event; similar ramp, clear foot and overshoot are observed by the four spacecrafts. The cross-correlation analysis shows clear peaks between the spacecraft data during the crossing window when the IMF time-series are shifted by an amount equal to the time delay found above. We obtained a satisfactory overlap of the middle of shock ramps as illustrated in the middle panel of Figure 2.7. For this event, the results of the timing analysis as well as the plasma condition and the shock geometry are given on Table 2.3 A second "clean" example of shock crossing by the Cluster-quartet, which occurred on March 28, 2001 at 13:12:22 UT, is shown on the top panel of

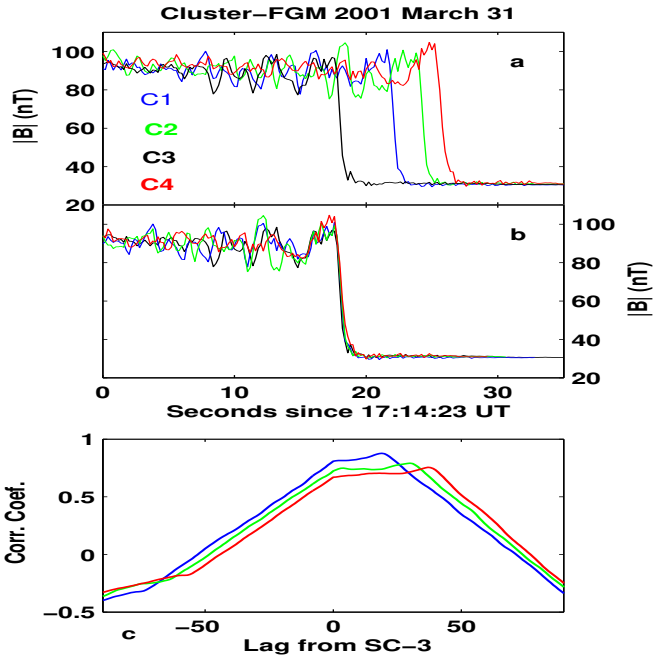

Figure 2.6: An Example of a clean bow shock crossing; the time series correspond to the magnetic field from Cluster/IMF. On March 31, 2001 at 1714:39 UT.Successive crossings along the spacecraft trajectories are indicated in color on the top panel. The middle panel shows the same profile shifted in time according to lags Δt obtained from cross-correlation analysis. The bottom panel provides those cross correlation values as function of lag.

Shock 2001 03 31/ 1714:30 UT	
$\hat{n}$	0.959 -0.139 0.247
M_A	1.74
β	0.0192
V_{sh}	-66 km/s
θ_{Bn}	86°

Table 2.3: Shock parameters

Figure 2.7; the spacecraft spatial separation was of the order 600 km. As was the case for the first example, there is no evidence for a presence of sub-

stantial differences in the shock structure for this event. The results of the cross-correlation analysis, shown in the bottom panel, indicate a very clear peak. The time delay obtained by the automatic procedure outlined above and from computing the cross-correlation of the interplanetary magnetic field IMF time series are similar. For this event, the results of the timing analysis

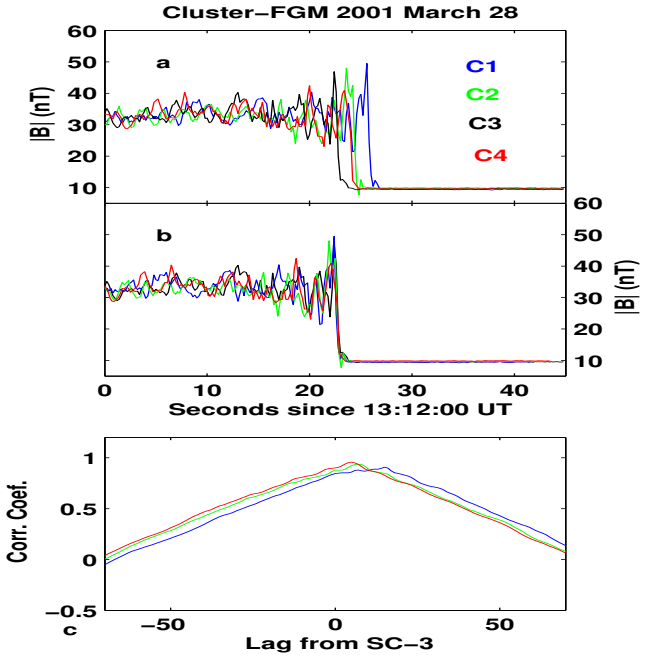

Figure 2.7: A Second Example of a clean bow shock crossing same as Figure 2.6. Event of March 28, 2001 at 1312:22 UT.

as well as the plasma conditions and shock geometry are given on Table 2.4. Finally, Figure 2.8 illustrates a third example of a "clean" crossing that occurred on March 19, 2001 at 19:48:30 UT. The shock parameters, the plasma conditions and the shock geometry are given in Table 2.5. For all of the

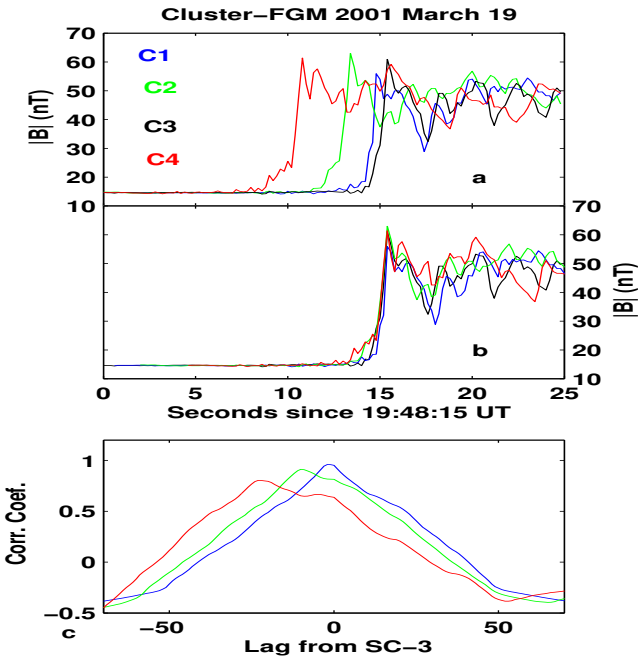

Figure 2.8: Third Example of a clean bow shock crossing on March 19, 2001 at 1948:30 UT.

Shock 2001 03 28/ 1312:22 UT	
$\hat{n}$	0.986 -0.130 -0.103
M_A	8.84
β	0.130
V_{sh}	-202 km/s
θ_{Bn}	79°

Table 2.4: Shock parameters

events listed, the performance of the automatic procedure computing the cross-correlation results was checked by visual inspection. The uncertainty of the time delays is less than two time lags as related to the position of the peak of the correlation function. For each selected shock crossing, the corre-

Shock 2001 03 19/ 1948:30 UT	
$\hat{n}$	0.819 -0.089 0.565
M_A	6.94
β	0.0500
V_{sh}	105 km/s
θ_{Bn}	69°

Table 2.5: Shock parameters

sponding plasma data were collected as explained in the previous subsection. As mentioned above, 82 shock crossings show significant fluctuations in the magnetic field magnitude shock profiles. For these events, a filtering technique is systematically applied prior to applying the timing analysis. Two different filters were used; the first one is based on moving averages whereas the second uses a low-pass filter using the FFT technique. Depending on the event, one filtering technique is selected and applied rather than the

other. The inclusion of such "noisy" shock profiles allows to extend the data selection to include oblique shocks with relative θ_{Bn} significantly off perpendicularity. An example of such shock crossing by the Cluster-quarter where IMF fluctuations are present is illustrated on the top panel of Figure 2.9; for this event, the spacecraft separation distance was in the order of 150 km. For this crossing, significant high frequency fluctuations in the magnetic

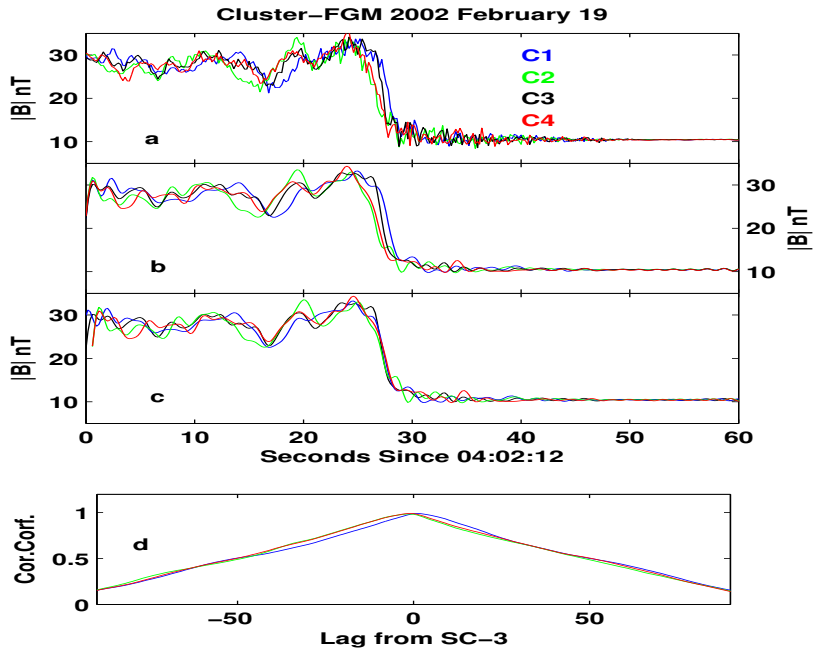

Figure 2.9: An Example of a bow shock crossing where low band-pass filtering is applied on the time series of IMF measurements. Panel (a) shows the IMF measurements while panel (b) shows the same time series where the high frequency fluctuations are suppressed. Panel (c) shows the same time series as in panel (b) but shifted in time according to lags Δt, obtained from cross correlation between each spacecraft time series and that of the reference spacecraft S/C3. The bottom panel provides those cross correlation values as function of lag.

field are present, particularly in the foot and the ramp. In order to eliminate these fluctuations to allow for a better determination of the crossing time differences, the Fast Fourier Transform technique (FFT) was applied for the time interval of interest. This conventional technique is reliable for as far as eliminating unwanted high frequency signals is concerned. If the $x\,(n)$ is the input signal and $X\,(m)$ the signal in frequency domain:

$$X\,(m) = \sum_{n=0}^{N-1} x\,(n)\, e^{-f2\pi nm/N}$$

where the n is the index of the input signal and m is the index of the output signal. A new profile was obtained by inverting the Fast Fourier transformed data with a high frequency cut-off. Usually a cut-off frequency of 2 Hz is used which sufficient to significantly reduce whistler activity. The resulting magnetic field profile is shown on panel b of Figure 2.9. We then compute the cross correlation function of the newly transformed data in order to determine the crossing time delays (bottom Figure 2.9). Panel c of Figure 2.9 shows the time shifted magnetic field data according to the cross correlation function results. For this event specifically, and because the ramp's slopes are significantly different, only the middle of the ramps overlap satisfactorily. A second example on which the FFT technique was applied on IMF measurements is given on Figure 2.10. As was the case in the previous example, only the middle of the ramps satisfactorily overlap as shown in the Figure 2.10 and after shifting the time delays according to the cross correlation results.

As mentioned above, a second filtering technique based on 'moving averages'

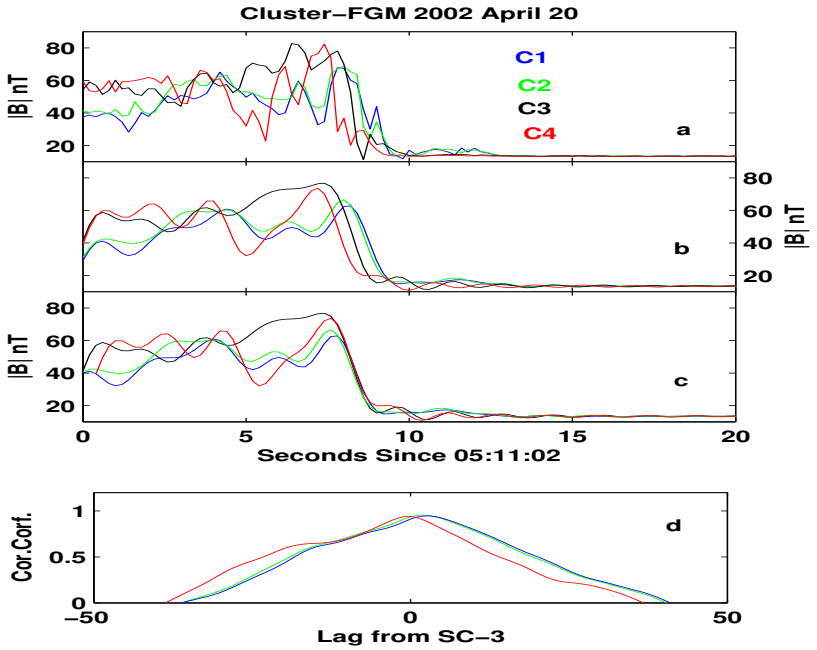

Figure 2.10: A Second example of using low band-pass filtering on April 20, 2002.

was applied to a certain number of shock crossing profiles. If x is the input signal, y is the output signal, and M is number of points used in the moving average (usually range between 5 to 9 points).

$$y(n) = \frac{1}{M} \sum_{k=-(M-1)/2}^{(M-1)/2} x(n-k)$$

A first example to which the technique was applied is shown on Figure 2.11. The top panel shows the time series of IMF measurements with Cluster FGM on March 19, 2001; the bow shock crossing ocurred at 23:46:18 UT. In panel

b the fluctuations in the IMF signals have been suppressed after applying the moving average technique. The cross-correlation was then performed on the averaged signals as shown on the bottom of Figure 2.11. Again, when time shifted according to the cross correlation between each spacecraft signal with the Cluster-3 signal as a reference, we obtain a good overlap of the middle of the shock ramps. A second example in which the moving average technique

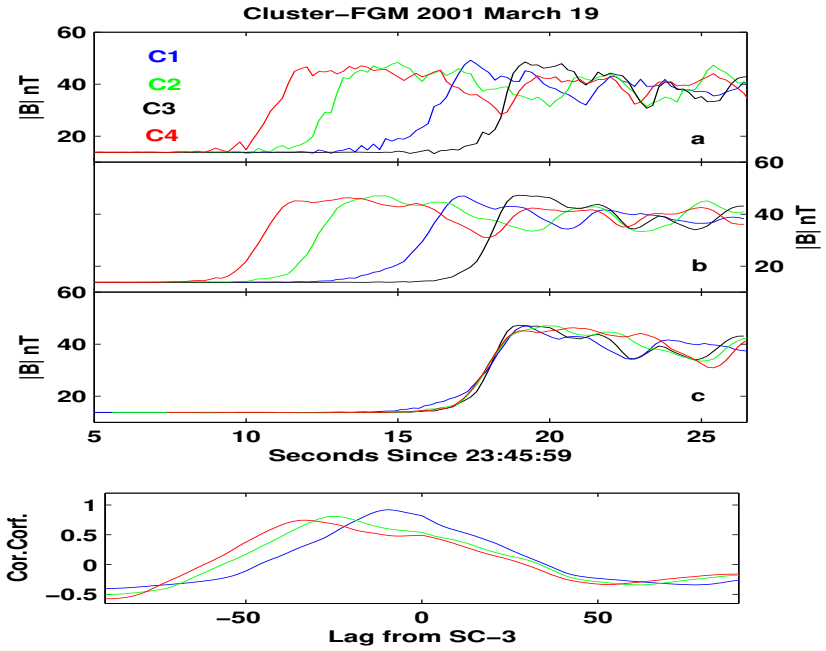

Figure 2.11: An Example of bow shock crossing in which the moving average technique is applied on the time series of IMF measurements. Panel (a) shows the IMF measurements and panel (b) shows the same time series where the hight frequency fluctuations are suppressed. Panel (c) shows the same time series of IMF as in panel (b) but shifted in time according to lags Δt resulting from cross correlations between each spacecraft time series and that of S/C3. The bottom panel provides those cross correlation values as function of lag.

was applied to the data is illustrated by Figure 2.12. This event occurred on

April 20, 2002, and the shock crossing of Cluster-3 was at 04:53:19 UT. For this event, the ramp's slopes are significantly different, only the middle of the ramps satisfactorily overlap as shown in the bottom panel of Figure 2.11 and Figure 2.12.

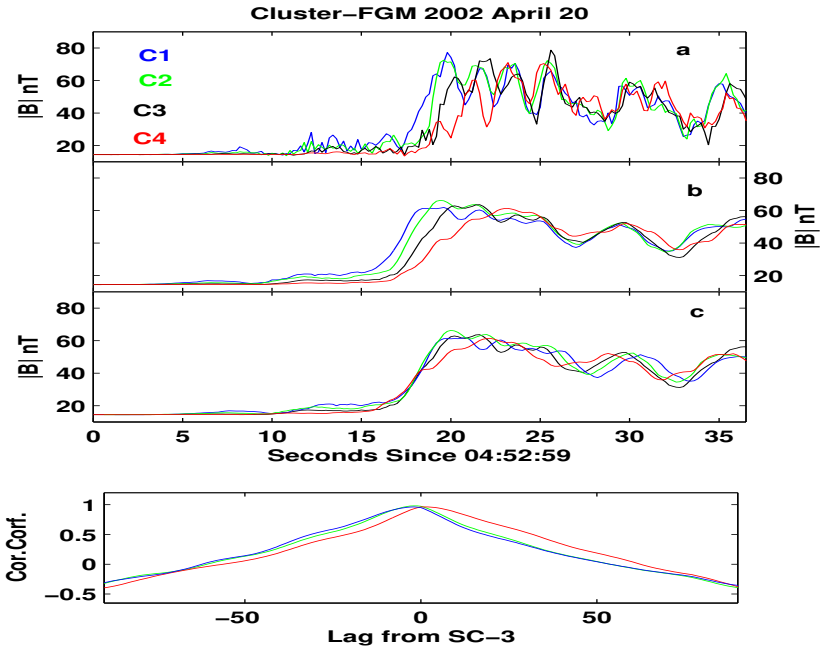

Figure 2.12: A second example of using moving averages on April 20, 2002.

2.4.2 Event Selection Criteria

The main criterion for event selection is based on the results of the cross-correlation analysis. The selected events are such that the correlation function shows an unambiguous peak. Once the time delays are obtained, we always check the consistency of the results, i.e whether the middle of the shock

ramps overlap satisfactorily. In many events when the magnetic field shock structures are not alike for all the Cluster-quartet, the cross-correlation analysis provides inconclusive results, and such events are eliminated from our data base. An example of an eliminated event is shown on Figure 2.13. The shock crossing occurred on January 21, 2001, at 02:25:52 UT. The maximum peaks of the automatic procedure computing the cross-correlation are ambiguous as indicated on Figure 2.13; the cross-correlation function maximum between Cluster-3 and Cluster-2 is not detectable. This shock is probably accelerating, which in turn caused a structure change in the shock between the two spacecrafts. As shown on panel a, there exist significant high frequency fluctuations in the magnetic field, particularly in the foot and the ramp. In order to remove the high frequencies, we performed a moving averages filter on the time series of the magnetic fields as shown in panel b of Figure 2.13. The cross-correlation analysis was applied on the new profile to determine the crossing time delays (bottom Figure 2.13). After shifting the time series panel c, it is clear as it appears from Figure 2.13 that the overlap of the shock ramps is poor.

2.4.3 Observation Positions and Database

In the present work, we have selected 133 events. For each event, the shock normal as well as the plasma conditions were determined. We then derived the corresponding shock velocity and shock geometry θ_{Bn} (angle between the shock normal and the upstream magnetic field) as well as the ram pressure ρ

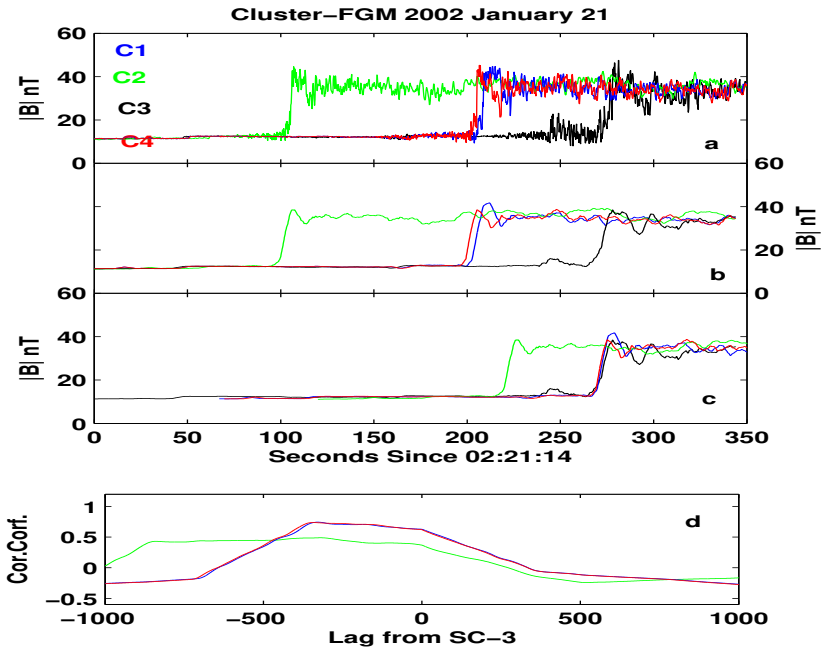

Figure 2.13: An Example of a non selected event on January 21 2002. In panel (a), the IMF shows fluctuations in the shock structure. In panel (b), the IMF fluctuations have been suppressed using moving averages. Panel (c) shows the same time series of IMF as in panel (b) shifted in time according to lags Δt obtained from the cross correlation analysis between each spacecraft time series using S/C3 as a reference.

and the Alfvèn Mach number M_A. Using Cluster-3 as the reference satellite, the positions of the bow shock crossings used in the present study as observed on Cluster-3 are shown in the Figure 2.15. In addition, the distribution of the angle θ_{Bn} is shown in Figure 2.16. Most events occur at quasi-perpendicular shocks ($\theta_{Bn} \geq 45°$), although a significant number of crossings are associated with a quasi-parallel geometry ($\theta_{Bn} \leq 45°$). Finally, the distributions of M_A and ρ are given in Figures 2.16 and 2.17, respectively. These distributions

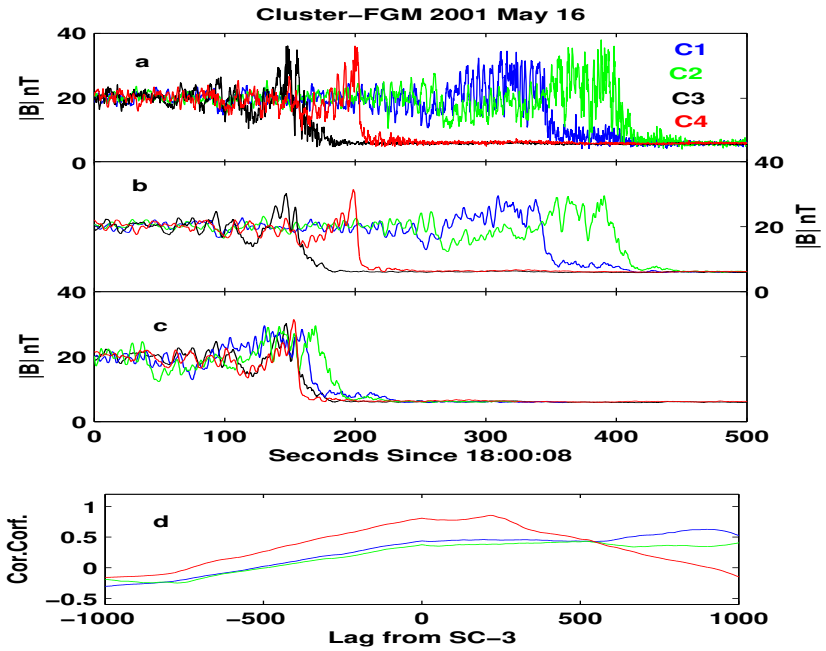

Figure 2.14: Second example of eliminated event on May 16, 2001. Bow shock crossing at 18:02:35 UT.

are typical of solar wind.

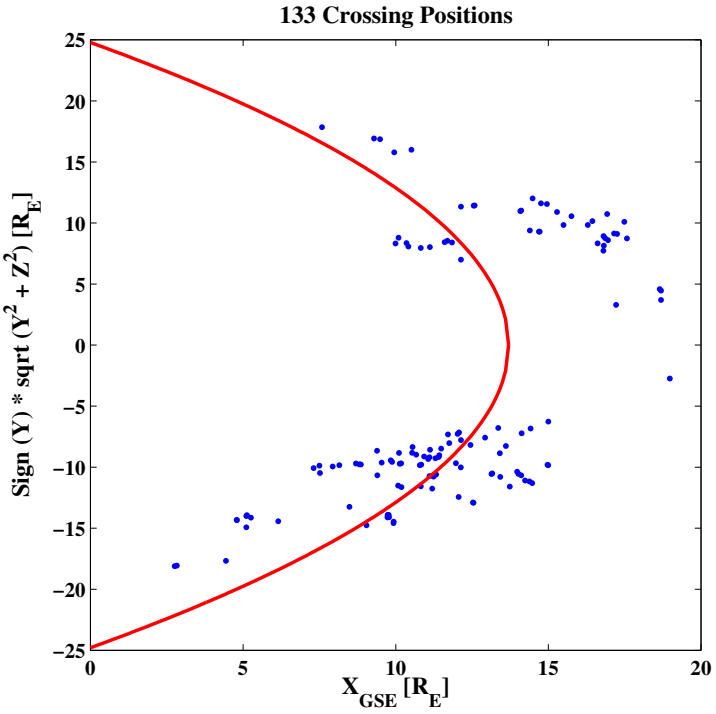

Figure 2.15: Satellite Crossing Positions in The GSE frame of reference. The red curve represents a nominal bow shock

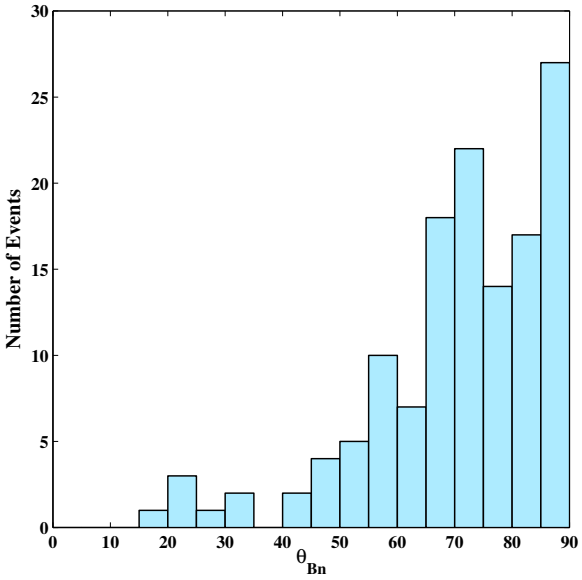

Figure 2.16: Histogram for θ_{Bn}.

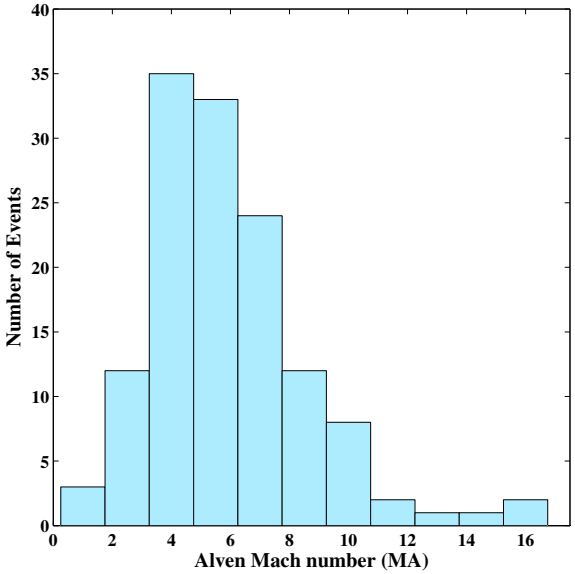

Figure 2.17: Histogram for Mach number.

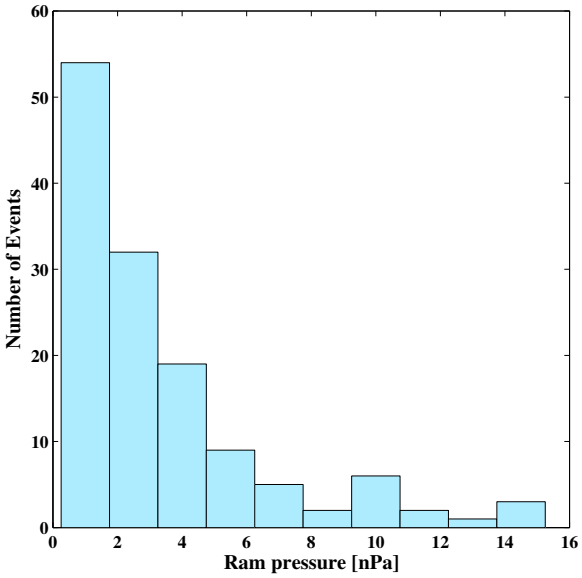

Figure 2.18: Histogram for Ram pressure.

Chapter 3

Standoff Distance and Shape of the Earth's Bow Shock

3.1 Standoff Position

In this section the results of the timing analysis are primarily used to investigate the standoff position of the bow shock. The overall shape of the shock is also addressed. Understanding the location of the shock nose is important to grasp the impact of the solar wind ram pressure as well of the Mach number on the size of the shock. In this context, the first empirical studies have shown that an object (obstacle) moving in a gas with a supersonic speed produces a shock front located a distance Δ from the obstacle such that [22]:

$$\frac{\Delta}{D_o} = 1.1\frac{\rho_1}{\rho_2} \tag{3.1}$$

where D_o is the radius of the obstacle and ρ_1 (ρ_2) is the upstream (downstream) gas density. In a semi-analytical work, Spreiter et al. [23] confirmed Seiff's results. Moreover, from gas dynamics theory of gas compressibility, it can be shown that the upstream and the downstream density ratio is related to the upstream Mach Number M_1 through equation [62]:

$$\frac{\rho_1}{\rho_2} = \frac{(\gamma - 1)M_1^2 + 2}{(\gamma + 1)M_1^2} \tag{3.2}$$

where γ is the ratio of specific heats; a numerical value of 5/3 is usually adopted. From equations 3.1 and 3.2, the shock nose distance a_s from the centre of the obstacle is then obtained:

$$\frac{a_s}{D_o} = 1.1\frac{(\gamma - 1)M_1^2 + 2}{(\gamma + 1)M_1^2} \tag{3.3}$$

This last expression raises some difficulties in the case of low Mach number shocks; particularly in the case $M_1 = 1$ (no shock) where a_s remains finite. Farris and Russel [48] modified Spreiter et al.'s[23] work as an attempt to account for Mach number = 1 shocks, and at the same time applied the model to the Earth's bow shock. In Farris and Russel's model, the subsolar distance $a_s(R_E)$ is given by the following expression:

$$a_s = D_o \left[1 + 1.1\frac{(\gamma - 1)M_1^2 + 2}{(\gamma + 1)(M_1^2 - 1)}\right] \tag{3.4}$$

This expression shows that the distance of the shock dependents on the distance D_o from Earth of the magnetosheath and the upstream Mach numberM_1. The size of the obstacle in units of Earth's radius R_E is given by the following equation (see Appendix C for the derivation):

$$D_o = 9.47 \left(\frac{f^2}{k}\right)^{1/6} \left(\frac{2}{p}\right)^{1/6} R_E \tag{3.5}$$

where the ram pressure p is expressed in nPa, and the parameters f and k reflect the effective portion of the solar wind dynamical pressure as applied to the magnetosphere and the effects of the electric currents in the magnetopause, respectively. The numerical value of f^2/k is in the range 1.77 - 2.25 [26]. In the solar wind medium, three types of Mach numbers could be considered: the sonic or acoustic, Mach number M_S, the Alfven Mach number M_A and the magnetosonic Mach number M_{MS}. Up to date, there are no convincing arguments for the choice of Mach number that would account satisfactorily for the observations. For as far as our study is concerned, the logical choice is the Alfven Mach number M_A, which is dictated by the study of Merka [27] who found a better fit of the 2D shock surface using a shock model with M_A. Therefore the subsolar distance $a_s\,(R_E)$ in expression 3.3 becomes:

$$a_s = 9.47 \left(\frac{2f^2/k}{p}\right)^{1/6} \left[1 + 1.1\frac{(\gamma-1)M_A^2 + 2}{(\gamma+1)(M_A^2-1)}\right] \tag{3.6}$$

A second model for the the bow shock subsolar location was reported by Shue et al [28]. Using several bow shock crossings observed by ISEE 1&2,

AMPTE/IRM and IMP 8 satellites, the authors adjusted the magnetoppause position by introducing the effects of the IMF B_z component. Using a linear dependence upon B_z, the authors fitted the data in order to obtain the best match with the observations. By imposing pressure balance at the magnetopause, the authors were able to fit the two parameters used in the model using the solar wind ram pressure and the interplanetary magnetic field (IMF) B_z.

They obtained a final form for the fit with coefficients for the size and shape of the magnetopause that is given by:

$$D_o = \frac{1}{p^{1/6.6}} \left(11.4 + \eta_z B_z\right) \tag{3.7}$$

$$\eta_z = \begin{cases} 0.013 & \text{when } B_z \geq 0 \\ 0.140 & \text{when } B_z < 0 \end{cases}$$

Equation 3.7 indicates that when the interplanetary magnetic field IMF is southward (northward) the magnetopause moves inward (outward), which in turn induces a decrease (increase) of the bow shock standoff distance. Using Equation 3.7, a so-called "MHD model" for the shock standoff distance is obtained:

$$a_s = \frac{1}{p^{1/6.6}} \left(11.4 + \eta_z B_z\right) \left[1 + 1.1 \frac{(\gamma - 1)M_A^2 + 2}{(\gamma + 1)(M_A^2 - 1)}\right] \tag{3.8}$$

Based on equations 3.6 and 3.8 the shock standoff distance can be predicted

given the solar wind plasma and the magnetic field conditions are known. Our purpose now is to compare the above determinations with the subsolar distance obtained from the timing analysis. Maksimovic et al. [54] were the first to use the shock normal determination to predict the bow shock standoff distance. The method requires the choice of a statistical bow shock model. It is generally accepted that conic surface sections provide a good approximation for these models. Because both the hyperboloid and the ellipsoid models entail an overdetermination of the problem, we are left with a paraboloid model [30]. The standoff distance a_{st}, in terms of the shock normal components (n_x,n_y,n_z), and spacecraft position (x, y, z) at the shock crossing location are derived below. If the shock is ideally represented by a paraboloid of revolution $\phi(x, y, z)$:

$$\phi(x, y, z) = x - a_{st} + b_{st}\left(y^2 + z^2\right) = 0 \tag{3.9}$$

For a given point on the surface, the normal is given by

$$\hat{n} = \frac{\vec{\nabla}\phi(x, y, z)}{\left|\vec{\nabla}\phi(x, y, z)\right|} = \frac{1}{\sqrt{1 + 4b_{st}^2\left(y^2 + z^2\right)}} \begin{pmatrix} 1 \\ 2b_{st}y \\ 2b_{st}z \end{pmatrix} \tag{3.10}$$

or

$$n_x = \frac{1}{\sqrt{1 + 4b_{st}^2\left(y^2 + z^2\right)}} \tag{3.11}$$

Using Equations 3.9 and 3.11, we obtain the standoff distance a_{st} in terms

of n_x:

$$a_{st} = x + \frac{\sqrt{(1 - n_x^2)\,(y^2 + z^2)}}{2n_x} \tag{3.12}$$

In equation 3.12, the spacecraft position components (x, y, z) as well as the shock normal components (n_x, n_y, n_z) are given in the Geocentric Polar Ecliptic (GPE) system of coordinates in which the solar wind is purely radial [31]. The timing standoff distance a_{st} is plotted versus the gas dynamics (Equation 3.6) and MHD (Equation 3.8) standoff distances on the top and bottom panel of Figure 3.1,respectively. For a_s, we have adopted $f^2/k = 1.77$.

Figure 3.1 shows a significant dispersion around the line of slope one in both the gas dynamics and the magnetohydrodynamics models, although a relatively large number of events compare well between the three standoff distance determinations. The error bar associated with each numerical a_{st} value is based on an uncertainty of two time-lags in the determination of the crossing time delays between the Cluster spacecrafts (see Appendix A for more details how uncertainties are derived). Overall, we have found no significant qualitative difference with the results obtained from the comparison of the two standoff distance models the gas dynamic a_s (GD) equation 3.4 and the magnetohydrodynamics a_s (MHD) equation 3.6 with the standoff distance a_{st} derived from the timing normal equation 3.9.

Pursuing our analysis further, the distribution of the difference between the two standoff distances, namely the gas dynamics a_s and the standoff distance a_{st} from the timing normal derivation 3.9, is given in the Figure 3.2. Clearly,

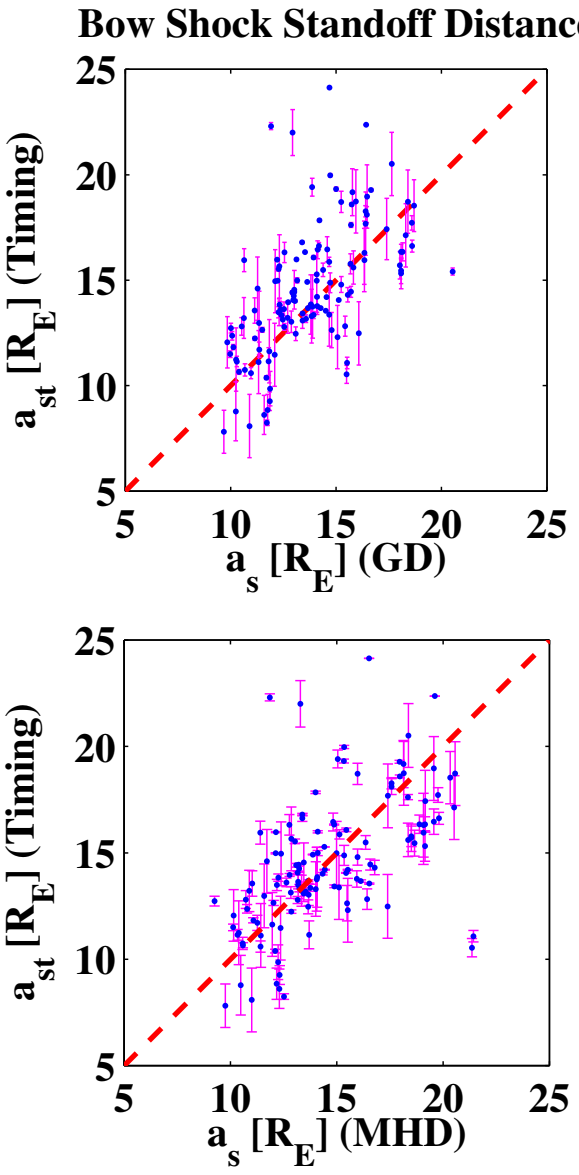

Figure 3.1: Timing standoff distance a_{st} versus standoff distance a_s obtained from a gas dynamics model (top panel) and a MHD model (bottom panel); errors are added to the plots. Each point corresponds to a bow shock crossing, and the slope of the dashed line is one.

the distribution is asymmetric about $\Delta = 0$, and the gas dynamics model underestimates the standoff distance, in a statistical sense, when compared to a_{st}. The analysis is further extended by averaging the difference Δ over

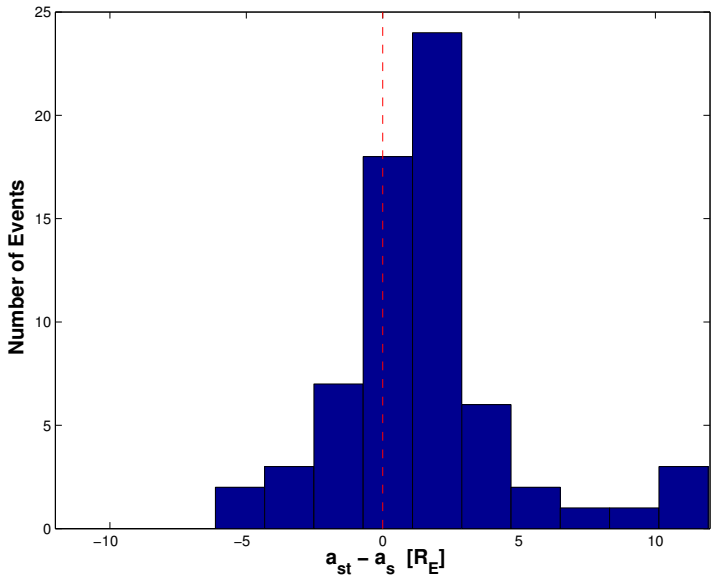

Figure 3.2: $\Delta = a_{st} - a_s$ histogram

successive intervals in $M_A = 0$ to 2, 2 to 4, 4 to 6 ... respectively. Figure 3.3 shows the results of $|a_{st} - a_s|$ versus M_A. The error bars associated with each numerical $|a_{st} - a_s|$ value correspond to one standard deviation. It is clear that, in a statistical sense, the agreement of a_s with a_{st}, as derived from the gas dynamic model 3.4 and the timing technique, is M_A dependent; the agreement is much better for high Mach number shocks. The bow shock standoff distance derived from the timing method exceeds on average the one derived from gas dynamic or MHD models. However, we have clearly found that the degree of agreement between models and observations is Mach

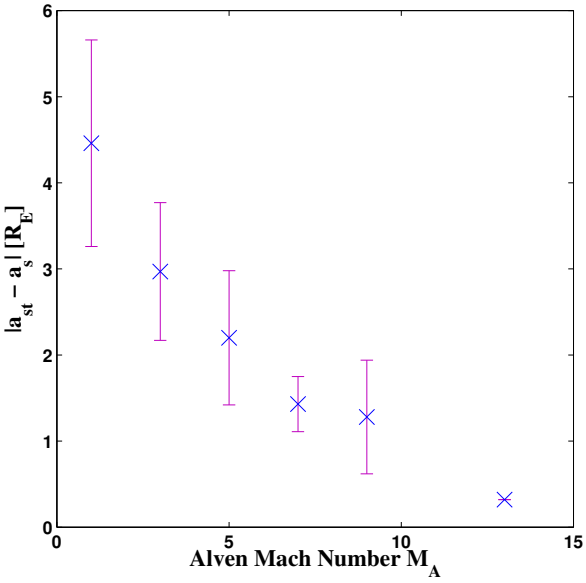

Figure 3.3: Absolute value of $\Delta = a_{st} - a_s$ versus M_A

number M_A dependent. The best agreement occurs for high M_A. While inside the range $M_A = 1 - 2$ the disagreement is quite significant ($4.5R_E$), it reduces to $0.6R_E$ for $M_A = 14$.

3.2 Shape

In section 2.1.2, we described the timing method which provides us the relevant elements that characterize the shock including the shock normal, its velocity and the angle (θ_{Bn}) between the upstream magnetic field and the normal to the shock surface. We examine in the present section, the shock's global shape as derived from the timing technique.

3.2.1 Comparison of Coplanarity and Timing Based Normal

The coplanarity theorem states that for a shock the upstream and downstream magnetic field vectors and the shock normal all lie in the same plane, and that the fields difference is also coplanar with the shock normal [19]. Based on this theorem, the shock normal n_c is given by:

$$\hat{n} = \frac{\left(\vec{B}_u - \vec{B}_d\right) \times \left(\vec{B}_u \times \vec{B}_d\right)}{\left|\left(\vec{B}_u - \vec{B}_d\right) \times \left(\vec{B}_u \times \vec{B}_d\right)\right|} \tag{3.13}$$

where $\vec{B}_u$ ($\vec{B}_d$) is the upstream (downstream) magnetic field. With single point measurements, the coplanarity is widely used in order to characterize the shock geometry. However, the results are often tainted with significant errors for large θ_{Bn} angles (nearly perpendicular shock). Moreover, observational evidence has indicated the existence of a non planer component of the magnetic field associated with shocks [63]. Using the coplanarity theorem, the shock orientation can be determined in terms of field measurements on both sides, upstream and downstream of the shock. The results are compared with the ones derived from the timing analysis using 4-point measurements. Because the timing derived shock normal uses four-point measurements, it provides a reliable test for the coplanarity hypothesis.

For the coplanarity normal determination purpose, the upstream and down-

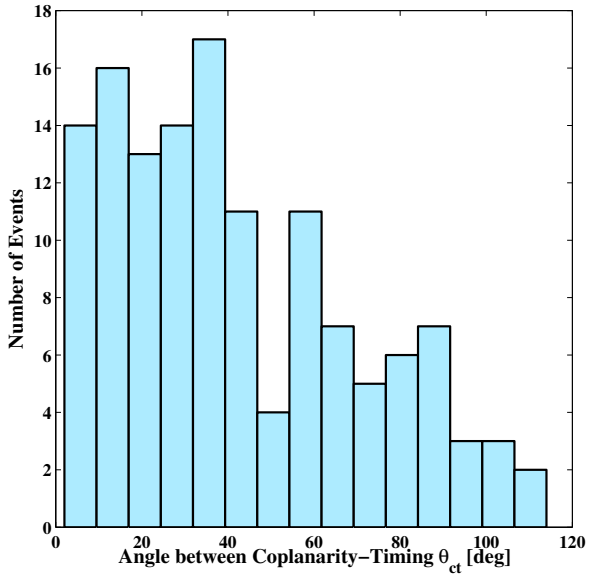

Figure 3.4: Histogram of angles between shock normal estimated by timing method and those calculated by coplanarity.

stream magnetic fields must be carefully identified to avoid the wave activity near the bow shock [7]. The main difficulty in implementing the coplanarity formula 3.13 using single-point measurement is that both the upstream and downstream fields are not simultaneously measured; there is an implicit assumption that the upstream field does not vary between the time when it is measured and the time when the downstream shock region is observed; the fields are likely to vary on both sides of the shock due to the presence of waves within and near the shock structures [42]. During the time periods before and after a shock crossing, and where the plasma is assumed to be in a steady state, the upstream and downstream fields $\vec{B}_u$ and $\vec{B}_d$ are obtained from an average. To illustrate the comparison between the two determinations of the

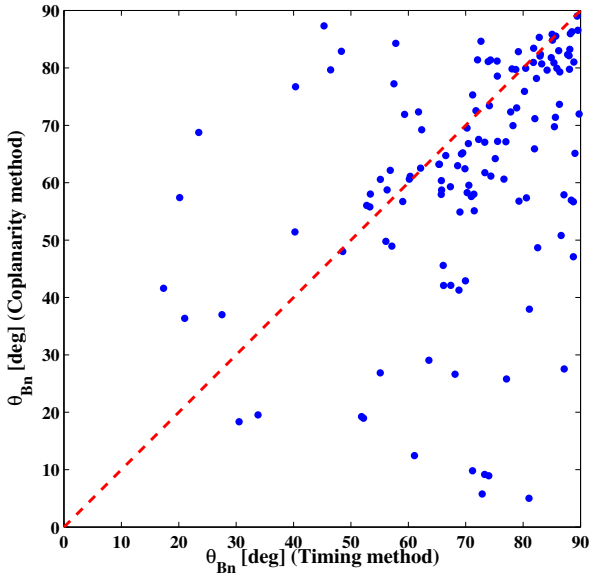

Figure 3.5: Comparison of θ_{Bn} obtained from coplanarity and those obtained from timing analysis.

shock normal, the distribution of the angular separation θ_{ct} between the two normals is plotted on Figure 3.4. The histogram indicates that the deviation from the timing normal is significant for quite a large number of events; only 15 events of the 133 events show deviations less than 10°. In an attempt to explain this discrepancy, in a study carried out by Horbury et al. [7], the authors found a good correlation between θ_{Bn} angle and θ_{ct}. With a data set of 48 shock crossings, the authors also found that the coplanarity could be a very poor estimator when $\theta_{Bn} > 80°$. With a larger statistics, we calculate the angle θ_{Bn} using both the timing and the coplanarity normals. Both determinations are reported on Figure 3.5. Our results somehow contrast with those found by [7], the correlation with the two θ_{Bn} determinations is not

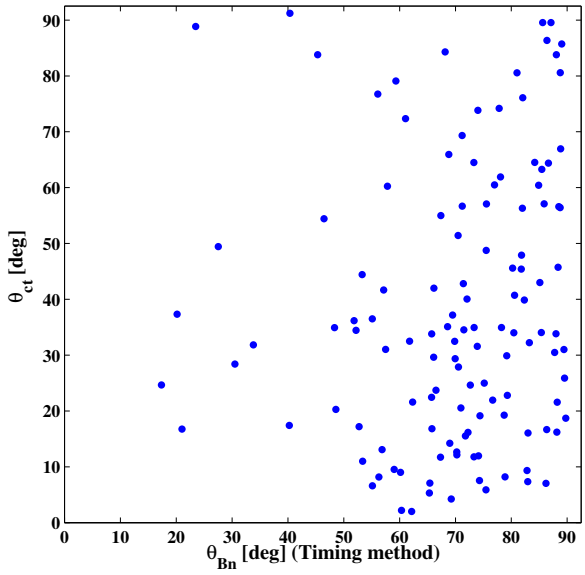

Figure 3.6: Angle θ_{ct} between the coplanarity and timing normals as a function of timing θ_{Bn}.

obvious. However, it appears in a statistical sense on Figure 3.6, the angle θ_{ct} is larger for higher θ_{Bn} numerical values, which is consistent with [7] findings. Pursuing the investigation of the difference between the timing and the coplanarity normals, an earlier study reported by Russell et al. [42] suggested that the deviation from coplanarity is related to the angle between the upstream and the downstream field directions. More precisely, if the angle between the fields is more than 10°, the deviation between the two normals is about 5°. In other words, the coplanarity provides a reliable estimation of the shock normal if the angle between the upstream and downstream directions is large. Although this latter study was based on four-point measurements, including ISEE 1, 2, 3 and IMP8, the separation between the spacecrafts involved was

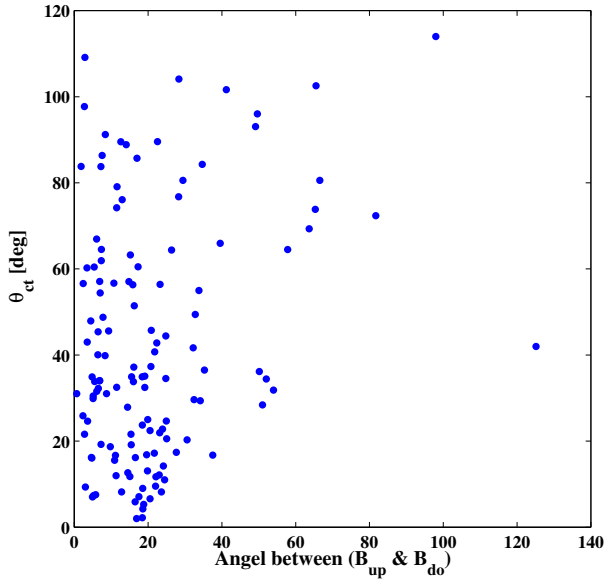

Figure 3.7: Deviation of coplanarity normal from timing normal as a function of the angle between the upstream and downstream magnetic fields directions.

quite large (several $R_E s$), which certainly invalidate the timing technique applied.

Based on Figure 3.7, it seems that there is no correlation and or causal relationship between the angle between the upstream and the downstream fields and the coplanarity shock normal. For angles less than 20°, the coplanarity data scatter over a rather large range in θ_{ct}.

3.2.2 Comparison of Conics Models and Timing Normals

The results of the timing analysis compared with the bow shock statistical models are examined in this section. The sole purpose of this exercise is to investigate how models of the bow shock shape depart from the direct measurement of the shock normal vector. The widely-used based conic sections including an elliptical model [47], paraboloid model [30] and hyperboloid model [49] are considered. A relatively recent and general 2-D surface model from [32] is also used. Again, the normal derived from previous models is compared with the timing normal. To determine the normal based-model $\hat{\mathbf{n}}_{\mathbf{M}}$, we assume that, for each crossing, the bow shock is near an equilibrium state, and ideally represented by a geometric surface which coincides with the crossing point. To determine $\hat{\mathbf{n}}_{\mathbf{M}}$, the model parameters must be known. To this end, it is assumed that all parameters are ram-pressure dependent, which is implicit for the conics model mentioned above. Below we solve for the paraboloid case used as an example; the treatment for the remaining three models is presented in Appendix D. A paraboloid of revolution is given by the following equation:

$$x + b_s\left(y^2 + z^2\right) - a_s = 0 \tag{3.14}$$

where a_s and b_s are the distance to the nose and the flaring parameter, respectively. The ram-pressure dependence is expressed such: $a_s = f a_{s0}$

and $b_s = f b_{s0}$, where $f = (\frac{p_0}{p})^{1/6}$. In the expression of f, p is the actual ram pressure at the time of the crossing and p_0 a nominal value for the ram pressure depending upon the model. For a paraboloid model, $p_0 = 2.1$ nPa [30]. Also it is widely accepted that for a nominal value of the ram pressure, $a_{s0} = 13.7\ R_E$ and $b_{s0} = 0.0223\ R_E^{-1}$. Usually, the ram pressure at the time of the crossing is not known; posing that the crossing location satisfies the paraboloid model, f can be solved for by rearranging 3.14:

$$a_{so} f^2 - x f - b_{so}\left(y^2 + z^2\right) = 0 \tag{3.15}$$

where (x, y, z) are the coordinates of the satellite at the crossing location. Solving for f we found:

$$f = \frac{1}{2a_{so}}\left[x + \sqrt{x^2 + 4a_{so}b_{so}\left(y^2 + z^2\right)}\right] \tag{3.16}$$

The solution f completely defines the model and therefore allows for the shock normal calculation according to Equation 3.5. A similar method is used to find the shock normal based with the hyperboloid, ellipsoid and Merka's models (see Appendix C), respectively. From the determinations above, the angle between n_M and n_t, measuring the deviation between the normals, is plotted for different models in Figures 3.8, 3.9, 3.10 and 3.11. The Figures clearly indicate that the results are similar, and are model independent in a statistical sense. We have found that for about half the crossings, the timing shock normals agree, within 11°.

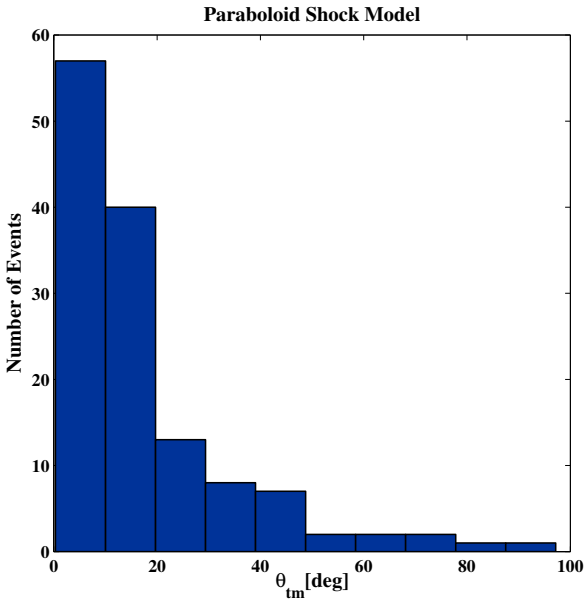

Figure 3.8: Histogram of the angle between the timing normal $\hat{\mathbf{n}}_\mathbf{t}$ and the paraboloid shock normal $\hat{\mathbf{n}}_\mathbf{m}$.

For a thorough discussion of the results reported in this chapter see the conclusion and discussion section of this thesis.

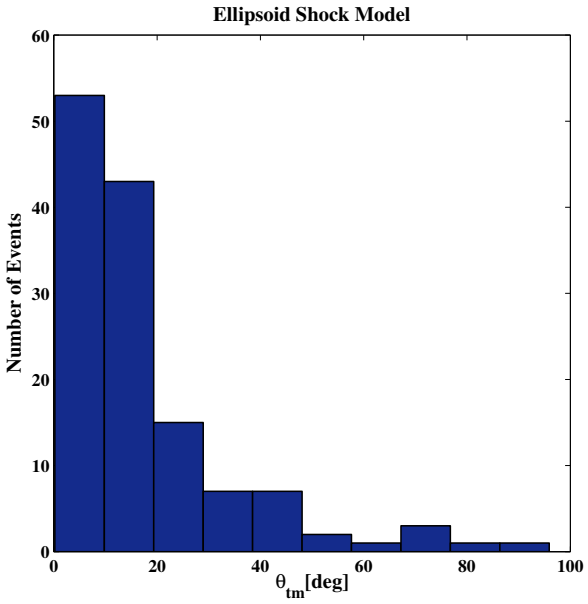

Figure 3.9: Histogram of the angle between the timing normal $\hat{\mathbf{n}}_\mathbf{t}$ and the ellipsoid shock normal $\hat{\mathbf{n}}_\mathbf{m}$.

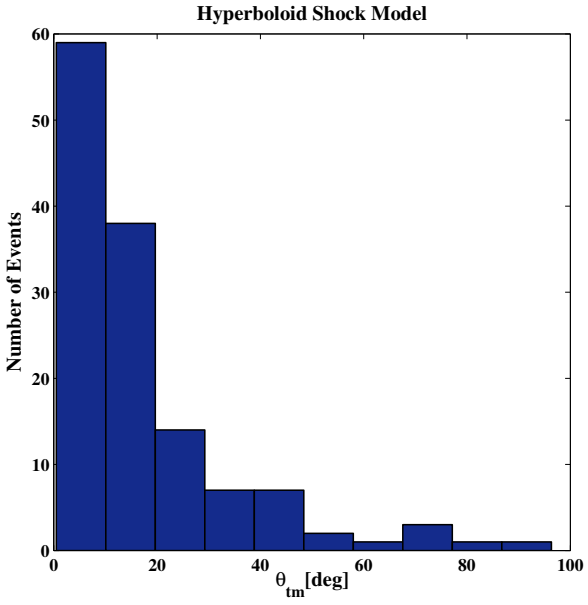

Figure 3.10: Histogram of the angle between the timing normal $\hat{\mathbf{n}}_\mathbf{t}$ and the hyperboloid shock normal $\hat{\mathbf{n}}_\mathbf{m}$.

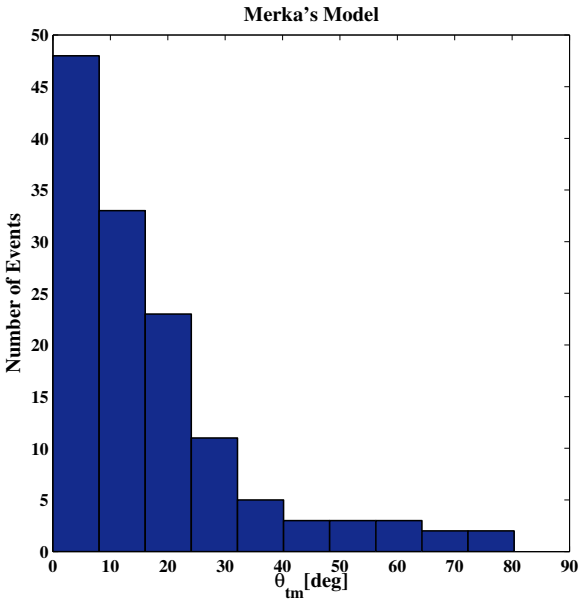

Figure 3.11: Histogram of the angle between the timing normal $\hat{\mathbf{n}}_\mathbf{t}$ and Merka's shock normal $\hat{\mathbf{n}}_\mathbf{m}$.

Chapter 4

Earth's Bow Shock Dynamics

In this chapter, the dynamics of the shock is investigated in the context of multi-spacecraft observations. We shall particularly focus on the shock velocity, and will present a detailed study. Prior to the European Cluster mission, shock motion measurements were performed using data collected by single or dual spacecrafts and analyzed while in some cases taking into account the Rankine-Hugoniot (RH) equations and ignoring them in others [38, 60, 53]. Cluster quartet measurements of the Earth's bow shock crossings allowed to estimate the nature and velocity of the bow shock motion in full three dimensional space.

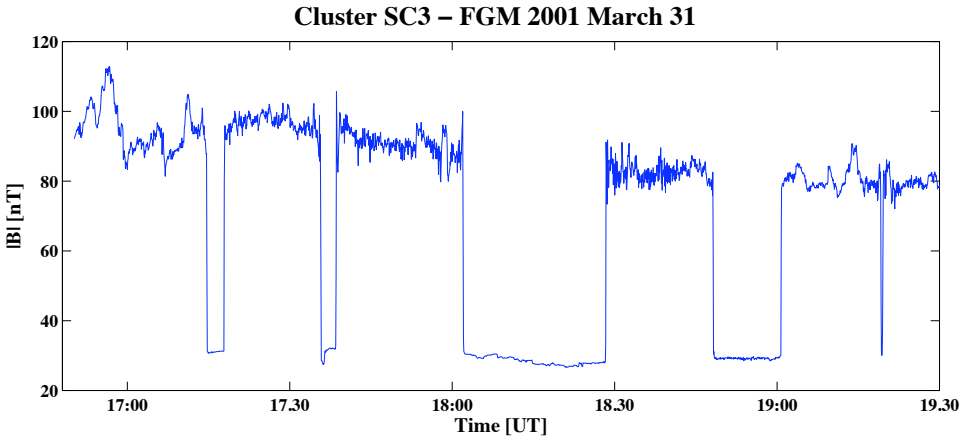

Figure 4.1: Successive shock crossings.

4.1 Statistical Results

Shock motion results essentially from various disturbances that occur in the solar wind conditions. This motion is often observed through successive shock crossings occurring during short time intervals lasting typically from few minutes to several hours. Cluster satellites "move back and forth" between the magnetosheath (downstream) and the solar wind (upstream), which indicate that the shock velocity is much higher than the satellite velocity, which is usually estimated to be of the order of ~ 2 km/s. An illustration of successive shock crossings is shown in Figure 4.1. In this Figure, several crossings through Cluster SC-3 occurred on March 31, 2001, characterized by a high solar wind variability. In this chapter, we investigate the shock dynamics by using the timing analysis introduced and described in section (2.1.2). The direction of the shock motion constitutes an important feature of interest

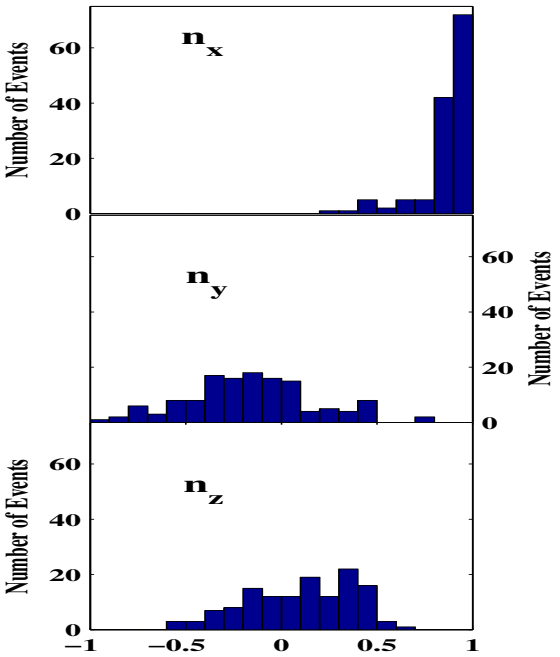

Figure 4.2: Histogram for the direction of shock motion along the 3 cartesian coordinates.

in shock dynamics, which is directly derived from the timing analysis. Figure 4.2 shows the histogram for the measured shock normal GPE-components n_x, n_y and n_z. The distribution clearly indicates shock motion along the x-GPE axis strongly suggesting that the shock motion is primarily directed along the Sun-Earth direction; the measurements indicate that 89% of the shock crossings with a $n_x/\sqrt{\left(n_y^2 + n_z^2\right)}$ ratio larger than 1. The shock velocity distribution for 133 crossings is shown on Figure 4.3. Positive (negative) velocity corresponds to outward (inward) moving shocks. The outward (inward) average speed is of the order of 49 km/s (57 km/s), although a quite large number of shocks (26 exactly) are observed with speed larger than 85

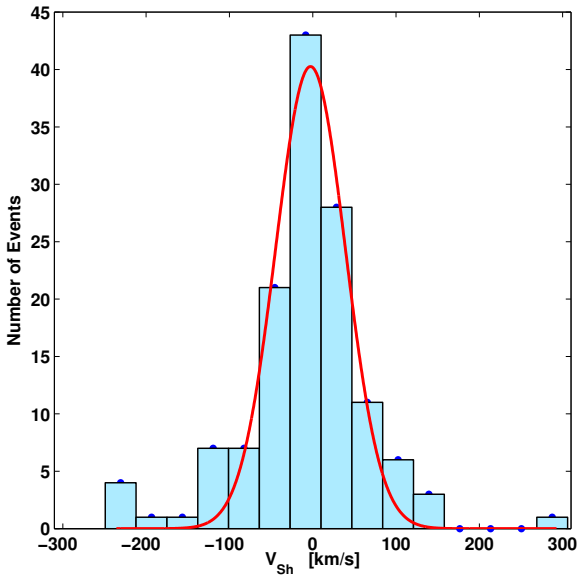

Figure 4.3: Shock velocity distribution.

km/s. The shock velocity distribution is very similar to the one obtained by Horbury et al. [7] and studies based on dual spacecraft (Russell et al. [43]; Šafránková et al. [56]). On the other hand, and as opposed to the results reported by Horbury et al. [7], we have not found any indication that the direction of the shock motion tends to be related to the shock geometry (θ_{Bn}). The red continuous curve on Figure 4.3 represents the best Gaussian fit of the shock velocity distribution. The fit provided a mean of ~ -2 km/s and a standard deviation equal to 42 km/s. We should mention that the Cluster orbital speed has been taken into account in the determination of the velocity distribution. Clearly, the fit is quite satisfactory for low shock speeds; departure from the Gaussian fit occurs at the speed of ~ 80 km/s (2 standard deviations). The Gaussian fit to the data could be interpreted as a shock

motion resulting from the random fluctuations in the solar wind conditions. This strongly suggests that the shock always move inward and outward under randomly fluctuating solar wind conditions. In their theoretical investigation, Völk and Auer [**?**] have shown that propagating Alvèn waves interacting with the shock induce shock speeds of the order of 10 km/s or less on average, which is strongly consistent with our results. However, for low Mach number shocks, the theoretical model predicts a much larger average shock speed. The systematic inward-outward motion could be intuitively interpreted as a recovery mechanism of a previously established shock in a quasi-static equilibrium configuration. The systematic inward/outward shock motion reflects an important coupling between the magnetopause and the shock through MHD waves. Moreover, in their theoretical study, Völk and Auer [**?**] have predicted that shock speeds larger than 85 km/s are caused by solar wind discontinuities, while smaller velocities result from interplanetary perturbations such as Alfvèn waves. Intuitively, we may presume that high shock speeds ($\gtrsim$ 85 km/s) are associated with significant abrupt changes in solar wind parameters. High shock-speed events are studied in section 4.3. In the next section, a simple model to account for the shock velocity distribution function is presented.

4.2 A Simple Model for the Shock Velocity Distribution Function

In this section we will develop the necessary tools to construct the probability distribution functions (PDFs) for the shock velocity near the nose region. As a starting point, we derive the probability distribution of the product of two random variables with Gaussian distribution functions.

4.2.1 The Probability Distribution Function of $P_z(z)$, $z = xy$

Let us consider two random variables x and y with Gaussian distributions given by:

$$\begin{aligned} P_x(x) &= \frac{1}{\sqrt{2\pi}\sigma_x} \exp\left\{-\frac{x^2}{2\sigma_x^2}\right\} \\ P_y(y) &= \frac{1}{\sqrt{2\pi}\sigma_y} \exp\left\{-\frac{y^2}{2\sigma_y^2}\right\} \end{aligned} \tag{4.1}$$

We construct the probability distribution function of the product $z = xy$ and show that the distribution is not normal; it is given by:

$$
\begin{aligned}
P_z(z) &= \frac{1}{2\pi\sigma_x\sigma_y}\int_{-\infty}^{+\infty}\int_{-\infty}^{+\infty}\exp\left\{-\frac{x^2}{2\sigma_x^2}\right\}\exp\left\{-\frac{y^2}{2\sigma_y^2}\right\}\delta(xy-z)dxdy \\
&= \frac{1}{2\pi\sigma_x\sigma_y}\int_{-\infty}^{+\infty}\int_{-\infty}^{+\infty}\exp\left\{-\frac{x^2}{2\sigma_x^2}\right\}\exp\left\{-\frac{y^2}{2\sigma_y^2}\right\}\frac{1}{|y|}\delta\left(x-\frac{z}{y}\right)dxdy \\
&= \frac{1}{2\pi\sigma_x\sigma_y}\int_{-\infty}^{+\infty}\frac{dy}{|y|}\exp\left\{-\frac{1}{2\sigma_x^2}\left(\frac{z}{y}\right)^2-\left(\frac{y^2}{2\sigma_y^2}\right)\right\} \qquad (4.2)
\end{aligned}
$$

We now perform the following change of variables. We first change $y \to -y$, then we call

$$Y = \frac{y}{\sigma_y} \qquad \text{and} \quad Z = \frac{|z|}{\sigma_x\sigma_y}$$

this in turn leads to the following PDF

$$P_z(Z) = \frac{1}{\pi\sigma_x\sigma_y}\int_0^{+\infty}\frac{dY}{Y}\exp\left\{-\frac{1}{2}\left[\frac{Z^2}{Y^2}+Y^2\right]\right\} \qquad (4.3)$$

We proceed and make a new change of variable:

$$Y = \sqrt{Z}t$$

which now leads to the following PDF:

$$P_z(Z) = \frac{1}{\pi\sigma_x\sigma_y}\int_0^{+\infty}\frac{dt}{t}\exp\left\{-\frac{Z}{2}\left[\frac{1}{t^2}+t^2\right]\right\} \qquad (4.4)$$

We again make the following change of variable:

$$t = e^u$$

which in turn leads to the following Probability Distribution Function for the product $z = xy$.

$$P_{z=xy}(Z) = \frac{2}{\pi\sigma_x\sigma_y}\int_0^{+\infty} du \exp\{-Z\cosh 2u\} \tag{4.5}$$

Finally introducing the variable:

$$t = \cosh 2u$$

leads to the known integral form:

$$\begin{aligned} P_{z=xy}(Z) &= \frac{1}{\pi\sigma_x\sigma_y}\int_1^{+\infty}\frac{dt}{\sqrt{t^2-1}}\exp\{-Zt\} \\ &= \frac{1}{\pi\sigma_x\sigma_y}K_0(|Z|) \end{aligned} \tag{4.6}$$

The final answer is given by

$$P_{z=xy}(z) = \frac{1}{\pi\sigma_x\sigma_y}K_0\left(\frac{|z|}{\sigma_x\sigma_y}\right) \tag{4.7}$$

where $K_0(x)$ is the Modified Bessel function of order zero. It is clear from this result that the product of two normally distributed Gaussian random

variables is not normally distributed. The next step is to construct the distribution function for a variable y given by $y = f(x)$ and where x is a Gaussian random variable. For this purpose, we consider a transformation method. Let $y = f(x)$, where f is a known function, and x a Gaussian random variable. We suppose that the probability density of x is $P_x(x)$. What is then the probability density, $P_y(y)$, of y? In order to resolve the problem, we consider the basic rule of probability conservation:

$$|P_x(x)dx| = |P_y(y)dy| \tag{4.8}$$

In other words, the probability of finding x in the interval x to $x + dx$ is the same as the probability of finding y in the interval y to $y + dy$. It then follows that

$$P_y(y) = \frac{P_x(x)}{|f'(x)|} \tag{4.9}$$

where $f'(x) = \frac{df}{dx}$.

We will now apply these results to the case of the velocity of the shock near the nose region under certain assumptions to be explicitly exposed.

4.2.2 Probability Density for the Velocity of the Bow Shock Near the Nose Region

In this section we will use the empirical expression for the standoff position that Spreiter et al. [23] derived in the context of gas dynamics, and which was used by Meziane et al. [35]. The expression is given by:

$$R = 9.47 \left(\frac{2f^2/k}{p} \right)^{\frac{1}{6}} (1 + 1.1\rho) \tag{4.10}$$

where the ram pressure p is expressed in nPa, the parameters f and k reflect the effective portion of the solar wind dynamical pressure as applied to the magnetosphere and the effects of the electric currents in the magnetopause, respectively, and where ρ represents the ratio of the upstream plasma density to the downstream plasma density. For all purposes, we will rewrite this expression in the following form:

$$\begin{aligned} R &= 9.47 \left(\frac{2f^2}{k} \right)^{\frac{1}{6}} (1 + 1.1\rho) \times p^{-1/6} = x(\rho) \times g(p) \\ x(\rho) &= 9.47 \left(\frac{2f^2}{k} \right)^{\frac{1}{6}} (1 + 1.1\rho) = b + a\rho \\ g(p) &= p^{-1/6} = y \end{aligned} \tag{4.11}$$

where

$$\begin{aligned} b &= 9.47\left(\frac{2f^2}{k}\right)^{\frac{1}{6}} \\ a &= 1.1b = 10.42\left(\frac{2f^2}{k}\right)^{\frac{1}{6}} \end{aligned} \tag{4.12}$$

The velocity of the Bow Shock nose can be evaluated by taking the time derivative of expression (4.10). For now, we make the fundamental assumption that the shock compressional ratio ρ is time independent under any change of the the ram pressure. Time variations in ram pressure reflect various propagating solar wind plasma fluctuations, which in turn affect the downstream plasma. Therefore, self-consistency requires the inclusion of the $\dot{\rho} = \frac{d\rho}{dt}$ term, which renders the calculation less tractable. For now and as a first attempt, we assume that the term is small. Taking the time derivative of (4.10), we obtain:

$$\begin{aligned} V &= \frac{dR}{dt} \\ &= -1.58\left(\frac{2f^2}{k}\right)^{\frac{1}{6}}(1+1.1\rho)p^{-7/6} \times \dot{p} = h(p) \times \dot{p} \\ \text{with} \quad h(p) &= -1.58\left(\frac{2f^2}{k}\right)^{\frac{1}{6}}(1+1.1\rho)p^{-7/6} = -Ap^{-7/6} \\ \text{and} \quad h'(p) &= \frac{dh}{dp} \\ &= \frac{7A}{6}p^{-13/6} \end{aligned} \tag{4.13}$$

We make the following change of variable

$$z = -Ap^{-7/6} \tag{4.14}$$

This form allows calculation of the probability density $P_z(z)$ in terms of $P_p(p)$ and consequently $P_V(V)$. Notice that $z < 0$. At this point, the probability distribution function for the ram pressure $P_p(p)$ should be provided. As a first approximation we assume that the ram pressure p is a Gaussian random variable with a distribution given by:

$$P_p(p) \;=\; \frac{1}{\sqrt{2\pi}\sigma_p} \exp\left\{-\frac{(p-p_0)^2}{2\sigma_p^2}\right\} \tag{4.15}$$

The choice of distribution 4.15 is dictated by the random fluctuations in the plasma density and velocity. Intuitively, we expect that the observed ram PDF is close to a Maxwellian particularly near the maximum. An accurate representation of the ram pressure PDF should certainly include plasma discontinuities and other transient events, which induce sharp changes in the solar wind parameters. Solving for the shock velocity distribution also requires $P_{\dot{p}}(\dot{p})$ to be known. With similar arguments raised above, the choice of a Maxwellian shape for $P_{\dot{p}}(\dot{p})$ is justified; in this case however, the nominal numerical value $\dot{p_0} = 0$. Therefore

$$P_{\dot{p}}(\dot{p}) = \frac{1}{\sqrt{2\pi}\sigma_{\dot{p}}} \exp\left\{-\frac{\dot{p}^2}{2\sigma_{\dot{p}}^2}\right\} \tag{4.16}$$

We know from earlier results (see above), and after expressing p in terms of z ($p = (-A/z)^{6/7}$), that:

$$\begin{aligned} P_z(z) &= \frac{P_p(p)}{|h'(p)|} = \frac{6}{7A\sqrt{2\pi}\sigma_p} p^{13/6} \exp\{-\frac{(p-p_0)^2}{2\sigma_p^2}\} \\ &= \frac{6}{7A\sqrt{2\pi}\sigma_p} \left(-\frac{A}{z}\right)^{\frac{13}{7}} \exp\left\{-\frac{1}{2\sigma_p^2}\left(\left(-\frac{A}{z}\right)^{6/7} - p_0\right)^2\right\} \end{aligned} \quad (4.17)$$

The next step is to construct the probability density for the velocity of the nose of the shock, which is written as $V = z\dot{p}$, which we consider as the product of two random variables

$$\begin{aligned} P_V(V) &= \int_{-\infty}^{+\infty} d\dot{p} \int_{-\infty}^{0} dz \delta(z\dot{p} - V) P_z(z) P_{\dot{p}}(\dot{p}) \\ &= \int_{-\infty}^{+\infty} d\dot{p} \int_{0}^{+\infty} \frac{dz}{|\dot{p}|} \delta(z + \frac{V}{\dot{p}}) P_z(-z) P_{\dot{p}}(\dot{p}) = \int_{-\infty}^{0} \frac{d\dot{p}}{|\dot{p}|} P_{\dot{p}}(\dot{p}) P_z\left(\frac{V}{\dot{p}}\right) \\ &= \int_{0}^{+\infty} \frac{d\dot{p}}{\dot{p}} P_{\dot{p}}(\dot{p}) P_z\left(-\frac{V}{\dot{p}}\right) \end{aligned} \quad (4.18)$$

which finally leads to:

$$P_V(V) = \frac{3}{7\pi A \sigma_p \sigma_{\dot{p}}} \left(\frac{A}{V}\right)^{13/7} \int_0^{+\infty} d\dot{p} \dot{p}^{6/7} \exp\left\{-\frac{\dot{p}^2}{2\sigma_{\dot{p}}^2}\right\} \exp\left\{-\frac{1}{2\sigma_p^2}\left(\left(\frac{A}{V}\dot{p}\right)^{6/7} - p_0\right)^2\right\} \quad (4.19)$$

This integral is evaluated numerically given that the probability densities $P_p(p)$ and $P_{\dot{p}}(\dot{p})$ are provided. These probabilities are obtained experimentally from spacecraft observations of solar wind.

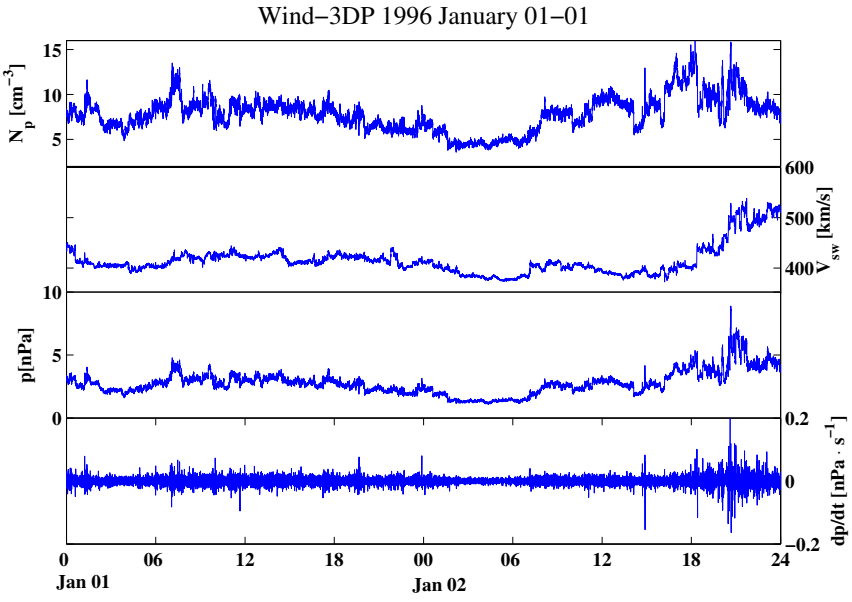

Figure 4.4: Solar plasma data time series measured by WIND-3DP experiment on 1996, January 01-02. The two top panels show the ion density and flow velocity, respectively. The third panel shows the solar wind ram pressure in nPa unit, while the bottom panel displays the time variation of the ram pressure (in nPa/s) at WIND location. The time resolution for the measurements is 12 sec.

A representative example of the solar wind plasma data is illustrated on Figure 4.4 which shows the ion density and the flow velocity measurements on January 01-02 , 1996, performed by WIND-3DP experiment; the WIND spacecraft was located at 91 R_E from Earth. With one plasma measurement every 12 sec, the average over the whole period of solar wind parameters are typical: a density $N_{sw} = 7.8\ cm^{-3}$, a flow $V_{sw} = 420$ km/s and an ion temperature $T_{sw} = 11$ eV. The Figure shows small to moderate amplitude

fluctuations in the plasma physical properties characterizing a quasi-typical conditions for the solar wind. The ram pressure p as well as its time variation $\dot{p}$ at WIND location are calculated and plotted on the third and the bottom panels of Figure 4.4, respectively. The complete time series shown in Figure 4.4 is composed of 7200 measurements, a sufficiently large data set to build a probability distribution for the ram pressure under quiet solar wind conditions.

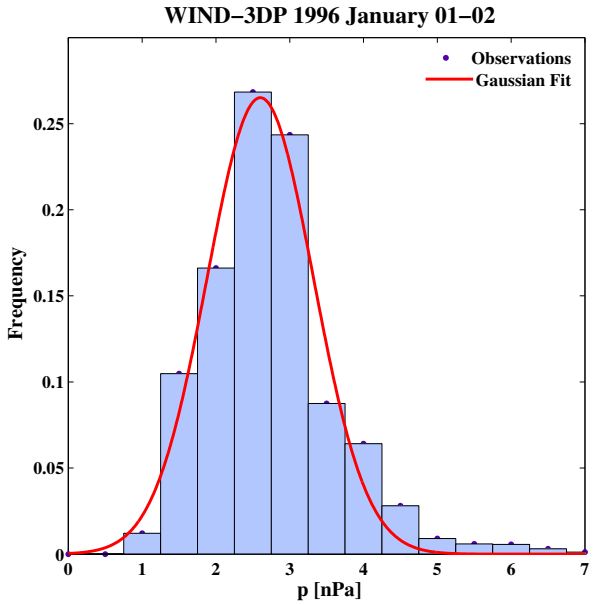

Figure 4.5: Solar wind ram pressure distribution.

Figures 4.5 and 4.6 show the distributions $P_p(p)$ and $P_{\dot{p}}(\dot{p})$ for the solar wind ions corresponding to the time series of Figure 4.4. The red continuous line on each figure represents the best Gaussian fit of the observation (Histogram). It is clear that the Gaussian fit is quite satisfactory for $P_{\dot{p}}(\dot{p})$ distribution

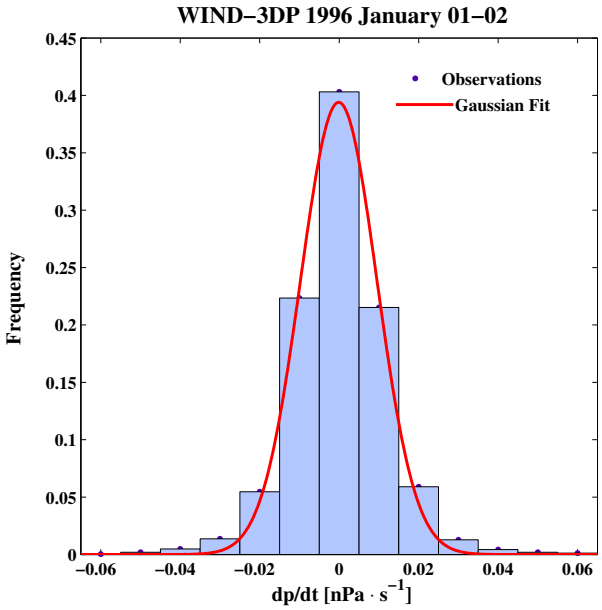

Figure 4.6: Solar wind dp/dt distribution.

with $P_{\dot{p}}(\dot{p}) = 0.39e^{-(\dot{p}/\sqrt{2}\sigma_{\dot{p}})^2}$ and a standard deviation $\sigma_{\dot{p}} \sim 0.01$ nPa/s. For the ram pressure distribution $P_p(p)$, the Gaussian fit is less satisfactory, and a tail corresponding to high ram pressure values is present and noticeable; this is expected when the solar wind density and the velocity fluctuations are random. The Gaussian fit is given by $P_p(p) = 0.26e^{-((p-p_0)/\sqrt{2}\sigma_p)^2}$ with a mean of $p_0 \sim 2.7$ nPa and standard deviation $\sigma_p \sim 0.72$ nPa. Finally to calculate the integral 4.19, the compressional ratio ρ should be provided. The latter can be obtained from the resolution of the Rankine-Hugoniot equations, given that plasma and magnetic data are available. To estimate ρ, we choose solar wind parameters averaged over the 1996 January 01-02 interval period and a typical value for $M_A \sim 10$. At the shock nose, we found

$\rho \sim 0.26$.

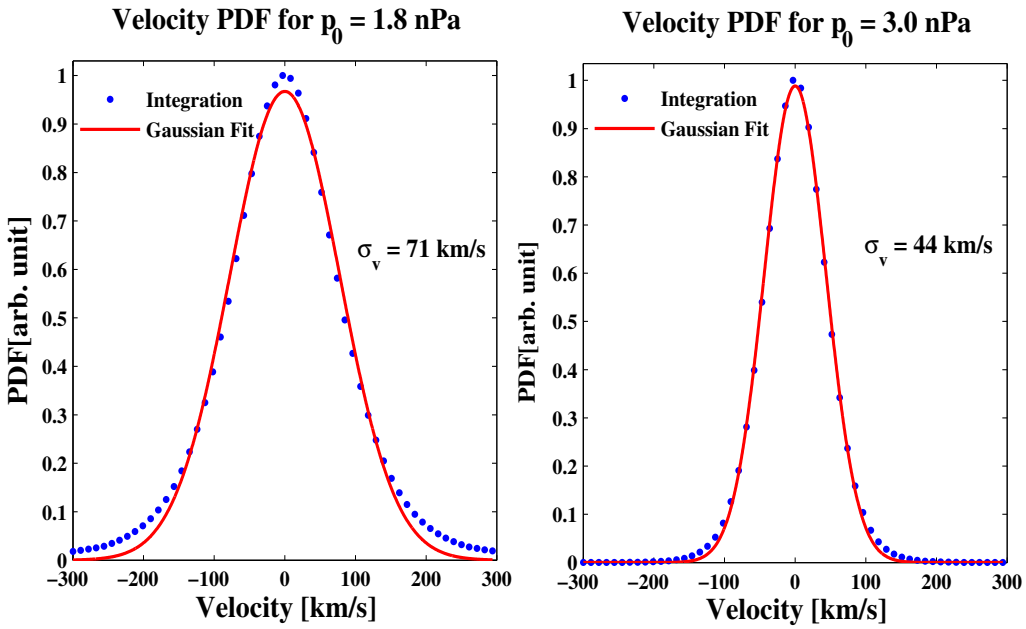

Figure 4.7: Results of the numerical integration of expression (4.19) for two values of p_0.

Figure 4.7 shows the predicted shock velocity probability density $P_V(V)$ obtained from the numerical integration of expression (4.19) for two numerical values of p_0: $p_0 = 1.8$ nPa (left panel) and $p_0 = 3.0$ nPa (right panel). The probability density $P_V(V)$ presents some interesting features that can be described as follows. First, the distributions are symmetric and appear nearly Gaussian, particularly near the maximum. Also, it results from the calculation of $P_V(V)$ that the average shock speed is nearly zero for any numerical value of p_0 and that the distribution width near the maximum increases with

decreasing p_0. A Gaussian best fit to the small velocities (near the peak) provides a standard deviation $\sigma_V = 71$ km/s for $p_0 = 1.8$ nPA and $\sigma_V = 44$ km/s for $p_0 = 3.0$ nPA.

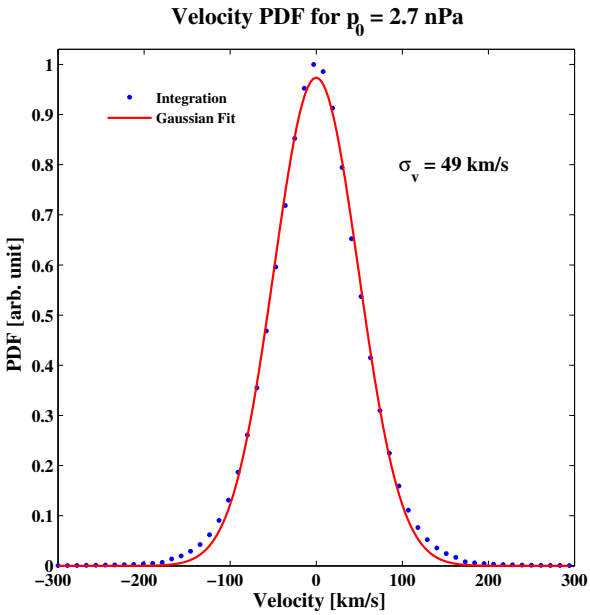

Figure 4.8: Velocity PDF calculated from expression (4.19); the free parameters are obtained from the average of the plasma data measurements by WIND on 1996 January 01-02.

If we use the distributions $P_p(p)$ and $P_{\dot{p}}(\dot{p})$ of Figures 4.5 and 4.6 from the January 01-02, 1996 plasma data to calculate $P_V(V)$, we obtain the results shown on Figure 4.8. In this particular case, the Gaussian best fit provides a standard deviation $\sigma_V = 49$ km/s in very good agreement with the observed shock velocity distribution reported above in section 4.3. These results strongly indicate that considerations about the ram pressure satisfactorily account for the observed shock bulk speed, i.e. the Mach number

M_A is not relevant. The Alfven Solar wind turbulence constitutes the main driver of the random character of the shock motion.

4.3 The Case of High Speed Shocks

We present below a detailed investigation of high-speed shock events. Since we used ACE data to monitor the solar plasma, only events where ACE data were available were considered, i.e 16 out of 26 events. An example of high

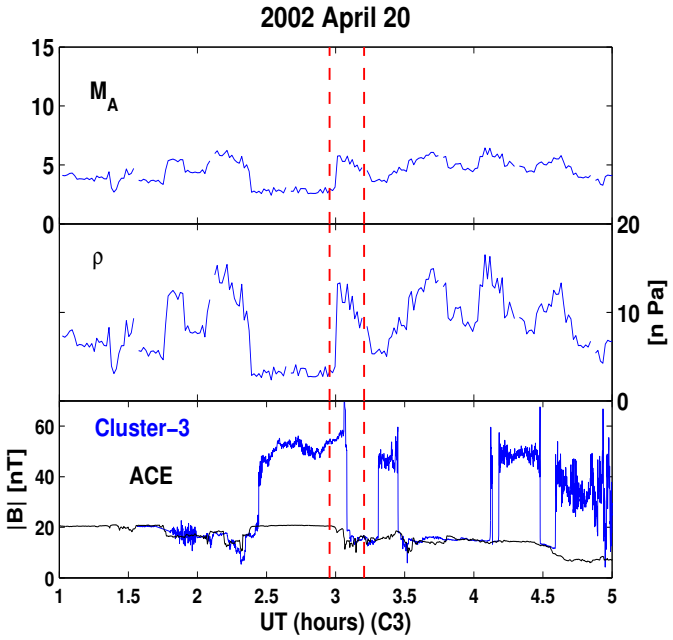

Figure 4.9: Bottom panel shows magnetic field magnitude from Cluster-3 and ACE spacecraft on April 20, 2002. Data from ACE are shifted by 42.4 minutes. The middle and top panels show measurements from ACE of ram pressure ρ and Alfvèn and Mach number M_A as derived from the solar wind and magnetic field data, respectively. The two dashed vertical lines in both panels indicate a 12 minute window centred on the shock crossing we have analyzed.

speed shock crossing is illustrated in Figure 4.9. The timing analysis of the shock crossing which occurred at 0347:18 UT at Cluster-3 provided an inward shock speed of $\sim$ 219 km/s, and a shock normal $\mathbf{n_t}$ = (0.939, -0.277, -0.200). To characterize the plasma environment at the shock time, we used ACE to monitor the solar wind conditions. We found, using visual inspection, a convective time delay from ACE to Cluster-3 of the order of 42.4 minutes, which provides a satisfactory overlap of magnetic field measurements recorded by the two spacecrafts as shown on the top panel of Figure 4.9. A rough estimate of the time delay, based on the ACE-Cluster distance, provides a numerical value of 39 minutes. On the same Figure, the two vertical dashed lines delimit a 12 minute time-interval centred on the shock crossing time.Our choice of 12 minutes is dictated by the fact that a longer time interval leads to a noticeable change in the overlap of the magnetic field measurement time series between ACE and Cluster. In fact, it corresponds to an uncertainty of the convective time delay from ACE to Cluster spacecraft, which has been discussed in the example reported in section 2.3. It is clear from Figure 4.9 that the Cluster shock inward motion at 0347:18 UT may be related to a compression due to an abrupt increase in the solar wind ram pressure ρ with no less sharp but moderate increase of Mach number M_A. It is worth noting that the 0347:18 UT shock crossing coincides with the sharp changes in the solar wind conditions for a time delay of 47 min. Taking into account the response of the shock, the time delay found here is certainly reliable. Our next step is to predict the shock speed resulting from the observed abrupt

change in ρ and M_A. For this purpose, we differentiate with respect to time the standoff distance formula 3.6 introduced earlier to obtain an expression for the shock speed: we start by rewriting equation 3.6 as following

$$a_s = C\frac{1}{\rho^{1/6}}\left[1+\frac{1.1}{\gamma+1}\frac{(\gamma-1)\,M_A^2+2}{M_A^2-1}\right] \tag{4.20}$$

where $C = 9.47\,(2f^2/k)^{1/6}$ and by using

$$\frac{da_s}{dt} = \frac{\partial a_s}{\partial \rho}\frac{d\rho}{dt} + \frac{\partial a_s}{\partial M_A}\frac{dM_A}{dt} \tag{4.21}$$

$$\frac{\partial a_s}{\partial \rho} = -\frac{C}{6}\frac{1}{\rho^{7/6}}\left[1+\frac{1.1}{\gamma+1}\frac{(\gamma-1)\,M_A^2+2}{M_A^2-1}\right] \tag{4.22}$$

$$\frac{\partial a_s}{\partial \rho} = -\frac{1}{6\rho}\frac{C}{\rho^{1/6}}\left[1+\frac{1.1}{\gamma+1}\frac{(\gamma-1)\,M_A^2+2}{M_A^2-1}\right]$$

$$\frac{\partial a_s}{\partial \rho} = -\frac{a_s}{6\rho} \tag{4.23}$$

$$\frac{\partial a_s}{\partial M_A} = \frac{C}{\rho^{1/6}}\frac{1.1}{\gamma+1}\left[\frac{2\,(\gamma-1)\,M_A\,(M_A^2-1)-2M_A\,(\gamma-1)\,M_A^2-4M_A}{(M_A^2-1)^2}\right] \tag{4.24}$$

$$= \frac{2.2C}{\gamma+1}\frac{1}{\rho^{1/6}\,(M_A^2-1)^2}\left[(\gamma-1)\,M_A\left(M_A^2-1-M_A^2\right)-2M_A\right]$$

$$= -\frac{2.2C}{\gamma+1}\frac{M_A}{\rho^{1/6}\,(M_A^2-1)^2}\,(\gamma+1)$$

$$= -2.2C\frac{MA}{\rho^{1/6}\,(M_A^2-1)^2}$$

$$= -2.2\frac{C}{\rho^{1/6}M_A}\left(\frac{M_A}{M_A^2-1}\right)^2 \tag{4.25}$$

use equation 4.23 and equation 4.25 in expression 4.21

$$\frac{da_s}{dt} = -\frac{a_s}{6\rho}\frac{d\rho}{dt} - 2.2\frac{C}{\rho^{1/6}M_A}\left(\frac{M_A}{M_A^2-1}\right)^2\frac{dM_A}{dt} \tag{4.26}$$

$$= -\frac{a_s}{6\rho}\frac{d\rho}{dt}\left[1 + \frac{6\rho}{a_s}\frac{2.2C}{\rho^{1/6}M_A}\left(\frac{M_A}{M_A^2-1}\right)^2\frac{dM_A/dt}{d\rho/dt}\right]$$

$$\frac{da_s}{dt} \approx -\frac{a_s}{6\rho}\frac{\Delta\rho}{\Delta t}\left[1 + \frac{13.2C}{a_s}\frac{\rho^{5/6}}{M_A}\left(\frac{M_A}{M_A^2-1}\right)^2\frac{\Delta M_A}{\Delta\rho}\right] \tag{4.27}$$

Equation 4.27 provides the theoretical predictions of the shock velocity at the nose for given perturbations $\frac{\Delta\rho}{\Delta t}$ and ΔM_A. $\Delta\rho$ could be significant for propagating discontinuities which are quite common in the solar wind. It has been suggested that the interaction of tangential discontinuities with the shock may result in quite high speed shock motion [39, **?**].The observed shock velocity is plotted versus the maximal numerical/algebraic value of $\Delta\rho$ within the 12 min window. The observed shock velocity versus $\Delta\rho$ for the 16 events is shown in Figure 4.10. On the x-axis, $\Delta\rho$ corresponds to the maximum algebraic numerical value of the ram pressure within the 12-minutes window. Except for 3 events, the variation of the ram pressure is consistent with the direction of the shock motion: inward (outward) shock motion corresponds to an increase (decrease) of the solar wind ram pressure. Roughly, higher ram pressure variations correspond to high shock speeds. However, it is clear that the ram pressure variations alone do not account for the shock speed. At this point, a larger data set is necessary to pursue

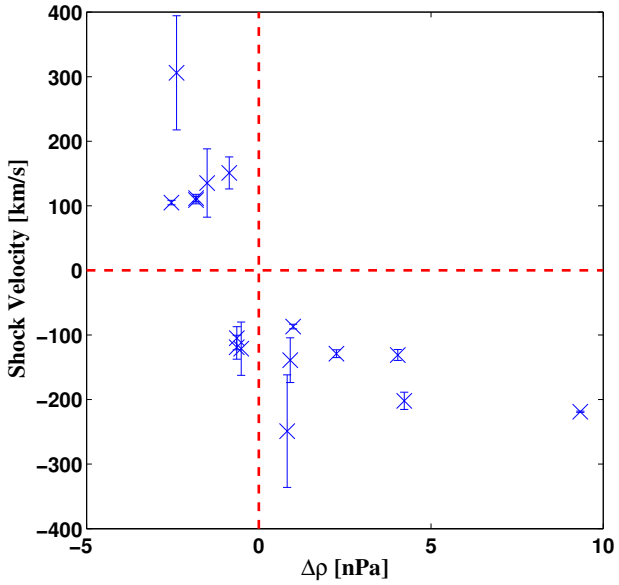

Figure 4.10: Observed shock velocity versus the variation of the ram pressure at ACE location. The convective time delay between ACE and Cluster is taken into account.

any theoretical investigation. An estimation of the prediction of the shock velocity could be obtained from Equation 4.27. For this purpose we determine the successive differences of ρ and M_A which allow for an estimate of the time derivative $\frac{\Delta\rho}{\Delta t}$ of the ram pressure; two successive measurements are separated by $\Delta t = 64$ sec. We then deduce the velocity of the shock nose da_s/dt for each of the twelve events of Figure 4.10. The results are plotted versus the measured radial component of the shock as shown on Figure 4.11. Despite the scattering of the data points about the line of slope unity; we carried out a linear regression and found a best linear fit given by $V_{sh} = 1.2\frac{da_s}{dt} - 58.1$ with a coefficient of correlation of 0.73. As a conclusion, we have shown that high speed shock motions are mainly accompanied with significant and sharp

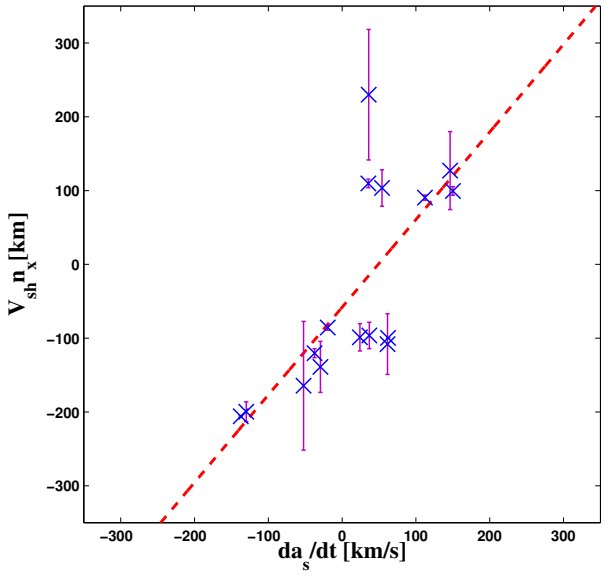

Figure 4.11: Observed shock velocity versus the model shock velocity predicted with Equation 4.27. The dashed line represents the best linear fit.

changes in solar wind ram pressure observed upstream. The changes are in most part consistent with the inward and outward motion. An attempt to compare the observed shock velocities with theoretical predictions based on a gas dynamics model have been carried out. Our estimate of the ram pressure temporal changes provides shock velocity values that are in good agreement with the observations. These results are in agreement with the theoretical predictions of Völk and Auer [**?**] seminal work. Tangential discontinuities are a major driver to shock motion with speeds larger than $\approx$ 80 km/s. For such cases, and when compared to the Mach number, we found that the the ram pressure variations are a dominant factor when fast shock motions occur.

Chapter 5

Conclusion and Discussion

We have investigated the location, shape and motion of Earth's bow shock using observations based on measurements made by the cluster spacecraft quartet. Several bow shock crossings have been identified and carefully characterized according to several relevant plasma parameters; a data collection of 133 Earth bow shock crossings, ranging from quasi-steady perpendicular to moderately noisy oblique geometries, have been identified and characterized using a timing method and the corresponding solar wind plasma conditions were identified. When present, the magnetic field fluctuations are suppressed using the appropriate technique such as a low band-pass ltering or moving averages before applying the timing method.

We compared the bow shock standoff distance derived from the timing method with those predicted by the Gas Dynamics and Magnetophydrodynamics bow

shock models. We found that the standard shock models statistically underestimate the standoff distance derived from the timing analysis. However we have clearly found that the degree of agreement between models and observations is Mach number M_A dependent. We found that the best agreement between models and observations occurs for high M_A. While inside the range $M_A = 1 - 2$, the disagreement is quite significant ($4.5R_E$); it reduces to ($0.6R_E$) for $M_A = 14$.

We have examined the shock global shape as derived from the timing technique by testing the coplanarity hypothesis and conics models. We have examined the calculated shock normal based on the coplanarity hypothesis and that obtained through the timing method and found that the distribution of the angular separation θ_{ct} between the two normals shows a deviation from the timing normal for quite a large number of events. We have calculated the angle θ_{Bn} using both the timing and the coplanarity normals, and our results show no obvious correlation with the two θ_{Bn} determinations. We found that, there is no indication of a possible impact of the angle between the upstream and downstream magnetic fields on coplanarity.

The comparison between the timing normal and the widely-used bow shock model provides limited outcomes. The angle between the timing normal and the conics based models indicates that the results are similar and are model independent in a statistical sense. For half of the studied crossings, the angle

between the two shock normals lie within 11^o. We have found no indication that departure from an ideal bow shock model is related to the crossing position along the x-axis. Therefore, the hypothesis that an expansion (or a compression) wave propagation from the nose to the flanks accompanying a shock motion is not supported by our analysis.

The shock dynamics direction has been determined directly from the timing analysis. The distribution of the shock normal for 133 crossings derived from timing clearly indicates that the shock motion is along the $x-$GPE axis, and consequently the shocks move globally inward (or outward) basically along the Sun-Earth direction. We have not found any indication that the direction of the shock motion tends to be related to the shock geometry (θ_{Bn}). The shock velocity distribution is satisfactorily fit by a zero-mean Maxwellian for speeds less than $\sim$ 80 km/s. This strongly suggests that the shock always move inward and outward under solar wind conditions which fluctuate randomly. Our results support the theoretical investigation given by Völk and Auer [58], who have shown that the propagation of Alvèn waves interacting with the shock induce shock speeds of the order of 10 km/s or less on average: in very good agreement with our results. However, for low Mach number shocks, the average shock speed could be much larger. The systematic inward-outward motion could be intuitively interpreted as a mechanism of recovery of a previously established shock in a quasi-static equilibrium configuration. The systematic inward/outward shock motion reflects an im-

portant magnetopause-shock coupling through MHD waves.

We constructed the probability distribution functions (PDFs) for the shock velocity near the nose region and compared it with the distributions of the ram pressure fluctuations and the derivative of the ram with respect to time fluctuations. We used data from Wind-3DP experiment for very quiet solar wind, and found that a Gaussian fit is quite satisfactory for the time derivative of the ram pressure distribution, but the Gaussian fit to the ram pressure distribution is less satisfactory, a slight offset from the mean and tail in the distribution corresponding to high ram pressure. We developed a simple model for the velocity of the nose distribution function and found it to be consistent with the observations.

We have shown that high speed shock motions are mainly accompanied with significant and sharp changes in solar wind ram pressure observed upstream. The changes are in the most part consistent with the inward and outward motion. An attempt to compare the observed shock velocities with theoretical predictions based on a gas dynamics model have been carried out. Our estimate of the ram pressure temporal changes provides shock velocity values that are in good agreement with the observations. These results are in agreement with the theoretical predictions of Völk and Auer [58] seminal work. Tangential discontinuities are a major driver to shock motion with speeds larger than $\approx$ 80 km/s. For such cases, and when compared to the

Mach number, we found that the ram pressure variations are a dominant factor when fast shock motions occur.

Bibliography

[1] A. Balogh, C. M. Carr, M. H. Acuna, M. W. Dunlop, T. J. Beek, P. Brown, K. H. Fornacon, E. Georgescu, K. H. Glassmeier and J. Harris. *The cluster magnetic field investigation:Overview of in-flight performance and initial results*, Annales Geophysicae 2001.

[2] C. P. Escoubet, M. Fehringer and M. Goldstein. *The cluster mission*,Ann. Geophys 19(10/12), pp. 1197-1200. 2001.

[3] S. J. Schwartz. *Shock and Discontinuity Normals, Mach Numbers, and Related Parameters*,Analysis methods for multi-spacecraft data,edited by G.Paschmann and P.W.Daly.Int.Space Sci 1998.

[4] C. C. Harvey. *Spatial gradients and the volumetric tensor.* In Analysis methods for multi-spacecraft data,edited by G.Paschmann and P.W.Daly.Int.Space Sci 1998.

[5] C. Escoubet, R. Schmidt and M. Goldstein. *Cluster-science and mission overview.* In The Cluster and Phoenix MissionsAnonymous 1997.

[6] M. Taylor, C. Escoubet, H. Laakso, A. Masson and M. Goldstein. *The cluster mission: Space plasma in three dimensions*, in The Cluster Active ArchiveAnonymous 2010.

[7] T. S. Horbury, P. J. Cargill, E. A. Lucek, J. Eastwood, A. Balogh, M. W. Dunlop, K. H. Fornacon and E. Georgescu. *Four spacecraft measurements of the quasiperpendicular terrestrial bow shock: Orientation and motion*. Journal of Geophysical Research 107(A8), pp. 1208. 2002.

[8] H. Reme, C. Aoustin, J. Bosqued, I. Dandouras, B. Lavraud, J. Sauvaud, A. Barthe, J. Bouyssou, T. Camus and O. Coeur-Joly. *First multispacecraft ion measurements in and near the earth's magnetosphere with the identical cluster ion spectrometry (CIS) experiment*. Presented at Annales Geophysicae. 2001.

[9] H. Reme, J. Bosqued, J. Sauvaud, A. Cros, J. Dandouras, C. Aoustin, J. Bouyssou, T. Camus, J. Cuvilo and C. Martz. *The cluster ion spectrometry (CIS) experiment.* In The Cluster and Phoenix Missions Anonymous 1997.

[10] I. Dandouras, A. Barthe, E. Penou, S. Brunato, H. Rme, L. Kistler, M. Bavassano-Cattaneo and A. Blagau. *Cluster ion spectrometry (CIS) data in the cluster active archive (CAA).* In The Cluster Active Archive Anonymous 2010.

[11] J. Gloag, E. Lucek, L. Alconcel, A. Balogh, P. Brown, C. Carr, C. Dunford, T. Oddy and J. Soucek.*FGM data products in the CAA.*In The Cluster Active Archive Anonymous 2010.

[12] E.Lucek, L.-N.Alconcel, P.Brown, C.Carr, H.Lewtas, T.Oddy.*User guide to the FGM measurements in the cluster active archive (CAA).* ESA, Tech. Rep. CAA-EST-UG-FGM, Cluster Active Archive. 2011.

[13] I.Dandouras, A.Barthe.*User guide to the CIS measurements in the Cluster Active Archive (CAA).* ESA, Tech. Rep.CAA-EST-UG-CIS, Cluster Active Archive. 2011.

[14] D. McComas, S. Bame, P. Barker, W. Feldman, J. Phillips, P. Riley and J. Griffee.*Solar wind electron proton alpha monitor (SWEPAM) for the advanced composition explorer.* In The Advanced Composition Explorer Mission Anonymous 1998.

[15] C. W. Smith, J. LHeureux, N. F. Ness, M. H. Acua, L. F. Burlaga and J. Scheifele.*The ACE magnetic fields experiment.* In The Advanced Composition Explorer Mission Anonymous 1998.

[16] B. Mailyan, C. Munteanu and S. Haaland. *What is the best method to calculate the solar wind propagation delay?* Presented at Annales Geophysicae. 2008.

[17] M. R. Aellig, A. J. Lazarus and J. T. Steinberg. *The solar wind helium abundance: Variation with wind speed and the solar cycle*. Geophys. Res. Lett. 28(14), pp. 2767-2770. 2001.

[18] K. W. Ogilvie and T. D. Wilkerson. *Helium abundance in the solar wind*. Solar Physics 8(2), pp. 435-449. 1969.

[19] S. J. Schwartz.*Shock and Discontinuity Normals, Mach Numbers, and Related Parameters*Presented at Analysis methods for multi-spacecraft data.Int. Space Sci, pp.249-270. 1998.

[20] C.Mazelle,B.Lembge,A.Morgenthaler,K.Meziane,T.S.Horbury,V.Gnot, E.A.Lucek, I.Dandouras. *Self-reformation of the quasi-perpendicular shock: Cluster observations*. Presented at AIP Conference Proceedings. 2010, .

[21] Y. Hobara, M. Balikhin, V. Krasnoselskikh, M. Gedalin and H. Yamagishi. *Statistical study of the quasi?perpendicular shock ramp widths*. Journal of Geophysical Research: Space Physics (19782012) 115(A11), 2010.

[22] A.Seiff.*Recent Information on Hypersonic Flow Fields*. Presented at Gas Dynamics in Space Explorations. NASA SP-24, pages, published by NASA, Washington, D.C., December 1962.

[23] J. R. Spreiter, A. L. Summers and A. Y. Alksne.*Hydromagnetic flow around the magnetosphere*. Planet. Space Sci. 14(3), pp. 223-223. 1966.

[24] J. R. Spreiter and A. W. Rizzi. *Aligned magnetohydrodynamic solution for solar wind flow past the earth's magnetosphere*. Acta Astronaut. 1(1), pp. 15-35. 1974.

[25] M. H. Farris and C. T. Russell.*Determining the standoff distance of the bow shock: Mach number dependence and use of models*. Journal of Geophysical Research 99(A9), pp. 17681-17,689. 1994.

[26] D. G. Sibeck, R. E. Lopez and E. C. Roelof. *Solar wind control of the magnetopause shape, location, and motion*. Journal of Geophysical Research 96(A4), pp. 5489-5495. 1991.

[27] J. Merka, A. Szabo, T. W. Narock, J. D. Richardson and J. H. King.*Three decades of bow shock observations by IMP 8 and model predictions*. Planet. Space Sci. 53(1), pp. 79-84. 2005.

[28] J. H. Shue, J. K. Chao, H. C. Fu, C. T. Russell, P. Song, K. K. Khurana and H. J. Singer.*A new functional form to study the solar wind control of the magnetopause size and shape*. Journal of Geophysical Research 102(A5), pp. 9497-9511. 1997.

[29] M. Maksimovic, S. D. Bale, T. S. Horbury and M. Andr. *Bow shock motions observed with CLUSTER*. Geophys. Res. Lett. 30(7), pp. 1393. 2003.

[30] I. H. Cairns and J. G. Lyon.*MHD simulations of Earths bow shock at low mach numbers: Standoff distances*. Journal of Geophysical Research 100(A9), pp. 17173-17,180. 1995.

[31] J. Merka, A. Szabo, T. W. Narock, J. H. King, K. I. Paularena and J. D. Richardson.*A comparison of IMP 8 observed bow shock positions with model predictions*. J.Geophys.Res 108(A2), pp. 1077. 2003.

[32] J. Merka, A. Szabo, T. W. Narock, J. D. Richardson and J. H. King.*Three decades of bow shock observations by IMP 8 and model predictions*. Planet. Space Sci. 53(1), pp. 79-84. 2005.

[33] J. Merka, A. Szabo, J. A. Slavin, M. Peredo.*Three-dimensional position and shape of the bow shock and their variation with upstream Mach numbers and interplanetary magnetic field orientation*. Journal of Geophysical Research-Space Physics, vol. 110, 2005.

[34] C. Mazelle, B. Lembège, A. Morgenthaler, K. Meziane, T. Horbury, V. Génot, E. Lucek and I. Dandouras.*Self-reformation of the quasi-perpendicular shock: Cluster observations*. Presented at AIP Conference Proceedings. 2010, .

[35] K. Meziane, T.Y. Alrefay and A. Hamza.*On the shape and motion of the earth's bow shock*. Planet. Space Sci.93-94, pp 1-9 2014.

[36] D. H. Fairfield. *Average and unusual locations of the Earths magnetopause and bow shock*. Journal of Geophysical Research 76(28), pp. 6700-6716. 1971.

[37] V. Formisano, V. Domingo and K. P. Wenzel. *The three-dimensional shape of the magnetopause*. Planet. Space Sci. 27(9), pp. 1137-1149. 1979.

[38] V. Formisano, P. C. Hedgecock, G. Moreno, J. Sear and D. Bollea. *Observations of earth's bow shock for low mach numbers*. Planet. Space Sci. 19(11), pp. 1519-1531. 1971.

[39] Formisano,V., Hedgecock,P.C., *Solar wind interaction with the Earth's magnetic field. 3. On the Earth's bow shock structure*. J. Geophys. Res, vol. 78, pp. 3745-3760, 1973.

[40] V. Formisano and G. Mastrantonio. *On the Earths bow shock motion and speed*. In The Magnetospheres of the Earth and JupiterAnonymous 1975, .

[41] M. Peredo, J. A. Slavin, E. Mazur and S. A. Curtis. *Three-dimensional position and shape of the bow shock and their variation with alfvenic, sonic and magnetosonic mach numbers and interplanetary magnetic field orientation*. Journal of Geophysical Research 100(A5), pp. 7907-7916. 1995.

[42] C. T. Russell, M. M. Mellott, E. J. Smith and J. H. King. *Multiple spacecraft observations of interplanetary shocks four spacecraft determination*

of shock normals. Journal of Geophysical Research 88pp. 4739-4748. 1983.

[43] C. T. Russell, M. M. Hoppe, W. A. Livesey, J. T. Gosling and S. J. Bame.*ISEE-1 and-2 observations of laminar bow shocks- velocity and thickness*. Geophys. Res. Lett. 9pp. 1171-1174. 1982.

[44] S. Petrinec and C. Russell.*Near?Earth magnetotail shape and size as determined from the magnetopause flaring angle*. Journal of Geophysical Research: Space Physics (19782012) 101(A1), pp. 137-152. 1996.

[45] C. Russell. *Planetary bow shocks*. Geophysical Monograph Series 35pp. 109-130. 1985.

[46] C. Russell and T. Zhang.*Unusually distant bow shock encounters at venus*. Geophys. Res. Lett. 19(8), pp. 833-836. 1992.

[47] M. H. Farris, S. M. Petrinec and C. T. Russell.*The thickness of the magnetosheath: Constraints on the polytropic index*. Geophys. Res. Lett. 18(10), pp. 1821-1824. 1991.

[48] M. H. Farris and C. T. Russell.*Determining the standoff distance of the bow shock: Mach number dependence and use of models*. Journal of Geophysical Research 99(A9), pp. 17681-17,689. 1994.

[49] J. Slavin, R. Holzer, J. Spreiter and S. Stahara.*Planetary mach cones: Theory and observation*. Journal of Geophysical Research: Space Physics (19782012) 89(A5), pp. 2708-2714. 1984.

[50] J. A. Slavin and R. E. Holzer.*Solar wind flow about the terrestrial planets. I- modeling bow shock position and shape*. Journal of Geophysical Research 86pp. 11401-11418. 1981.

[51] J. K. Guha, D. L. Judge and J. H. Marburger.*OGO 5 magnetic-field data near the Earths bow shock: A correlation with theory*. Journal of Geophysical Research 77(4), pp. 604-610. 1972.

[52] B. Lembège, P. Savoini, P. Hellinger and P. M. Trávníček.*Nonstationarity of a two?dimensional perpendicular shock: Competing mechanisms*. Journal of Geophysical Research: Space Physics (19782012) 114(A3), 2009.

[53] S. Lepidi, U. Villante, A. J. Lazarus, A. Szabo and K. Paularena.*Observations of bow shock motion during times of variable solar wind conditions*. Journal of Geophysical Research 101(A5), pp. 11107-11,123. 1996.

[54] M. Maksimovic, S. D. Bale, T. S. Horbury and M. Andr.*Bow shock motions observed with CLUSTER*. Geophys. Res. Lett. 30(7), pp. 1393. 2003.

[55] J. A. Newbury, C. T. Russell and M. Gedalin.*The ramp widths of high-mach-number, quasi-perpendicular collisionless shocks*. Journal of Geophysical Research 103(A12), pp. 29581-29,593. 1998.

[56] J. Šafránková, K. Jelnek and Z. Němeček. *The bow shock velocity from two-point measurements in frame of the INTERBALL project.* Advances in Space Research 31(5), pp. 1377-1382. 2003.

[57] J. Šafránková , Z. Němeček and M. Borák. *MAGION-4 observations of bow shock crossings.* Czechoslovak Journal of Physics 49pp. 563-578. 1999.

[58] H. J. Völk and R. D. Auer. *Motions of the bow shock induced by interplanetary disturbances.* Journal of Geophysical Research 79(1), pp. 40-48. 1974.

[59] G. Zastenker, C. Russell, H. Bridge, A. Lazarus, V. Smirnov, Z. Němeček and J. Šafránková. *Bow shock motion with two-point observations: Prognoz 7, 8 and ISEE 1, 2; prognoz 10 and IMP 8.* Advances in Space Research 8(9), pp. 171-174. 1988.

[60] Z. Němeček, J. Šafránková and G. Zastenker. *Dynamics of the earth's bow shock position.* Advances in Space Research 8(9), pp. 167-170. 1988.

[61] Z. Němeček and J. Šafránková. *The earth's bow shock and magnetopause position as a result of the solar wind-magnetosphere interaction.* J. Atmos. Terr. Phys. 53(11), pp. 1049-1054. 1991.

[62] L.D. Landau and E.M. Lifshitz. *Fluid Mecanica.* New York: Pergamon, 1959.

[63] V. Thomas and S. H. Brecht.*Angular dependence of high mach number plasma interactions*. Journal of Geophysical Research: Space Physics (19782012) 92(A4), pp. 3175-3186. 1987.

[64] I. H. Cairns and C. L. Grabbe.*Towards an MHD theory for the standoff distance of earth's bow shock*. Geophys. Res. Lett. 21(25), pp. 2781-2784. 1994.

[65] T. E. Cravens.*Physics of Solar System Plasmas*, Cambridge University Press 1997.

[66] M. Verigin, G. Kotova, J. Slavin, A. Szabo, M. Kessel, J. Safrankova, Z. Nemecek, T. Gombosi, K. Kabin and F. Shugaev.*Analysis of the 3-D shape of the terrestrial bow shock by Interball/Magion 4 observations*. Advances in Space Research 28(6), pp. 857-862. 2001.

[67] M. Verigin, G. Kotova, A. Remizov, V. Styazhkin, N. Shutte, T. Zhang, W. Riedler, H. Rosenbauer, K. Szeg and M. Tatrallyay. *Shape and location of planetary bow shocks*. Kosmicheskie Issledovaniia 37pp. 38-43. 1999.

[68] M. Verigin, J. Slavin, A. Szabo, T. Gombosi, G. Kotova, O. Plochova, K. Szeg, M. Ttrallyay, K. Kabin and F. Shugaev.*Planetary bow shocks: Gasdynamic analytic approach*. Journal of Geophysical Research: Space Physics 108(A8), 2003.

[69] J. Chao, D. Wu, C. Lin, Y. Yang, X. Wang, M. Kessel, S. Chen and R. Lepping.*Models for the size and shape of the earth's magnetopause and bow shock*. Presented at Cospar Colloquia Series. 2002.

[70] A. Dmitriev, J. Chao and D. Wu.*Comparative study of bow shock models using wind and geotail observations*. Journal of Geophysical Research: Space Physics (19782012) 108(A12), 2003.

[71] K. Jelńek, Z. Němeček and J. Šafránková.*A new approach to magnetopause and bow shock modeling based on automated region identification*. Journal of Geophysical Research: Space Physics (19782012) 117(A5), 2012.

[72] E. W. Greenstadt, I. M. Green, G. T. Inouye, A. J. Hundhausen, S. J. Bame and I. B. Strong.*Correlated magnetic field and plasma observations of the Earth's bow shock*. Journal of Geophysical Research: Space Physics. 73, pp. 51-60. 1968.

[73] E. Greenstadt.*Observation of nonuniform structure of the earth's bow shock correlated with interplanetary field orientation*. Journal of Geophysical Research 77(10), pp. 1729-1738. 1972.

[74] R. E. Holzer, M. G. McLeod and E. J. Smith.*Preliminary results from the OGO 1 search coil magnetometer: Boundary positions and magnetic noise spectra*. Journal of Geophysical Research 71(5), pp. 1481-1486. 1966

[75] K. Tsubouchi, T. Terasawa, T. Mukai, Y. Saito, T. Yamamoto, S. Kokubun, H. Kojima and H. Matsumoto.*Motion of the earth's bow shock in the deep?tail flank*. Journal of Geophysical Research: Space Physics (19782012) 105(A11), pp. 25097-25112. 2000.

[76] G. R. Smit.*Oscillatory motion of the nose region of the magnetopause*. Journal of Geophysical Research 73(15), pp. 4990-4993. 1968.

[77] R. Lepping and P. Argentiero. *Single spacecraft method of estimating shock normals*. Journal of Geophysical Research 76(19), pp. 4349-4359. 1971.

[78] H. Zhuang and C. Russell. *An analytic treatment of the structure of the bow shock and magnetosheath*. Journal of Geophysical Research 86(A4), pp. 2191-2205. 1981.

[79] C. Wu, J. Gaffey and B. Liberman. *Statistical acceleration of electrons by lower-hybrid turbulence*. Journal of Plasma Physics 25(03), pp. 391-401. 1981.

[80] M. Scholer and S. Matsukiyo.*Nonstationarity of quasi-perpendicular shocks: A comparison of full particle simulations with different ion to electron mass ratio*. Presented at Annales Geophysicae. 2004.

[81] S. Matsukiyo and M. Scholer. *Modified two?stream instability in the foot of high mach number quasi?perpendicular shocks*. Journal of Geophysical Research: Space Physics (19782012) 108(A12), 2003.

[82] B. Lembége, P. Savoini, P. Hellinger and P. M. Trávniček.*Nonstationarity of a two?dimensional perpendicular shock: Competing mechanisms*. Journal of Geophysical Research: Space Physics (19782012) 114(A3), 2009.

[83] Bruce T. Tsurutani, Robert G. Stone, *Collisionless Shocks in the Heliosphere: Reviews of Current Research*. AGU Monograph, Vol. 35, 1985.

Appendix A

General Solution to the Rankine-Hugoniot Conservation Equations

We present in this section the different steps towards the resolution of the Rankine-Hugoniot Equations. First, let us define the useful following quantities:

- The solar wind velocity: $\vec{U} = U\hat{u}$
- The ambiant IMF: $\vec{B} = B\hat{b}$
- The shock normal: $\hat{n}$

along with:

$$\begin{cases} s &= \hat{b}\cdot\hat{u} = \cos(\hat{b},\hat{u}) = \cos\psi \\ r &= \hat{b}\cdot\hat{n} = \cos(\hat{b},\hat{n}) = \cos\theta \\ t &= \hat{n}\cdot\hat{u} = \cos(\hat{n},\hat{u}) = \cos\beta \end{cases}$$

We also define c to be the coplanarity factor as follows:

$$c = \hat{u}\cdot(\hat{n}\times\hat{b}) \tag{A.1}$$

$c = 0$ if coplanarity is satisfied.

Let us define

$$k^2 = r^2 - 2rst + t^2 \tag{A.2}$$

if $c = 0$ then $\hat{u}\cdot(\hat{n}\times\hat{b}) = \cos\left[\hat{u},\hat{n}\times\hat{b}\right] = 0$, then the coplanarity condition leads to:

$$\beta + \psi - \theta = \pi \tag{A.3}$$

using the coplanarity condition one can show that

$$k^2 = 1 - s^2 \quad ork = \sqrt{1-s^2} \tag{A.4}$$

A.0.1 The $\vec{E}\times\vec{B}$ drift velocity

$$\vec{V}_D = \frac{\vec{E}\times\vec{B}}{B^2} \quad with \quad \vec{E} = -\vec{U}\times\vec{B} \tag{A.5}$$

the drift can be shown to take the following form:

$$\vec{V}_D = \frac{U}{B}(\hat{u} - s\hat{b}) \tag{A.6}$$

the unit vector along the $\vec{E} \times \vec{B}$ drift velocity can be expressed as:

$$\hat{v}_D = \frac{\hat{u} - s\hat{b}}{\sqrt{1 - s^2}} \tag{A.7}$$

A.0.2 The Hoffman-Teller Velocity

By definition we have

$$\vec{V}_{HT} = \frac{\hat{n} \times (\hat{u} \times \hat{b})UB}{\hat{b} \cdot \hat{n}B} = \frac{U}{r}\left[(\hat{n} \cdot \hat{b})\hat{u} - (\hat{n} \cdot \hat{u})\hat{b}\right] \tag{A.8}$$

which leads to:

$$\vec{V}_{HT} = U\left(\hat{u} - \frac{t}{r}\hat{b}\right) \tag{A.9}$$

The magnitude of the "de Hoffmann-Teller" velocity can be calculated and shown to be:

$$V_{HT} = \frac{k}{r}U \tag{A.10}$$

and the unit vector along the "de Hoffmann-Teller" velocity can be expressed as:

$$\hat{v}_{HT} = \frac{r}{k}\hat{u} - \frac{t}{k}\hat{b} \tag{A.11}$$

A.1 The shock Frame

we define the shock-frame through the following unit vectors:

$$\begin{cases} \hat{e}_x &= \hat{n} \\ \hat{e}_y &= \hat{n}_1 = \hat{n}_2 \times \hat{n} = \frac{1}{\sqrt{1-s^2}}(t\hat{n} \times \hat{b} - r\hat{n} \times \hat{u}) \\ \hat{e}_z &= \hat{n}_2 = \frac{1}{\sqrt{1-s^2}}(t\hat{b} - r\hat{u}) = -\hat{v}_{HT} \end{cases}$$

where again

$$\begin{cases} r &= \hat{n} \cdot \hat{b} \\ t &= \hat{n} \cdot \hat{u} \\ s &= \hat{u} \cdot \hat{b} \end{cases}$$

within this frame, one can express the vectors $\vec{U}$ and $\vec{B}$ in the following form:

$$\begin{aligned} \vec{U} &= tU\hat{e}_x - \frac{tc}{k}U\hat{e}_y - \frac{r-st}{k}U\hat{e}_z \\ \hat{u} &= t\hat{e}_x - \frac{tc}{k}\hat{e}_y - \frac{r-st}{k}\hat{e}_z \end{aligned} \tag{A.12}$$

and

$$\begin{aligned} \vec{B} &= Br\hat{e}_x - \frac{rc}{k}B\hat{e}_y - \frac{sr-t}{k}B\hat{e}_z \\ \hat{u} &= r\hat{e}_x - \frac{rc}{k}\hat{e}_y - \frac{sr-t}{k}\hat{e}_z \end{aligned} \tag{A.13}$$

The Rankine-Hugoniot Relations

The jump conditions at the shock alls us to determine the downstream components of the plasma given the upstream ones. In what follows the subscript

of 2 indicates the values downstream of the shock.

$$[B_n] = 0 \quad \text{(A.14)}$$

$$[E_t] = 0 \quad \text{(A.15)}$$

$$[\rho(U_n - V_s)] = 0 \quad \text{(A.16)}$$

$$\left[\rho(U_n - V_s)(\vec{U} - \vec{V}_s) + P\hat{n} - \frac{B_n}{\mu_0}\vec{B} + \frac{B^2}{2\mu_0}\hat{n}\right] = 0 \quad \text{(A.17)}$$

$$\left[\frac{1}{2}\rho(U_n - V_s)(\vec{U} - \vec{V}_s)^2 + \frac{\gamma}{\gamma - 1}P(U_n - V_s) + S_n\right] = 0 \quad \text{(A.18)}$$

where

$$\vec{S} = \frac{1}{\mu_0}\vec{E} \times \vec{B} = \frac{1}{\mu_0}\left[B^2(\vec{U} - \vec{V}_s) - (\vec{U} - \vec{V}_s) \cdot \vec{B}\vec{B}\right] \quad \text{(A.19)}$$

within the shock frame one can express the following quantities:

$$S_n = \vec{S} \cdot \hat{n} = \frac{1}{\mu_0}\left[B^2(U_n - V_s) - B_n(\vec{U} - \vec{V}_s) \cdot \vec{B}\right] \quad \text{(A.20)}$$

$$\vec{E} = -(\vec{U} - \vec{V}_s) \times \vec{B}$$

$$= (U_z B_y - U_y B_z)\hat{e}_x + (U_x B_z - U_z B_x)\hat{e}_y + (U_y B_x - U_x B_y)\hat{e}_z - V_s B_z \hat{e}_y + V_s B_y \hat{e}_z \quad \text{(A.21)}$$

The RH equations become:

$$B_{2n} = B_{2x} = B_n = Br \tag{A.22}$$

Equation A.16 leads to the following continuity expression:

$$\rho_2 U_{2n} = \rho U_n + (\rho_2 - \rho) V_s \tag{A.23}$$

we now introduce the following variable

$$x = \frac{\rho}{\rho_2}, \quad 0 < x \leq 1 \tag{A.24}$$

For a shock solution only $x < 1$ is acceptable.

We define the variables η and α as

$$\eta = \frac{V_s}{U_n} \quad ; \quad \alpha = 1 - \eta \tag{A.25}$$

which allows us to rewrite equation (A.23) in the following form

$$\frac{U_{2n}}{U_n} = x + (1 - x)\eta \tag{A.26}$$

The tangential components of the electric field can be computed and inserted in equation (A.15) which leads to:

$$(U_{2n} - V_s)B_{2z} - U_{2z}Br = (U_n - V_s)B_z - U_z Br \tag{A.27}$$

and

$$-(U_{2n} - V_s)B_{2y} + U_{2y}Br = -(U_n - V_s)B_y + U_y Br \tag{A.28}$$

The $\hat{n}$-component of equation (A.17) can be explicitly written as:

$$\rho_2(U_{2n} - V_s)^2 + P_2 + \frac{B_{2y}^2}{2\mu_0} + \frac{B_{2z}^2}{2\mu_0} = \rho(U_n - V_s)^2 + P + \frac{B_y^2}{2\mu_0} + \frac{B_z^2}{2\mu_0} \tag{A.29}$$

where we used equation (A.22). The y-component and the z-component of equation (A.17) lead to:

$$\rho_2(U_{2n} - V_s)U_{2y} - \frac{B_{2y}Br}{\mu_0} = \rho(U_n - V_s)U_y - \frac{B_y Br}{\mu_0} \tag{A.30}$$

$$\rho_2(U_{2n} - V_s)U_{2z} - \frac{B_{2z}Br}{\mu_0} = \rho(U_n - V_s)U_z - \frac{B_z Br}{\mu_0} \tag{A.31}$$

Finally equation (A.18) can be developed and written in the following form:

$$\frac{1}{2}\rho_2\left[(U_{2n} - V_s)^3 + (U_{2y}^2 + U_{2z}^2)(U_{2n} - V_s)\right] + \frac{\gamma}{\gamma - 1}P_2(U_{2n} - V_s) + S_{2n}$$

$$= \tag{A.32}$$

$$\frac{1}{2}\rho\left[(U_n - V_s)^3 + (U_y^2 + U_z^2)(U_n - V_s)\right] + \frac{\gamma}{\gamma - 1}P(U_n - V_s) + S_n$$

Let us define the following variables, which will enable us to rewrite the 'RH'

equations in a very compact form:

$$\beta_{y,z} = \frac{U_{2y,z}}{U_n} \quad ; \quad \gamma_{y,z} = \frac{B_{2y,z}}{U\sqrt{\mu_0\rho}} \quad ; \quad M_A = \frac{U}{B/\sqrt{\mu_0\rho}} \quad ; \quad m = \frac{r}{M_A} \tag{A.33}$$

This allows us to rewrite equations (A.27) and (A.28) in the following form:

$$\begin{aligned} (\alpha\gamma_y)x - m\beta_y &= a_y = \alpha\frac{B_y}{U\sqrt{\mu_0\rho}} - m\frac{U_y}{U_n} \\ (\alpha\gamma_z)x - m\beta_z &= a_z = \alpha\frac{B_z}{U\sqrt{\mu_0\rho}} - m\frac{U_z}{U_n} \end{aligned} \tag{A.34}$$

Equations (A.30) and (A.31) can be further simplified by introducing

$$\delta = \frac{U}{U_n} \tag{A.35}$$

to obtain

$$\begin{aligned} \alpha\beta_y - \delta^2 m\gamma_y &= a_y^{'} = \alpha\frac{U_y}{U_n} - \delta^2 m\frac{B_y}{U\sqrt{\mu_0\rho}} \\ \alpha\beta_z - \delta^2 m\gamma_z &= a_z^{'} = \alpha\frac{U_z}{U_n} - \delta^2 m\frac{B_z}{U\sqrt{\mu_0\rho}} \end{aligned} \tag{A.36}$$

Combining equations (A.34), (A.36), one obtains:

$$\begin{aligned} \gamma_y &= \frac{\alpha a_y + m a_y^{'}}{\alpha^2 x - m^2\delta^2} \\ \gamma_z &= \frac{\alpha a_z + m a_z^{'}}{\alpha^2 x - m^2\delta^2} \end{aligned} \tag{A.37}$$

similarly

$$\begin{aligned} \beta_y &= \frac{m\delta^2 a_y + \alpha a_y^{'} x}{\alpha^2 x - m^2\delta^2} \\ \beta_z &= \frac{m\delta^2 a_z + \alpha a_z^{'} x}{\alpha^2 x - m^2\delta^2} \end{aligned} \tag{A.38}$$

Equation (A.29) becomes

$$\alpha^2 x + \frac{P_2}{\rho U_n^2} + \frac{\delta^2}{2}(\gamma_y^2 + \gamma_z^2) = \alpha^2 + \frac{\delta^2}{\gamma M_S^2} + \frac{\delta^2}{2}\left(\frac{1}{M_A^2} - m^2\right) \tag{A.39}$$

where we have defined

$$M_S = \frac{U}{C_s} \quad ; \quad C_s^2 = \frac{\gamma P}{\rho} \tag{A.40}$$

A similar treatment of equation (A.32) leads to

$$\begin{aligned} &\frac{1}{2}\alpha^3 x^2 + \frac{1}{2}\alpha(\beta_y^2 + \beta_z^2) + \frac{\gamma}{\gamma - 1}\alpha\frac{P_2}{\rho U_n^2}x + \delta^2(\gamma_y^2 + \gamma_z^2)\alpha x - m\delta^2(\beta_y\gamma_y + \beta_z\gamma_z) \\ &= \\ &\frac{1}{2}[\alpha^3 + \alpha(\delta^2 - 1)] + \frac{\gamma}{\gamma - 1}\alpha\delta^2\frac{1}{\gamma M_S^2} + \alpha\delta^2\left(\frac{1}{M_A^2} - m^2\right) \\ &-m\delta^2\left(\frac{U_y}{U_n}\frac{B_y}{U\sqrt{\mu_0\rho}} + \frac{U_z}{U_n}\frac{B_z}{U\sqrt{\mu_0\rho}}\right) \\ &= \\ &\frac{1}{2}[\alpha^3 + \alpha(\delta^2 - 1)] + \alpha\delta^2\left(\frac{1}{M_A^2} + \frac{1}{\gamma - 1}\frac{1}{\gamma M_S^2}\right) - \frac{\delta^3 s}{M_A}m + \delta^2(\alpha - 1)m^2 \end{aligned} \tag{A.41}$$

From equation (A.39) we can obtain the pressure term

$$\frac{P_2}{\rho U_n^2} = \alpha^2 + \frac{\delta^2}{\gamma M_S^2} + \frac{\delta^2}{2}\left(\frac{1}{M_A^2} - m^2\right) - \alpha^2 x - \frac{\delta^2}{2}(\gamma_y^2 + \gamma_z^2)$$

The next step is to simplify and rewrite the expressions derived in terms of the dimensionless variables.

$$\begin{aligned} a_y^2 + a_z^2 &= \left(\frac{\alpha}{M_A}\right)^2 - 2m\delta s\left(\frac{\alpha}{M_A}\right) - (\alpha - 1 - \delta)(\alpha - 1 + \delta)m^2 \\ a_y^{'2} + a_z^{'2} &= \alpha^2(\delta^2 - 1) - 2\frac{\alpha\delta^3 s}{M_A}m + \delta^2\left(2\alpha + \frac{\delta^2}{M_A^2}\right)m^2 - \delta^4 m^4 \\ a_y a_y^{'} + a_z a_z^{'} &= \alpha^2\frac{\delta s}{M_A} + \alpha(1 - \alpha - \frac{\delta^2}{M_A^2} - \delta^2)m + \frac{\delta^3 s}{M_A}m^2 + \delta^2(\alpha - 1)m^3 \end{aligned} \tag{A.42}$$

This in turn leads to:

$$(\alpha^2 x - m^2\delta^2)^2(\gamma_y^2+\gamma_z^2) = \frac{\alpha^4}{M_A^2} - \alpha^2\left(\alpha + 2\frac{\delta^2}{M_A^2}\right)m^2 + \delta^2\left(2\alpha^2 + \frac{\delta^2}{M_A^2}\right)m^4 - \delta^4 m^6$$

$$\begin{aligned}(\alpha^2 x - m^2\delta^2)^2(\beta_y^2+\beta_z^2) = &\left[\alpha^2(\delta^2-1) - 2\frac{\alpha\delta^3 s}{M_A}m + \delta^2\left(2\alpha + \frac{\delta^2}{M_A^2}\right)m^2 - \delta^4 m^4\right]\alpha^2 x^2 \\ &+ 2\delta^2 m\left[\frac{\alpha^2\delta s}{M_A} + \alpha(1-\alpha-\frac{\delta^2}{M_A^2}-\delta^2)m + \frac{\delta^3 s}{M_A}m^2 + \delta^2(\alpha-1)m^3\right]\alpha x \\ &+ m^2\delta^4\left[\left(\frac{\alpha}{M_A}\right)^2 - 2m\delta s\left(\frac{\alpha}{M_A}\right) - (\alpha-1-\delta)(\alpha-1+\delta)m^2\right]\end{aligned}$$

and

$$\begin{aligned}&(\alpha^2 x - m^2\delta^2)^2(\beta_y\gamma_y + \beta_z\gamma_z) = \\ &\left[\frac{\alpha^3\delta s}{M_A} - \left(\alpha + \frac{\delta^2}{M_A^2}\right)\alpha^2 m - \frac{\alpha\delta^3 s}{M_A}m^2 + \delta^2\left(\alpha^2 + \alpha + \frac{\delta^2}{M_A^2}\right)m^3 - \delta^4 m^5\right]\alpha x \\ &+\left[\frac{\alpha^3\delta^2}{M_A^2}m - \frac{\alpha^2\delta^3 s}{M_A}m^2 - \alpha\delta^2\left(\alpha - \alpha^2 - \frac{\delta^2}{M_A^2}\right)m^3 + \frac{\delta^5 s}{M_A}m^4 + \delta^4(\alpha-1)m^5\right]\end{aligned} \tag{A.43}$$

Equation (A.41) can be rewritten in a compact form

$$\begin{aligned}&\frac{1}{2}\left(\frac{1+\gamma}{1-\gamma}\right)(\alpha^2 x - m^2\delta^2)^2\alpha^3 x^2 \\ &+\frac{1}{2}\alpha^3\left[\alpha^2(\delta^2-1) - 2\frac{\alpha\delta^3 s}{M_A}m + \delta^2\left(2\alpha + \frac{\delta^2}{M_A^2}\right)m^2 - \delta^4 m^4\right]x^2 \\ &+\delta^2\alpha^2 m\left[\frac{\alpha^2\delta s}{M_A} + \alpha(1-\alpha-\frac{\delta^2}{M_A^2}-\delta^2)m + \frac{\delta^3 s}{M_A}m^2 + \delta^2(\alpha-1)m^3\right]x \\ &+\frac{1}{2}\alpha m^2\delta^4\left[\left(\frac{\alpha}{M_A}\right)^2 - 2m\delta s\left(\frac{\alpha}{M_A}\right) - (\alpha-1-\delta)(\alpha-1+\delta)m^2\right]\end{aligned}$$

$$+\frac{\gamma}{\gamma-1}\left[\alpha^2+\frac{\delta^2}{\gamma M_S^2}+\frac{\delta^2}{2}\left(\frac{1}{M_A^2}-m^2\right)\right](\alpha^2x-m^2\delta^2)^2\alpha x$$

$$+\frac{1}{2}\left(\frac{\gamma-2}{\gamma-1}\right)\left[\frac{\alpha^4}{M_A^2}-\alpha^2\left(\alpha+2\frac{\delta^2}{M_A^2}\right)m^2+\delta^2\left(2\alpha^2+\frac{\delta^2}{M_A^2}\right)m^4-\delta^4m^6\right]\alpha\delta^2x$$

$$-m\delta^2\left[\frac{\alpha^3\delta s}{M_A}-\left(\alpha+\frac{\delta^2}{M_A^2}\right)\alpha^2m-\frac{\alpha\delta^3s}{M_A}m^2+\delta^2\left(\alpha^2+\alpha+\frac{\delta^2}{M_A^2}\right)m^3-\delta^4m^5\right]\alpha x$$

$$-m\delta^2\left[\frac{\alpha^3\delta^2}{M_A^2}m-\frac{\alpha^2\delta^3s}{M_A}m^2-\alpha\delta^2\left(\alpha-\alpha^2-\frac{\delta^2}{M_A^2}\right)m^3+\frac{\delta^5s}{M_A}m^4+\delta^4(\alpha-1)m^5\right]$$

$$=(\alpha^2x-m^2\delta^2)^2\left[\frac{1}{2}\alpha^3+\frac{1}{2}\alpha(\delta^2-1)+\alpha\delta^2\left(\frac{1}{M_A^2}+\frac{1}{\gamma-1}\frac{1}{M_S^2}\right)-\frac{\delta^3s}{M_A}m+\delta^2(\alpha-1)m^2\right] \tag{A.44}$$

Equation (A.44) has the following form

$$a_4x^4+a_3x^3+a_2x^2+a_1x+a_0=0 \tag{A.45}$$

where the coefficients are given by:

$$
\begin{aligned}
a_4 &= \frac{1}{2}\left(\frac{1+\gamma}{1-\gamma}\right)\alpha^7 \\
a_3 &= \frac{1}{2}\left(\frac{\gamma}{\gamma-1}\right)\left[2\left(\alpha^2+\frac{\delta^2}{\gamma M_S^2}+\frac{\delta^2}{2M_A^2}\right)+\frac{\gamma+2}{\gamma}m^2\delta^2\right]\alpha^5 \\
&= \frac{1}{2}\left(\frac{\gamma}{\gamma-1}\right)\left[2\left(\alpha^2+\frac{1}{\gamma}\frac{\delta^2}{M_S^2}+\frac{1}{2}\frac{\delta^2}{M_A^2}\right)+\frac{\gamma+2}{\gamma}\frac{\delta^2}{M_A^2}r^2\right]\alpha^5 \\
a_2 &= -\alpha^5\left[\frac{\alpha^2}{2}+\delta^2\left(\frac{1}{M_A^2}+\frac{1}{\gamma-1}\frac{1}{M_S^2}\right)\right] \\
&+ \delta^2\alpha^3\left[\frac{1}{2}\left(2\alpha+\frac{\delta^2}{M_A^2}\right)-\alpha(1-\alpha)-\frac{2\gamma}{\gamma-1}\left(\alpha^2+\frac{\delta^2}{\gamma M_S^2}+\frac{\delta^2}{2M_A^2}\right)\right]m^2 \\
&= -\alpha^5\left[\frac{\alpha^2}{2}+\frac{\delta^2}{M_A^2}\left(1+\frac{1}{\gamma-1}\frac{M_A^2}{M_S^2}\right)\right] \\
&+ \frac{\delta^2}{M_A^2}\alpha^3\left[\frac{1}{2}\left(2\alpha+\frac{\delta^2}{M_A^2}\right)-\alpha(1-\alpha)-\frac{2\gamma}{\gamma-1}\left(\alpha^2+\frac{1}{\gamma}\frac{\delta^2}{M_S^2}+\frac{1}{2}\frac{\delta^2}{M_A^2}\right)\right]r^2 \\
a_1 &= \frac{1}{2}\left(\frac{\gamma-2}{\gamma-1}\right)\frac{\delta^2}{M_A^2}\alpha^5+\alpha\frac{1}{\gamma-1}\frac{\delta^6}{M_S^2}m^4 \\
&+ \alpha^3\delta^2\left[\frac{3\gamma-2}{\gamma-1}\frac{\delta^2}{M_A^2}+2\delta^2\frac{1}{\gamma-1}\frac{1}{M_S^2}+\frac{1}{2}\frac{\gamma}{\gamma-1}\alpha^2-2\frac{\delta^2}{M_A^2}\right]m^2 \\
&= \frac{1}{2}\left(\frac{\gamma-2}{\gamma-1}\right)\frac{\delta^2}{M_A^2}\alpha^5+\alpha\frac{1}{\gamma-1}\frac{\delta^2}{M_S^2}\frac{\delta^4}{M_A^4}r^4 \\
&+ \alpha^3\frac{\delta^2}{M_A^2}\left[\frac{3\gamma-2}{\gamma-1}\frac{\delta^2}{M_A^2}+2\delta^2\frac{1}{\gamma-1}\frac{1}{M_S^2}+\frac{1}{2}\frac{\gamma}{\gamma-1}\alpha^2-2\frac{\delta^2}{M_A^2}\right]r^2 \\
a_0 &= -\frac{1}{2}\frac{\delta^4\alpha^3}{M_A^2}m^2-\alpha\frac{1}{\gamma-1}\frac{1}{M_S^2}\delta^6m^4 \\
&= -\frac{1}{2}\frac{\delta^4}{M_A^4}\alpha^3r^2-\alpha\frac{1}{\gamma-1}\frac{\delta^2}{M_S^2}\frac{\delta^4}{M_A^4}r^4
\end{aligned}
\tag{A.46}
$$

One can easily verify that $x = 1$ is a solution. In other words, we can show that:

$$a_4 + a_3 + a_2 + a_1 + a_0 = 0 \tag{A.47}$$

which in turn allows us to reduce the polynomial in x to a lower order:

$$a_4x^4 + a_3x^3 + a_2x^2 + a_1x + a_0 = (x-1)(c_3x^3 + c_2x^2 + c_1x + c_0) = 0 \quad \text{(A.48)}$$

The c-coefficients can be identified

$$\begin{aligned}
c_3 &= a_4 = \frac{1}{2}\left(\frac{1+\gamma}{1-\gamma}\right)\alpha^7 \\
c_2 &= a_3 + a_4 = \frac{1}{2}\left(\frac{1+\gamma}{1-\gamma}\right)\alpha^7 \\
&+ \frac{1}{2}\left(\frac{\gamma}{\gamma-1}\right)\left[2\left(\alpha^2 + \frac{\delta^2}{\gamma M_S^2} + \frac{\delta^2}{2M_A^2}\right) + \frac{\gamma+2}{\gamma}m^2\delta^2\right]\alpha^5 \\
&= \alpha^5\left[\frac{1}{2}\alpha^2 + \frac{\gamma}{\gamma-1}\delta^2\left(\frac{1}{\gamma M_S^2} + \frac{1}{2M_A^2}\right) + \delta^2\frac{1}{2}\frac{\gamma+2}{\gamma-1}m^2\right] \\
c_1 &= a_2 + a_3 + a_4 = -\alpha^5\frac{\delta^2}{2M_A^2}\frac{\gamma-2}{\gamma-1} \\
&+ \alpha^3\delta^2\left[\frac{\delta^2}{2M_A^2} - \frac{1}{2}\frac{\gamma}{\gamma-1}\alpha^2 - \frac{2\gamma}{\gamma-1}\delta^2\left(\frac{1}{\gamma M_S^2} + \frac{1}{2M_A^2}\right)\right]m^2 \\
c_0 &= -a_0 = \frac{1}{2}\frac{\delta^4\alpha^3}{M_A^2}m^2 + \alpha\frac{1}{\gamma-1}\frac{1}{M_S^2}\delta^6m^4
\end{aligned} \quad \text{(A.49)}$$

A.1.1 Case $V_s = 0$, $\eta = 0$ and $\alpha = 1$

The set of coefficients is given by:

$$\begin{aligned}
c_3 &= \frac{1}{2}\left(\frac{1+\gamma}{1-\gamma}\right) \\
c_2 &= \left[\frac{1}{2} + \frac{\gamma}{\gamma-1}\delta^2\left(\frac{1}{\gamma M_S^2} + \frac{1}{2M_A^2}\right) + \delta^2\frac{1}{2}\frac{\gamma+2}{\gamma-1}m^2\right] \\
c_1 &= -\frac{\delta^2}{2M_A^2}\frac{\gamma-2}{\gamma-1} + \delta^2\left[\frac{\delta^2}{2M_A^2} - \frac{1}{2}\frac{\gamma}{\gamma-1} - \frac{2\gamma}{\gamma-1}\delta^2\left(\frac{1}{\gamma M_S^2} + \frac{1}{2M_A^2}\right)\right]m^2 \\
c_0 &= \frac{1}{2}\frac{\delta^4}{M_A^2}m^2 + \frac{1}{\gamma-1}\frac{1}{M_S^2}\delta^6 m^4
\end{aligned} \tag{A.50}$$

At the nose of the shock we have $\delta = \frac{U}{U_n} = -1$. This reduces to the following values of the c-coefficients:

$$\begin{aligned}
c_3 &= \frac{1}{2}\left(\frac{1+\gamma}{1-\gamma}\right) \\
c_2 &= \left[\frac{1}{2} + \frac{\gamma}{\gamma-1}\left(\frac{1}{\gamma M_S^2} + \frac{1}{2M_A^2}\right) + \frac{1}{2}\frac{\gamma+2}{\gamma-1}m^2\right] \\
c_1 &= -\frac{1}{2M_A^2}\frac{\gamma-2}{\gamma-1} + \left[\frac{1}{2M_A^2} - \frac{1}{2}\frac{\gamma}{\gamma-1} - \frac{2\gamma}{\gamma-1}\left(\frac{1}{\gamma M_S^2} + \frac{1}{2M_A^2}\right)\right]m^2 \\
c_0 &= \frac{1}{2}\frac{1}{M_A^2}m^2 + \frac{1}{\gamma-1}\frac{1}{M_S^2}m^4
\end{aligned} \tag{A.51}$$

for $\gamma = \frac{5}{3}$ we obtain the following set of coefficients

$$\begin{aligned} c_3 &= -2 \\ c_2 &= \frac{1}{2} + \frac{3}{2M_S^2} + \frac{5}{4M_A^2} + \frac{11}{4}m^2 \\ c_1 &= \frac{1}{4M_A^2} - \left[\frac{5}{4} + \frac{2}{M_A^2} + \frac{3}{M_S^2}\right] m^2 \\ c_0 &= \frac{1}{2M_A^2}m^2 + \frac{3}{2M_S^2}m^4 \end{aligned} \tag{A.52}$$

we can now solve the cubic equation in x

$$x^3 + \frac{c_2}{c_3}x^2 + \frac{c_1}{c_3}x + \frac{c_0}{c_3} = 0 \tag{A.53}$$

where (using $m = \frac{r}{M_A}$)

$$\begin{aligned} a &= \frac{c_2}{c_3} = -\frac{1}{8}\left[2 + \frac{6}{M_S^2} + \frac{5+11r^2}{M_A^2}\right] < 0 \\ b &= \frac{c_1}{c_3} = -\frac{1}{8M_A^2}\left[1 - \left(5 + \frac{8}{M_A^2} + \frac{12}{M_S^2}\right) r^2\right] \\ c &= \frac{c_0}{c_3} = -\frac{r^2}{4M_A^4}\left[1 + 3\frac{r^2}{M_S^2}\right] < 0 \end{aligned} \tag{A.54}$$

the coefficients a and c are negative as is clear from equation (A.54). The next step is to express explicitly the solutions to the cubic polynomial in x.

To do this, we define the following parameters:

$$\begin{aligned} p &= b - \frac{1}{3}a^2 \\ q &= \frac{2}{27}a^3 - \frac{1}{3}ab + c \\ \Delta &= \left(\frac{q}{2}\right)^2 + \left(\frac{p}{3}\right)^3 \end{aligned} \tag{A.55}$$

$$\Delta = \frac{1}{27}a^3c - \frac{1}{108}a^2b^2 + \frac{1}{27}b^3 - \frac{1}{6}abc + \frac{1}{4}c^2 \tag{A.56}$$

If $x = x_0$ is the shock solution satisfying $x^3 + ax^2 + bx + c = 0$ then we can further reduce the cubic polynomial to a quadratic one.

$$x^3 + ax^2 + bx + c = (x - x_0)(x^2 + b^{'}x + c^{'}) = 0 \tag{A.57}$$

where

$$\begin{aligned} b^{'} &= -\frac{1}{x_0}\left(b + \frac{c}{x_0}\right) = a + x_0 \\ c^{'} &= -\frac{c}{x_0} \end{aligned} \tag{A.58}$$

Two cases need to be studied.

Case $\Delta > 0$

$$\begin{cases} x_0 = y^{\frac{1}{3}} - \frac{p}{3}y^{-\frac{1}{3}} - \frac{a}{3} \\ y = -\frac{q}{2} + \sqrt{\Delta} \end{cases}$$

Case $\Delta < 0$ In this case, the variable y is complex, and three real solutions

in x can be calculated (x_0, x_1, x_2).

$$\begin{aligned} x_1 x_2 &= c^{'} > 0 \\ x_1 + x_2 &= -b^{'} = \frac{1}{x_0}\left(b + \frac{c}{x_0}\right) = -(a + x_0) \end{aligned} \tag{A.59}$$

A.1.2 Solving for the downstream plasma variables

We have shown above that the density ratio x can be calculated explicitly. We now need to express the other variables. In the shock frame, $V_s = 0$, we have

$$x = \frac{\rho}{\rho_2} = \frac{U_{2n}}{U_n} \quad , \quad \eta = 0 \quad , \quad \alpha = 1 \tag{A.60}$$

which in turn, using equations (A.33),(A.34),and (A.35), allows us to obtain the downstream variables. First we define the variable N, which enables us to derive a compact form of the magnetic field.

$$N = \frac{B_2}{B} \quad \Rightarrow \quad B_2 = NB \quad \Rightarrow \quad B_{2y}^2 + B_{2z}^2 = B_2^2 - B_{2x}^2 = (N^2 - r^2)B^2 \tag{A.61}$$

Using equations (A.37) we obtain

$$\left.\begin{aligned} B_{2y} &= \gamma_y U\sqrt{\mu_0\rho} \\ B_{2z} &= \gamma_z U\sqrt{\mu_0\rho} \end{aligned}\right\} \Rightarrow B_{2y}^2 + B_{2z}^2 = \left(U\sqrt{\mu_0\rho}\right)^2\left[\gamma_y^2 + \gamma_z^2\right]$$

This result, along with equations (A.43) and (A.61), gives

$$N^2 - r^2$$

$$=$$

$$\left(\frac{M_A}{\alpha^2 x - m^2\delta^2}\right)^2 \left[\frac{\alpha^4}{M_A^2} - \alpha^2\left(\alpha + 2\frac{\delta^2}{M_A^2}\right)m^2 + \delta^2\left(2\alpha^2 + \frac{\delta^2}{M_A^2}\right)m^4 - \delta^4 m^6\right]$$

$$= \tag{A.62}$$

$$\left(\frac{1}{\alpha^2 x - r^2\frac{\delta^2}{M_A^2}}\right)^2 \left[\alpha^4 - \alpha^2\left(\alpha + 2\frac{\delta^2}{M_A^2}\right)r^2 + \frac{\delta^2}{M_A^2}\left(2\alpha^2 + \frac{\delta^2}{M_A^2}\right)r^4 - \frac{\delta^4}{M_A^4}r^6\right]$$

Similarly

$$\left.\begin{aligned} U_{2y} &= \beta_y U_n \\ U_{2z} &= \beta_z U_n \end{aligned}\right\} \Rightarrow U_{2y}^2 + U_{2z}^2 = U_n^2\left[\beta_y^2 + \beta_z^2\right]$$

which leads to

$$\begin{aligned}
U_{2y}^2+U_{2z}^2 &= \left(\frac{U_n}{\alpha^2 x-m^2\delta^2}\right)^2\left\{\left[\alpha^2(\delta^2-1)-2\frac{\alpha\delta^3 s}{M_A}m+\delta^2\left(2\alpha+\frac{\delta^2}{M_A^2}\right)m^2-\delta^4 m^4\right]\alpha^2x^2\right.\\
&+ 2\delta^2 m\left[\frac{\alpha^2\delta s}{M_A}+\alpha(1-\alpha-\frac{\delta^2}{M_A^2}-\delta^2)m+\frac{\delta^3 s}{M_A}m^2+\delta^2(\alpha-1)m^3\right]\alpha x\\
&+ \left.m^2\delta^4\left[\left(\frac{\alpha}{M_A}\right)^2-2m\delta s\left(\frac{\alpha}{M_A}\right)-(\alpha-1-\delta)(\alpha-1+\delta)m^2\right]\right\}\\
&= \left(\frac{U_n}{\alpha^2 x-r^2\frac{\delta^2}{M_A^2}}\right)^2\left\{\left[\alpha^2(\delta^2-1)-2\frac{\alpha\delta^3 s}{M_A^2}r+\frac{\delta^2}{M_A^2}\left(2\alpha+\frac{\delta^2}{M_A^2}\right)r^2-\frac{\delta^4}{M_A^4}r^4\right]\alpha^2x^2\right.\\
&+ 2\frac{\delta^2}{M_A^2}r\left[\alpha^2\delta s+\alpha(1-\alpha-\frac{\delta^2}{M_A^2}-\delta^2)r+\frac{\delta^2}{M_A^2}\delta s r^2+\frac{\delta^2}{M_A^2}(\alpha-1)r^3\right]\alpha x\\
&+ \left.r^2\frac{\delta^4}{M_A^4}\left[\alpha^2-2r\delta s\alpha-(\alpha-1-\delta)(\alpha-1+\delta)r^2\right]\right\} \qquad \text{(A.63)}
\end{aligned}$$

Expressions (A.62) and (A.63) take the following forms in the shock frame

$$N^2-r^2=\left(\frac{1}{x-r^2\frac{\delta^2}{M_A^2}}\right)^2\left[1-\left(1+2\frac{\delta^2}{M_A^2}\right)r^2+\frac{\delta^2}{M_A^2}\left(2+\frac{\delta^2}{M_A^2}\right)r^4-\frac{\delta^4}{M_A^4}r^6\right] \qquad \text{(A.64)}$$

and

$$\begin{aligned}
\left(\frac{U_2}{U_n}\right)^2-x^2 &= \left(\frac{1}{x-m^2\delta^2}\right)^2\left\{\left[\delta^2-1-2\frac{\delta^3 s}{M_A}m+\delta^2\left(2+\frac{\delta^2}{M_A^2}\right)m^2-\delta^4m^4\right]x^2\right.\\
&+ 2\delta^2 m\left[\frac{\delta s}{M_A}-\delta^2(1+\frac{1}{M_A^2})m+\frac{\delta^3 s}{M_A}m^2\right]x\\
&+ \left.m^2\delta^4\left[\frac{1}{M_A^2}-\frac{2m\delta s}{M_A}+\delta^2m^2\right]\right\} \qquad \text{(A.65)}
\end{aligned}$$

A.1.3 The Normal Component of the Electric Field $\vec{E}$ and the Pressure Term

The normal components of the electric field are given by equation (A.21)

$$\begin{aligned} \vec{E}\cdot\hat{n} &= U_z B_y - U_y B_z \\ \vec{E}_2\cdot\hat{n} &= U_{2z} B_{2y} - U_{2y} B_{2z} \end{aligned} \tag{A.66}$$

using the expressions for the velocity and the magnetic field, we can express the normal components upstream and downstream as follows:

$$\vec{E}_2\cdot\hat{n} = \left(\frac{\alpha^2 - m^2\delta^2}{\alpha^2 x - m^2\delta^2}\right)\vec{E}\cdot\hat{n} = \left(\frac{\alpha^2 - r^2\frac{\delta^2}{M_A^2}}{\alpha^2 x - r^2\frac{\delta^2}{M_A^2}}\right)\vec{E}\cdot\hat{n} \tag{A.67}$$

The pressure term is given by equation (A.39)

$$\begin{aligned} \frac{P_2}{\rho U_n^2} &= \alpha^2 + \frac{1}{\gamma}\frac{\delta^2}{M_S^2} + \frac{1}{2}\frac{\delta^2}{M_A^2}\left(1 - r^2\right) - \alpha^2 x \\ &- \frac{1}{2}\left(\frac{1}{\alpha^2 x - r^2\frac{\delta^2}{M_A^2}}\right)^2 \frac{\delta^2}{M_A^2}\left[\alpha^4 - \alpha^2\left(\alpha + 2\frac{\delta^2}{M_A^2}\right)r^2 + \frac{\delta^2}{M_A^2}\left(2\alpha^2 + \frac{\delta^2}{M_A^2}\right)r^4 - \frac{\delta^4}{M_A^4}r^6\right] \end{aligned} \tag{A.68}$$

Expressions (A.62) and (A.63) take the following forms in the shock frame

$$N^2 - r^2 = \left(\frac{1}{x - r^2\frac{\delta^2}{M_A^2}}\right)^2 \left[1 - \left(1 + 2\frac{\delta^2}{M_A^2}\right)r^2 + \frac{\delta^2}{M_A^2}\left(2 + \frac{\delta^2}{M_A^2}\right)r^4 - \frac{\delta^4}{M_A^4}r^6\right] \tag{A.69}$$

and

$$\left(\frac{U_2}{U_n}\right)^2 - x^2 = \left(\frac{1}{x - m^2\delta^2}\right)^2 \left\{ \left[\delta^2 - 1 - 2\frac{\delta^3 s}{M_A}m + \delta^2\left(2 + \frac{\delta^2}{M_A^2}\right)m^2 - \delta^4 m^4\right] x^2 \right.$$
$$+ 2\delta^2 m\left[\frac{\delta s}{M_A} - \delta^2(1 + \frac{1}{M_A^2})m + \frac{\delta^3 s}{M_A}m^2\right] x$$
$$\left. + m^2\delta^4\left[\frac{1}{M_A^2} - \frac{2m\delta s}{M_A} + \delta^2 m^2\right]\right\} \qquad \text{(A.70)}$$

Appendix B

The Earth's Magnetopause Size

The location of the magnetopause can be determined by the use the static pressure balance of the solar wind dynamic pressure and the magnetic pressure in the magnetosphere. The magnetospheric plasma is a low-β plasma and as a first approximation the dynamic pressure can be neglected. On the contrary, in addition to being supersonic, the solar wind is a plasma with $\beta \geq 1$. Because of the solar plasma is not directly in contact with the magnetopause, the effective upstream pressure at the magnetopause boundary is kp where $p = n_{sw}V_{sw}^2$ is the solar wind ram pressure and k a factor less than one. The magnetopause is a current layer since it forms a boundary between to regions with different magnetic fields. Neglecting the IMF, results that the current on the boundary is such that the field is basically null upstream. Since the magnetosheath magnetic pressure results from the magnetosphere magnetic field, we can show (see for example, Cravens, T. E [65]) that the

magnetic pressure just downstream of the magnetopause is given by:

$$p_B = \frac{2fB_{dipole}^2}{2\mu_0} \tag{B.1}$$

where f is a factor related to effectiveness of the electric current flowing along the boundary, and B_{dipole} is the geomagnetic dipole field. For a given distance R from Earth's centre and magnetic latitude λ, the Earth's magnetic field dipole is given by:

$$B_{dipole}\left(R,\lambda\right) = \frac{M}{R^3}\frac{\sqrt{\left(1+3\sin^2\lambda\right)}}{\cos^6\lambda} \tag{B.2}$$

where, M is the Earth magnetic dipole moment. In term of field strength,

$$B_{dipole}\left(R,\lambda\right) = B_0\left(\frac{R_E}{R}\right)^3\frac{\sqrt{\left(1+3\sin^2\lambda\right)}}{\cos^6\lambda} \tag{B.3}$$

where the distance R is now in Earth radius unit (R_E) and

$$B_0 = 3.011\times10^{-5}T$$

At the magnetic equator ($\lambda = 0$)

$$B\left(R\right) = B_0\left(\frac{R_E}{R}\right)^3 \tag{B.4}$$

Writing that the pressure balance at the magnetopause boundary is satisfied, $kp = p_B$ or

$$kp = p_B \tag{B.5}$$

or

$$kp = 2f^2 \frac{B_0^2}{\mu_0} \left(\frac{R_E}{R} \right)^6 \tag{B.6}$$

Using the numerical value of B_0 and expressing the ram pressure p in nPa, we deduce the sub-solar distance of the magnetopause:

$$\boxed{\left(\frac{R}{R_E} \right) = 9.47 \left(\frac{f^2}{k} \right)^{1/6} \left(\frac{2}{p} \right)^{1/6}} \tag{B.7}$$

Appendix C

Error Analysis

An estimation of uncertainties in the determination of the shock normal and speed are derived in this section.

C.1 Shock Speed

The timing technique provide the determination of the shock normal $\hat{n}\,(n_x, n_y, n_z)$

$$\begin{pmatrix} \vec{r}_{13} \\ \vec{r}_{23} \\ \vec{r}_{43} \end{pmatrix} \cdot \frac{1}{V} \begin{pmatrix} n_x \\ n_y \\ n_z \end{pmatrix} = \begin{pmatrix} t_{13} \\ t_{23} \\ t_{43} \end{pmatrix} \tag{C.1}$$

where V is the shock speed, t_{i3} and r_{i3} are respectively the time delay and the distance of spacecraft i ($i = 1, 2, 4$) with respect to SC3. Inverting (C.1)

we obtain

$$\frac{1}{V}\begin{pmatrix} n_x \\ n_y \\ n_z \end{pmatrix} = \begin{pmatrix} \vec{r}_{13} \\ \vec{r}_{23} \\ \vec{r}_{43} \end{pmatrix}^{-1} \begin{pmatrix} t_{13} \\ t_{23} \\ t_{43} \end{pmatrix} \tag{C.2}$$

or

$$\frac{1}{V}\begin{pmatrix} n_x \\ n_y \\ n_z \end{pmatrix} = \begin{pmatrix} \alpha_1 & \beta_1 & \gamma_1 \\ \alpha_2 & \beta_2 & \gamma_2 \\ \alpha_3 & \beta_3 & \gamma_3 \end{pmatrix} \begin{pmatrix} t_{13} \\ t_{23} \\ t_{43} \end{pmatrix} \tag{C.3}$$

where $(\alpha_i, \beta_i, \gamma_i)$ are the elements of the inverted matrix, whose elements are the components of the vectors $\vec{r}_{i3}$. For each component l

$$m_l = \frac{n_l}{V} = \alpha_l t_{13} + \beta_l t_{23} + \gamma_l t_{43} \tag{C.4}$$

Differentiating m_l and assuming that the uncertainty on the time delay are the same for all spacecraft ($dt_{13} = dt_{23} = dt_{43} = dt$):

$$dm_l = \frac{V\,dn_l - n_l dV}{V^2} = (\alpha_l + \beta_l + \gamma_l)\,dt \tag{C.5}$$

By definition

$$m_x^2 + m_y^2 + m_z^2 = \frac{1}{V^2} \tag{C.6}$$

By differentiating (C.6) and using (C.5) we have

$$
\begin{aligned}
-2\frac{dV}{V^3} &= 2\left(\alpha_1 t_{13}+\beta_1 t_{23}+\gamma_1 t_{43}\right)\left(\alpha_1+\beta_1+\gamma_1\right)dt \\
&\quad + 2\left(\alpha_2 t_{13}+\beta_2 t_{23}+\gamma_2 t_{43}\right)\left(\alpha_2+\beta_2+\gamma_2\right)dt \\
&\quad + 2\left(\alpha_3 t_{13}+\beta_3 t_{23}+\gamma_3 t_{43}\right)\left(\alpha_3+\beta_3+\gamma_3\right)dt \qquad \text{(C.7)}
\end{aligned}
$$

or

$$
\begin{aligned}
-\frac{dV}{V^3} &= \left[\left(\alpha_1 t_{13}+\beta_1 t_{23}+\gamma_1 t_{43}\right)\left(\alpha_1+\beta_1+\gamma_1\right)\right. \\
&\quad + \left(\alpha_2 t_{13}+\beta_2 t_{23}+\gamma_2 t_{43}\right)\left(\alpha_2+\beta_2+\gamma_2\right) \\
&\quad \left. + \left(\alpha_3 t_{13}+\beta_3 t_{23}+\gamma_3 t_{43}\right)\left(\alpha_3+\beta_3+\gamma_3\right)\right]dt \qquad \text{(C.8)} \\
&= A dt \qquad \text{(C.9)}
\end{aligned}
$$

where

$$
\begin{aligned}
A &= \left[\left(\alpha_1 t_{13}+\beta_1 t_{23}+\gamma_1 t_{43}\right)\left(\alpha_1+\beta_1+\gamma_1\right)\right. \\
&\quad + \left(\alpha_2 t_{13}+\beta_2 t_{23}+\gamma_2 t_{43}\right)\left(\alpha_2+\beta_2+\gamma_2\right) \\
&\quad \left. + \left(\alpha_3 t_{13}+\beta_3 t_{23}+\gamma_3 t_{43}\right)\left(\alpha_3+\beta_3+\gamma_3\right)\right] \qquad \text{(C.10)}
\end{aligned}
$$

In terms of absolute values, the uncertainty of V is given by

$$
\boxed{\Delta V = \left|AV^3\right|\Delta t} \qquad \text{(C.11)}
$$

C.2 Shock Normal

We now deduce the uncertainty on the shock normal. From (C.5) we have

$$\frac{V dn_x - n_x dV}{V^2} = (\alpha_1 + \beta_1 + \gamma_1)\, dt \tag{C.12}$$

$$\frac{dn_x}{V} = n_x \frac{dV}{V^2} + (\alpha_1 + \beta_1 + \gamma_1)\, dt \tag{C.13}$$

$$dn_x = n_x \frac{dV}{V} + V\,(\alpha_1 + \beta_1 + \gamma_1)\, dt$$

$$\boxed{\Delta n_x = \left|\frac{n_x}{V}\right| \Delta V + \left|V\Big(\alpha_1 + \beta_1 + \gamma_1\Big)\right| \Delta t} \tag{C.14}$$

The uncertainty of Δn_y and Δn_z are derived similarly.

C.3 Standoff Distance

For paraboloid bow shock model, the standoff distance in term of the shock normal is given by:

$$a_{st} = x + \frac{\sqrt{(1 - n_x^2)(y^2 + z^2)}}{2n_x} \tag{C.15}$$

or

$$a_{st} = x + \frac{1}{2}\sqrt{y^2 + z^2}\sqrt{\frac{1}{n_x^2} - 1}$$

Differentiating a_{st} (it is assumed that the spacecraft position is known precisely).

$$da_{st} = \frac{1}{2}\sqrt{y^2+z^2}\frac{1}{2}\frac{(-2n_x^{-3})}{\sqrt{\frac{1}{n_x^2}-1}}dn_x \tag{C.16}$$

$$= -\frac{1}{2}\sqrt{y^2+z^2}\frac{dn_x}{n_x^3\sqrt{\frac{1}{n_x^2}-1}}$$

or

$$= -\frac{a_{st}-x}{1-n_x^2}dn_x$$

In term of absolute error.

$$\boxed{\Delta a_{st} = \left|\frac{a_{st}-x}{1-n_x^2}\right|\Delta n_x} \tag{C.17}$$

Appendix D

Forcing the Conics Models

We show how the parameter $f = \frac{p}{p_0}^{-1/6}$, which is evaluated under the condition that a particular shock crossing satisfies a statistical bow shock model, is calculated. The are four widely used models, including the ellipsoidal model from Cairns et al. [30], the elliptical mode from Farris et al.[47], the hyperboloid model from Slavin and Holzer [49] and Merka's model [31]. The solution for the case the elliptical model was treated in chapter 3. We now present the treatment for the other three models. In this context, as mentioned in section (**??**), the shape of the bow shock can be represented by the following surface equation:

$$a_1x^2 + y^2 + a_3z^2 + 2a_4xy + 2a_7x + 2a_8y + a_{10} = 0 \qquad \text{(D.1)}$$

D.1 Forcing Ellipsoid Model

For forcing the ellipsoid model, we use Farris et al. [47] model. In this case, the coefficients in equation D.1 correspond to the following: $a_1 = 1 - \varepsilon^2$, $a_2 = a_3 = 1$, $a_4 = 0$, $a_7 = \varepsilon * L$, $a_8 = 0$ and $a_{10} = -L^2$ where $L = fL_0$ with the nominal numerical value $\varepsilon = 0.83$ and $L_0 = 24.8R_E$. Replacing the coefficient a_i in equation (D.1), we obtain the second degree equation to solve:

$$\left(L_0^2\right) f^2 - 2\left(\varepsilon x_S L_0\right) f - \left[\left(1-\varepsilon^2\right) x^2 + y_S^2 + z_S^2\right] = 0 \tag{D.2}$$

where (x_S, y_S, z_S) are the position component of the spacecraft at the crossing. Only the positive root is physical and therefore is given by:

$$f = \frac{1}{L_o^2}\left[\varepsilon x L_o + \sqrt{\left(\varepsilon x L_o\right)^2 + L_0^2\left[\left(1-\varepsilon^2\right) x^2 + y^2 + z^2\right]}\right] \tag{D.3}$$

D.2 Forcing the Hyperboloid Model

For forcing the hyperboloid model, we use Sliven and Holzer [49] model. In this case, the coefficients are:

$a_1 = 1 - \varepsilon^2$, $a_2 = a_3 = 1$, $a_4 = 0$, $a_7 = \varepsilon L - x_0(1-\varepsilon^2)$, $a_8 = 0$ and $a_{10} = -L^2 - \varepsilon x_0(\varepsilon x_0 0 + 2L)$ where $L = fL_0$ and $x_0 = fx_{00}$ with the nominal numerical value $\varepsilon = 1.16$, $L_0 = 23.3R_E$ and $x_0 = 3R_E$. Replacing the coefficient a_i in equation D.1, we obtain the second degree equation to solve:

$$\left[L_0^2 + \varepsilon x_{00}\left(\varepsilon x_{00} + 2L_0\right)\right] f^2$$
$$- 2x_S\left[\varepsilon L_0 - \left(1-\varepsilon^2\right) x_{00}\right] f - \left[\left(1-\varepsilon^2\right) x_S^2 + y_S^2 + z_S^2\right] = 0 \quad \text{(D.4)}$$

Again only the positive numerical value is considered

$$\boxed{f = \frac{x_S\left[\varepsilon L_0 - (1-\varepsilon)\, x_{00}\right] + \sqrt{\Delta}}{\left[L_0^2 + \varepsilon x_{00}\left(\varepsilon x_{00} + 2L_0\right)\right]}} \quad \text{(D.5)}$$

with

$$\Delta = x_S^2\left[\varepsilon L_0 - (1-\varepsilon)\, x_{00}\right]^2 + \left[L_0^2 + \varepsilon x_{00}\left(\varepsilon x_{00} + 2L_0\right)\right]$$
$$- \left[\left(1-\varepsilon^2\right) x_S^2 + y_S^2 + z_S^2\right] \quad \text{(D.6)}$$

D.3 Forcing Merka's Model

For this model, the coefficients are given in terms of Alvenic Mac number M_A with $a_2 = 1$:

$$\begin{cases} a_1 = 0.0063 - 0.0098 M_A \\ a_3 = 0.8351 + 0.102 M_A \\ a_4 = 0.298 + 0.004 M_A \\ a_7 = f a_{07}, (a_{07} = 16.39 + 0.2087 M_A + \frac{108.2}{(M_A - 1)^2}) \\ a_8 = f a_{08}, (a_{08} = -0.9421 + 0.0721 M_A) \\ a_{10} = f^2 (a_{010} = -444 - 2.935 M_A - \frac{1930}{(M_A - 1)^2}) \end{cases} \tag{D.7}$$

Replacing the coefficient a_i in equation (D.1), we obtain the second degree equation to solve:

$$a_{010} f^2 + 2 \left(a_{07} x_S + a_{08} y_S \right) f + \left[a_1 x_S^2 + a_2 y_S^2 + a_{03} z_S^2 + 2 a_{04} x_S y_S \right] \tag{D.8}$$

which gives the positive solution:

$$f = \frac{1}{a_{010}} \left[- \left(a_{07} x_S + a_{08} y_S \right) + \sqrt{\Delta} \right] \tag{D.9}$$

with

$$\Delta = \left(a_{07} x_S + a_{08} y_S \right)^2 + \left(a_{07} x_S + a_{08} y_S \right) \left[a_{07} x_S^2 + a_2 y_S^2 + a_3 z_S^2 + 2 a_4 x_S y_S \right] \tag{D.10}$$

Vita

Candidate's full name: Thamer Yousef S Alrefay

University attended :

Master of Science, Florida Institute of Technology , 2003

Bachelor of Science,King Abdulaziz University, 1996

Publications:

K. Meziane,T.Y. Alrefay and A. M. Hamza.*On the shape and motion of the earth's bow shock*. Planet. Space Sci.93-94, pp 1-9 2014.

K. Meziane, A. M. Hamza and T.Y. Alrefay, *Shock Dynamics: Velocity and Standoff Distribution functions*, in preparation for JGR, July 2014.

Conference Presentations:

Alrefay,T.Y.,Meziane.K.,Hamza,A.H.(2013), ,"Bow shock dynamics as observed by cluster satellites", DASP, Kingston,Canada.

Alrefay,T.Y.,Meziane.K.,Hamza,A.H.(2013),," Motion of the earth's bow shock", CAP, Montreal, Canada.

Alrefay,T.Y.,Meziane.K.,Hamza,A.H.(2013)," Motion of the earth's bow shock from cluster data", AGU,Cancun,Mexico. (Poster).